FREE AND NANOENCAPSULATED INDOCYANINE GREEN FOR NEAR INFRARED AND MULTIPHOTON BIOIMAGING

Ph.D. Thesis

By

ANSHU KUMARI

DISCIPLINE OF BIOSCIENCES AND BIOMEDICAL ENGINEERING

INDIAN INSTITUTE OF TECHNOLOGY INDORE

JUNE 2019

FREE AND NANOENCAPSULATED INDOCYANINE GREEN FOR NEAR INFRARED AND MULTIPHOTON BIOIMAGING

A THESIS

Submitted in partial fulfillment of the requirements for the award of the degree

of

DOCTOR OF PHILOSOPHY

by

ANSHU KUMARI

DISCIPLINE OF BIOSCIENCES AND BIOMEDICAL ENGINEERING

INDIAN INSTITUTE OF TECHNOLOGY INDORE

JUNE 2019

INDIAN INSTITUTE OF TECHNOLOGY INDORE

CANDIDATE'S DECLARATION

I hereby certify that the work which is being presented in the thesis entitled **FREE AND NANOENCAPSULATED INDOCYANINE GREEN FOR NEAR INFRARED AND MULTIPHOTON BIOIMAGING** in the partial fulfillment of the requirements for the award of the degree of **DOCTOR OF PHILOSOPHY** and submitted in the **DISCIPLINE OF BIOSCIENCES AND BIOMEDICAL ENGINEERING, INDIAN INSTITUTE OF TECHNOLOGY INDORE**, is an authentic record of my work carried out during the time period from January 2014 to June 2019 under the supervision of **Dr. Sharad Gupta**, Associate Professor, Discipline of Biosciences and Biomedical Engineering and Metallurgical Engineering and Material Science.

The matter presented in this thesis has not been submitted by me for the award of any other degree of this or any other institute.

Signature of the student with date: **Miss. Anshu Kumari**

This is to certify that the above statement made by the candidate is correct to the best of my/our knowledge.

Signature of Thesis Supervisor with date

(Dr. Sharad Gupta)

Miss Anshu Kumari has successfully given her a Ph.D. Oral Examination held on June 2, 2020.

Signature of Chairperson (OEB)
Date: 02.06.2020

Signature of External Examiner
Date: 02/06/2020

Signature(s) of Thesis Supervisor(s)
Date: 02/06/2020

Signature of PSPC Member #1
Date: 2/6/2020

Signature of PSPC Member #2
Date: 02/06/2020

Signature of Convener, DPGC
Date: 02/06/2020

Signature of Head of Discipline
Date: 02/06/2020

ACKNOWLEDGMENT

"Acknowledgements are never written by ink; they are always written by heart."

Working in a multi-disciplinary field could have never been easy without a friendly atmosphere and sincere support from my mentor, parents, and siblings. Therefore, in the beginning, I would like to thank those people without whom this work would not have been successful and those whose presence made my journey a joyful one.

First of all, I would like to express my sincere gratitude for my mentor ***Dr. Sharad Gupta*** *for offering me a position to work in the field of nanobiophotonics and his kind support in every aspect during my Ph.D. His motivation, faith in me, continuous valuable guidance, unfailing support, and his genuine never-ending care not only made this journey successful but also helped me to develop more organized research skills. His never-ending discussions and meticulous ideas always helped me to design my experiment with utmost care. Further, I would like to mention a sincere thanks for his inexhaustible patience during the correction phase of my academic writings. This is an honor for me to be his first Ph.D. student, and I could not have imagined having a better mentor for my Ph.D. Also, I want to give my sincere thanks to* ***Mrs. Tsetsegdari Damba*** *and her kids for their love and support throughout my Ph.D., which never let me feel that I am away from home.*

I am grateful to my parents (Ex-Army person A.K.Mishra and Mrs. Amarawati Devi) and my sibling Mrs. Gayatri Mishra, Mr. Pankaj K. Mishra, Mr. Amitab Mishra, and sister-in-law Capt. Raj Shukla for their unconditional love, continuous support, and motivation in every aspect of my life. Additionally, I am lucky to have ***Dr. Debasis Nayak, Dr. I. A. Palani,*** *and* ***Dr. Srivathsan Vasudevan*** *as one of the internal evaluation committee members, whose continuous guidance helped in the planning of work, gave motivation and made this work much more enjoyable. I want to expand my thanks to* ***Prof. Boyapati Manoranjan Choudary*** *for his valuable comments during the*

upgradation seminar from the junior research fellow position to the senior research fellow position. I would love to mention my sincere thanks to the late ***Dr. Kaustuv Das*** *and his students in Raja Ramanna Centre for Advanced Technology (RRCAT) Indore for sharing their instrument and knowledge for my research. I want to express my thanks to* ***Mr. Manoj, Mr. Ganapathi, Mr. Yoganand****, and* ***Mr. Morison*** *for sharing the technical expertise of confocal, multiphoton lasers, and time-correlated single-photon counting (TCSPC) instrumentation.*

*I also acknowledge the Department of Science & Technology India for sponsored Innovation in Science Pursuit for Inspired Research (****INSPIRE-IF140809****) fellowship during my Ph.D. and the Ministry of Human Resource Development* ***(MHRD)*** *for providing me with financial assistance during the initial year of my Ph.D.*

*Further, I want to thanks all my lab members (****Mr. Surjendu B. Dutta, Mr. Prashant Kharey,*** *and* ***Ms. Somya Jaiswal****) of the biophysics and biomedical and virology research group. Notably,* ***Mrs. Suman Bishnoi,*** *for sharing her valuable knowledge of biological techniques and scientific discussions. My sincere thanks to the Sophisticated Instrumentation Center* ***(SIC)*** *at the Indian Institute of Technology Indore (****IITI****). I would also like to thank Dr. Tejendra Dixit, Dr. Shailendra Saxena, and Mr. Kinny Pandey, who guided me in learning the field electron microscopy during the initial days of my research. I like to thank Mr. Ravinder and Mr. Ghanshayam for confocal and circular dichroism measurements. It is giving me immense pleasure to thank* ***Dr. Tridip Sarma*** *and Dr. Deepa Dey for their love and support they gave me during my Ph.D. days. I would also like to thank the students for helping me during the dynamic light scattering (DLS) measurements. Dr. Sonam Mandani and Mr. Sidharth Jain to be always there for DLS measurements. I am happy to have the support from Ms. Kalpana Kumari, Ms. Sheeba, and Ms. Abhipsa Panda; they helped me whenever I needed them, either by helping me doing experiments or by sharing any valuable thoughts. My special thank to Mr. Surjendu Dutta for his sincere support in data analysis,* ***Mr. Anurag R. Mishra,*** *and* ***Mr. Ritudwaj Tiwari*** *for standing by me in all good and bad days.*

*I love to grab the opportunity to thank **Dr. Vikas Yadav** and Mr. Subi Sugathan for teaching me the cell culture. Moreover, this acknowledgment cannot be completed without expressing my appreciation to Mr. Surender Bishnoi and Mr. Mukund; without their love, care, support, and understanding, I would not have been able to enjoy and complete this work successfully. Mrs. Suman Bishnoi became an inspiration and motivation for my every work since she came into my life. Moreover, I would like to express my sincerest thanks to my friends Dr. Mayur Sawant, Mrs. Tejaswani Sawant, Dr. Ankita Jain, Dr. Tejendra Dixit, Dr. P.S.N. Raju, Dr. Anupam, Dr. Roopali, Dr. Anuradha Dagar, Dr. Avadhesh K. Sharma, Ms. Shaifali Arora, Mr. Vishal Jain, Mr. Prajwal Kinake, Mr. Vinit Saraswat and Mr. Pankaj, Mr. Ajay, Miss Meena A. Krishnan, Mr. Rian, and Mr. Naveen and his family.*

I expand my thanks to the whole member of the Discipline of Biosciences and Biomedical Engineering. Mr. Amit Mishra and Mr. Arif Patel for their supportive nature. My gratitude towards Dr. Shilpa, Dr. P. Matkar, and other medical staff members of IITI who were always there for me during my Ph.D. days. Last but not least, I want to thank all staff members of the IITI for providing all comfort and convenience. Besides this, there are many more who have directly or indirectly contributed to making this journey successful, I wish I could thank them all, but time and space compel me to stop here.

Anshu Kumari

Dedicated

to

My Family

and

My Mentor

Dr. Sharad Gupta and Mrs. Tsetsegdari Damba

For their advice, their patience, and their faith in me.

SYNOPSIS

Early-stage cancer detection is a crucial step towards successful cancer treatment as well as for improving the patient survival rate. In recent years, molecular imaging has gained tremendous interest in early-stage cancer diagnosis. Nowadays, for molecular imaging scientific community has started to use the exogenous contrast agents to improve the detection ability of the existing imaging modalities. Especially, the use of exogenous near-infrared fluorescence (NIRF) contrast agents has improved the quality of NIR optical bioimaging. It helps in visualization of deeply buried inhomogeneities inside the tissue due to less scattering, low endogenous absorption, and almost zero auto-fluorescence in the NIR wavelength range. Additionally, it enables researchers to study the deep-seated abnormalities with an enhanced signal-to-noise ratio (SNR).

Indocyanine green (ICG) is the only U. S. Food and Drug Administration (FDA) approved NIRF dye that is being used in clinics for the last approximately 60 years. However, the use of ICG to the fullest has been limited due to its short blood circulation time, non-specific binding within the body, undesirable aggregation, poor aqueous stability, poor cellular uptake, and poor optical and thermal stability. These limitations of the ICG could be addressed by the nanoencapsulation of ICG within a carrier for site-specific delivery. To date, various nanocarriers have been developed, such as micelles, liposomes, polymers, metals, and composites, *etc.* However, none of them has reached clinical practice due to limitations such as non-biodegradability and non-biocompatibility, which leads to short and long-term cellular toxicity. Keeping these limitations in mind, the primary focus of this thesis has been to encapsulate ICG within biocompatible and biodegradable nanocarriers. A green chemistry-based two-step self-assembly method has been developed to fabricate these nanoparticles. The ICG loaded nanoparticles demonstrated an improved efficiency of ICG delivery in cells in comparison with the free form of ICG.

In addition, the nonlinear excitation properties of ICG and its application for multiphoton bioimaging has been studied for the first time. As shown in **Figure a,** apart from ICG well-known NIR absorption at 780 nm, it also shows two absorption bands with peak intensity at ~400 nm and ~230 nm. However, there was negligible information available in the literature about the origin of these absorption bands and their possible applications. Therefore, in this thesis, an effort has been made to understand the origin of

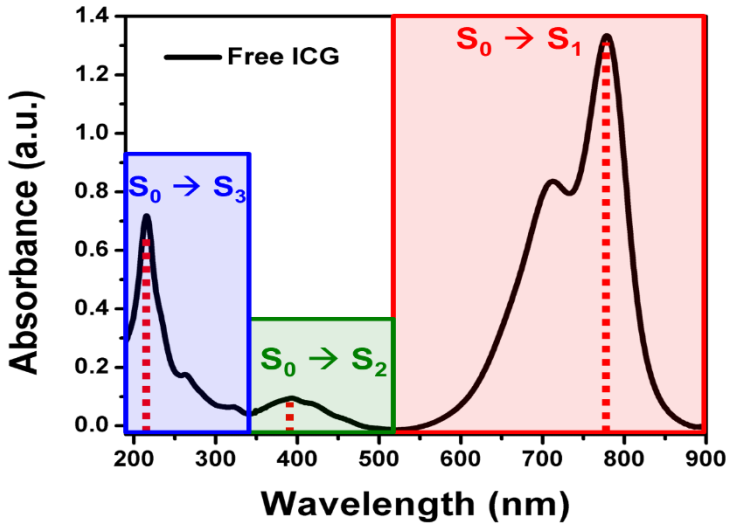

Figure a. Absorption spectrum of the aqueous solution of free ICG where ICG is indocyanine green, S_0, is ground state and S_1, S_2, and S_3 is first, second and third excited singlet state.

these bands and their potential applications. The results obtained in this thesis suggest that ICG could be used as an exogenous contrast agent for multiphoton bioimaging.

Moreover, the effect of nanoencapsulation of ICG on multiphoton bioimaging has also been studied in this thesis. The amino acid-based nanoparticles developed here provide a glimpse of the nanoencapsulated ICG for NIR and multiphoton bioimaging applications. These findings can start the ICG mediated preclinical and clinical multiphoton bioimaging.

The main objectives of the presented study are as following:

- A novel green chemistry-based synthesis of ICG loaded biocompatible and biodegradable poly-l-lysine (PLL) nanoparticles for NIR bioimaging.
- To study the nonlinear excitation of ICG to S_2 and S_3 states and its application in multiphoton bioimaging.
- To study the effect of nanoencapsulation of ICG on multiphoton bioimaging.

The Ph.D. thesis is divided into six chapters, as mentioned below.

C**hapter 1** gives the introduction of indocyanine green (ICG) and provides a comprehensive review of the literature for various applications of ICG. Additionally, a detailed discussion of the ICG optical properties and its various biomedical applications has been provided. This is followed by a summary of the work presented in the thesis.

C**hapter 2** describes the details of the materials and methods used in this thesis. In this chapter, the principles and specifications of the instruments used in the research work have been explained.

Chapter 3 introduces the drawbacks of the ICG, which limits its application in the clinics. The conventional delivery of the ICG results in non-specific binding of ICG with various plasma proteins causing a short residence time in the bloodstream. This problem can be addressed by protecting ICG within nanocarriers. In this chapter, green chemistry-based two-step nanoencapsulation of ICG is shown within the essential amino acid-based nanoparticles. Followed by the complete biophysical and biochemical characterization of the nanoparticles. The NIR bioimaging application of these nanoparticles will also be demonstrated.

The **fourth chapter** of this thesis is focused on understanding the mechanism of higher energy absorption peaks of ICG and its possible application. Both optical absorption spectroscopy and fluorescence spectroscopy are used to understand the origin of these high energy absorption peaks. It was found that these absorption peaks are due to the transition of electrons from the ground state (S_0) to higher energy states such as second and third excited singlet states (S_2 and S_3respectively). In addition, in this chapter, nonlinear excitation of ICG to the higher energy states, followed by an emission, is demonstrated. This nonlinear excitation to the higher excited states followed by an emission was used for ICG mediated bioimaging. These experimental results suggest that ICG could be used for in-vivo multiphoton bioimaging applications in the future.

Chapter 5 discuss the effect of ICG nanoencapsulation on multiphoton bioimaging. To study this, the ICG was nanoencapsulated in the arginine based homopeptide using a simple two-step self-assembly process in aqueous solution. Motivated by the results of our previous in-vitro studies, we extended our investigations to evaluate the effectiveness of nanoencapsulated ICG for multiphoton bioimaging. It was found that nanoencapsulated ICG showed superior nonlinear two-photon imaging ability than the free ICG formulation. Our results also indicate that ICG-doped PLA NPs are not cytotoxic.

Chapter 6 conclude the finding and summarizes the salient features of the entire work of the thesis and envisions the possible future steps. The outlook of the story also discusses the possible way to broadening the application of ICG in preclinical and clinical trials.

LIST OF PUBLICATIONS

(A) Publications from Ph.D. thesis work:

A1. In Refereed Journals: 2

1. **Kumari, A.** and Gupta, S. "Two-photon excitation and direct emission from S2 state of U.S. Food and Drug Administration approved near-infrared dye: Application of anti-Kasha's rule for two-photon fluorescence imaging." J. Biophotonics., 2019; 12: e201800086. DOI: 10.1002/jbio.201800086. (IF 3.763)

2. **Kumari, A.,** Kumari, K., and Gupta, S. "The effect of nanoencapsulation of ICG on two-photon bioimaging" RSC Adv., 2019; 9: 18703-18712. DOI: 10.1039/C9RA03152A. (IF 3.049)

3. **Kumari, A.,** Kumari, K., and Gupta, S. "Protease Responsive Essential Amino-Acid Based Nanocarriers for Near-Infrared Imaging" Scientific Reports, 2019, 9**,** 20334. DOI: 10.1038/s41598-019-56871-4. (IF 4.011)

A2. Book Chapter: 1

4. **Kumari, A.,** and Gupta, S., "Enzyme-responsive nanocontainer for small molecule delivery" In Tri, N. P., Do-Trong, O., and Nguyen, T. A., editors, in Micro and Nano Technologies "Smart Nanocontainers", Elsevier, Chapter 13, 2020, pp: 217-227, ISBN: 978-0-12-816770-0.

A3. Patent: 1

5. **Kumari, A.** and Gupta, S. "Essential amino-acid based biodegradable and biocompatible nanoparticles for biomedical imaging and targeted drug delivery applications," *Indian Patent 201721027869*, Published on 14 September, 2018.

A4. Unpublished Work: 3

6. **Kumari, A.** and Gupta, S. "Indocyanine Green as Non-linear Optical Material for Multiphoton Bioimaging" manuscript under preparation.

7. **Kumari, A.** and Gupta, S. "Application of ICG for White-Light Generation" manuscript under preparation.

A5. Conferences:

International/ National Conference (Oral Presentations): 3

8. **Kumari, A.,** Amit et. al. "S_2 State Optical Property Enhancement of Indocyanine Green Due to Optical Exposure" in press in Proc. SPIE**.**

9. **Kumari, A.** and Gupta, S. "Application of the Indocyanine Green for Multiphoton Bioimaging." in 1st In-house symposium on Advances in biosciences and bioengineering organized by Discipline of Biosciences and Biomedical Engineering, Indian Institute of Technology Indore on Feb 2019.

10. **Kumari, A.,** Kharey P. and Gupta, S. "Facile green synthesis of NIR active nanoparticles from biomolecules for biomedical imaging." in International Symposium on Functional Materials : Energy and Biomedical applications (IFSM-2018) organized by IIT Kanpur, Panjab University Chandigarh and University of Illinois at Chicago during April 13-15, 2018 at Chandigarh.

International/ National Conference (Poster Presentation): 3

11. **Kumari, A.** and Gupta, S. "Polypeptide based poly-L-lysine nanoparticles for photothermal therapy." in 1st In-house symposium on Advances in biosciences and bioengineering organized by Discipline of Biosciences and Biomedical Engineering, Indian Institute of Technology Indore on Feb 2019.

12. Panda, A., **Kumari, A.** and Gupta, S. "Quercetin based nanoparticles for theranostics." in 1st In-house symposium on Advances in biosciences and bioengineering organized by Discipline of Biosciences and Biomedical Engineering, Indian Institute of Technology Indore on Feb 2019.

13. **Kumari, A.** and Gupta, S. "Nanoparticles for Biomedical Applications." in International Symposium on the emerging area in Biosciences and Biomedical Engineering (eBBT-2018).

(B) Other publications during Ph.D.:

B1. In refereed Journals: 3

14. Biswas, D., **Kumari, A.,** K., G. C., Vasudevan, S., Gupta, S., Shukla, S., & Garg, U. K. (2017). Quantitative Differentiation of Pneumonia from Normal Lungs: Diagnostic Assessment Using Photoacoustic Spectral Response. *Applied Spectroscopy*, *71*(11), 2532–2537. DOI: 10.1177/0003702817708320 (IF 1.6)

15. Gorey, A., Biswas, D., **Kumari, A.,** Gupta, S. *et al.* "Application of continuous-wave photoacoustic sensing to red blood cell morphology" Laser in Medical Science, 2018, DOI: 10.1007/s10103-018-2621-7 (IF 1.95)

16. Kharey, P., Dutta, S. B., Gorey, A., Manikandan, M., **Kumari, A.,** Vasudevan, S., Palani, I. A., Majumder, S. K., and Gupta, S. "Pimenta dioica Mediated Biosynthesis of Gold Nanoparticles and Evaluation of Its Potential for Theranostic Applications." Chemistry Select, 2020, 5(26):7901-7908 (IF: 1.8).

17. **Kumari, A.,** Panda, A., Kumar, A. and Gupta, S. "Enhancement of Physico-chemical Properties of the Hydrophobic Anticancer Molecule Following Nanoencapsulation" manuscript under preparation.

18. **Kumari, A.,** Nayak, D., and Gupta, S. "Viral nanofactory for biomedical applications" manuscript under preparation.

B2. Conferences

Peer-reviewed International conference: 2

19. **Mishra, A.,** Biswas, D., Kharey P., Vasudevan S., and Gupta S. "Near-Infrared Activated Polymer Nanoparticles for Photoacoustic Imaging." in 13th International Conference on Fiber Optics and Photonics, OSA Technical Digest (online) (Optical Society of America, 2016), paper Tu2B.4; DOI: 10.1364/PHOTONICS.2016.Tu2B.4.

20. **Kumari, A.,** Kumar, A., and Gupta, S. "Enhancement of Physico-chemical Properties of the Hydrophobic Anticancer Molecule Following Nanoencapsulation." Proc. SPIE 10507, Colloidal Nanoparticles for Biomedical Applications XIII, 1050713 (23 February 2018); DOI: 10.1117/12.2287327.

International/ National Conference (Poster Presentation): 1

21. Biswas, D., **Kumari, A.** et al., "Gold Nanoparticle as Photoacoustic Tomography Contrast Agent." in Proc. International Conference on Nanoscience and Technology (ICONSAT 2016), 29 February – 2 March 2016, P-184. Pp.139.

TABLE OF CONTENTS

LIST OF FIGURES

Chapter 1

Chapter 2

Chapter 3

Chapter 6

ABBREVIATIONS

Indocyanine green	ICG
Highest occupied molecular orbital	HOMO
Lowest unoccupied molecular orbital	LUMO
Nearinfrared	NIR
Ultraviolet	U.V.
Visible	Vis
Cyanine dye	Cy-dye
United State	U. S.
Food and Drug Administration	FDA
Hypsochromic aggregates	H-aggregates
Jelly aggregates	J-aggregates
Signal-to-Noise Ratio	SNR
Polylactic-co-glycolic acid	PLGA
Nearinfrared fluorescence	NIRF
Magnetic resonance imaging	MRI
Optical imaging	O.I.
Three dimensional	3D
Continuous-wave	CW
Deionized water	DI
Photothermal therapy	PTT
Photodynamic therapy	PDT
Phospholipid-polyethylene glycol	PL-PEG
Monoclonal antibody	mAb
Anti-epidermal growth factor receptor	anti-EGFR

Reactive oxygen species	ROS
Molecular weight	M_w
ethylenediaminetetraacetic acid	EDTA
Human cervical cancer cell	HeLa
National Centre for Cell Science	NCCS
Poly-l-lysine	PLL
Poly-l-arginine	PLA
Dulbecco's modified eagle medium	DMEM
Fetal bovine serum	FBS
2-(4-amidinophenyl) indole-6-carboamidine-dihydrochloride	DAPI
3-(4, 5-dimethylthiazol-2-yl)-2, 5-diphenyltetrazolium bromide	MTT
Tokyo chemical industry	TCI
Fluorescence	FL
Photoluminescence	P.L.
Photomultiplier tube	PMT
Circular dichroism	CD
Photoelastic modulator	PEM
Time-correlated single-photon counting	TCSPC
Light-emitting diode	LED
Deltadiode	D.D.
Dynamic light scattering	DLS
National Institutes of Health	NIH
Electron-volt	eV
Instrument response functions	IRF

Full-width at half maximum	FWHM
Fluorescein isothiocyanate	FITC
Tetramethylrhodamine	TRITC
Field Emission Scanning Electron Microscopic	FESEM
cathodoluminescence	CL
Three dimensional	3D
near-infrared fluorescence	NIRF
Two-photon	2P
White-light	WL
Three-photon	3P
That is	i.e.
Et. Cetera	etc.
Secondary electrons imaging	SEI
Energy-dispersive X-ray spectroscopy	EDS
Direct current	D.C.
Phosphate buffer saline	PBS
Nanoparticles	NPs
Molecular charge ratio	MCR
Rotations per minutes	RPM
polydispersity index	PDI
Encapsulation efficiency	EE
Emission-excitation matrix	EEM
Non-descanned detectors	NDD
Enhanced permeability and retention	EPR

SYMBOLS AND NOTATIONS

Wavelength	λ
Planck's constant	h
Length of the box	L
Mass of an electron	m
Number of electrons in the box	n
Dalton	Da
Carbon dioxide	CO_2
Watt	W
Milli-ohm	MΩ
Kilo-dalton	kDa
Hydrogen bromide	HBr
Hydrogen chloride	HCl
Energy difference	ΔE
Degree celsius	℃
Minute	min
Millimeter	mm
Nanometer	nm
Centimeter	cm
Milliliter	mL
Milligram	mg
Micromole	μM

Arbitrary unit	a.u.
Microliter	μL
Incident radiation	I_o
Transmitted radiation	I
Absorbance	A
Transmittance	T
Molar extinction coefficient	ε
Molar concentration of the sample	c
Path length of the sample cell	l
Ground state	S_0
First, second…..n^{th} excited singlet states	S_1, S_2…. S_n
Degree	°
Pi	π
Chi	χ
Femtoecond	fs
Megahertz	MHz
Weight/volume	w/v
Percentage	%
Angstrom	Å
Picosecond	ps

Chapter 1

Introduction and Background Research

1.1 Introduction

Synthetic organic dyes have been known and being synthesized since the middle of the 18th century.[1] These dyes are playing an important role in our day-to-day life, with their primary application in the textile industry.[2] The fascination of humans with colored objects inspired them to develop different synthetic dyes for various applications in the last 150 years.[3] There is still a high demand for colored molecules, not only for decorative or cosmetic purposes, but for all kinds of technologies that require strong absorption and emission of light. Additionally, Dyes have also been used for various biomedical applications, especially for the labeling and visualization of biological samples and in therapy.[4, 5] Further, dyes have been gained interest to be used in different imaging modalities and cancer therapy. The most commonly used dye in clinics is indocyanine green (ICG), which was approved for *in-vivo* clinical applications by the United States Food and Drug Administration (U.S. FDA) almost six decades ago. In this chapter, the background of the cyanine dyes specially ICG, its properties, and its various biological applications, have been discussed.

1.2 Background Research

Cyanine dyes are organic molecules containing a chain of conjugated methine groups between two nitrogen atoms with a delocalized charge. Carbocyanine dyes were first reported by C. H. G. Williams in 1856, where it was reported that the reaction between crude quinoline with 1-iodopentane in excess ammonia resulted in the discovery of vibrant blue-colored dye.[6] After that, it is generally termed as ‘cyanine,’ originating from its Greek word cyanos (meaning dark blue). Cyanine

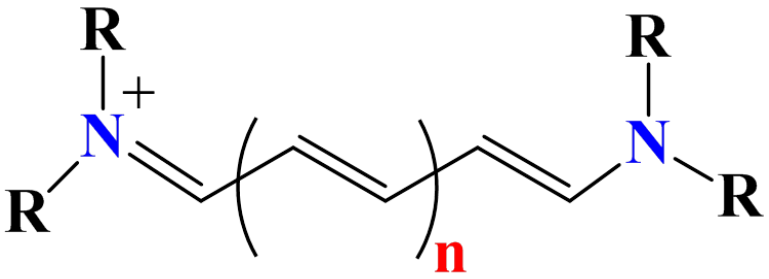

Figure 1.1 General molecular structure of the polymethine cyanine dyes.

dyes have dominated in the field of photography and other sophisticated areas of dye applications.[6, 7] Cyanine dyes belong to the family of the polymethine dyes. Generally, the polymethine dyes have two nitrogen in the center, where one of the nitrogen atoms is positively charged and is linked by a conjugated chain of an odd number of carbon atoms to the other nitrogen atom. The generic molecular structure of cyanine dyes is shown in **Figure 1.1.** The two-nitrogen atoms (denoted by blue color) are linked by a polymethine chain with variable chain length (n, denoted by red color). As it was known that organic molecules containing conjugated π–electrons typically have molecular orbitals levels, which allow the absorption of light. Similarly, cyanine dyes have been reported for a range of absorption between the visible and infrared wavelength range of the electromagnetic spectrum. Under different excitation, they give rise to distinct fluorescent emission of a particular wavelength, due to the presence of delocalized charge between two nitrogen atom, functioning as both electron acceptor and donor that are connected by the polymethine chain.[8–10]

Quantum mechanically, the cyanine dyes π–electrons in a polymethine chain can be described by the one-dimensional particle in a box model, as shown in **Figure 1.2.**[11] The energy difference (ΔE) between the highest occupied molecular orbital (HOMO) and the lowest unoccupied molecular orbital (LUMO) in a linear conjugated system is given by **Equation. 1.1.**

$$\Delta E = \frac{h^2\,(n+1)}{8mL^2} \text{.....Equation. 1.1}$$

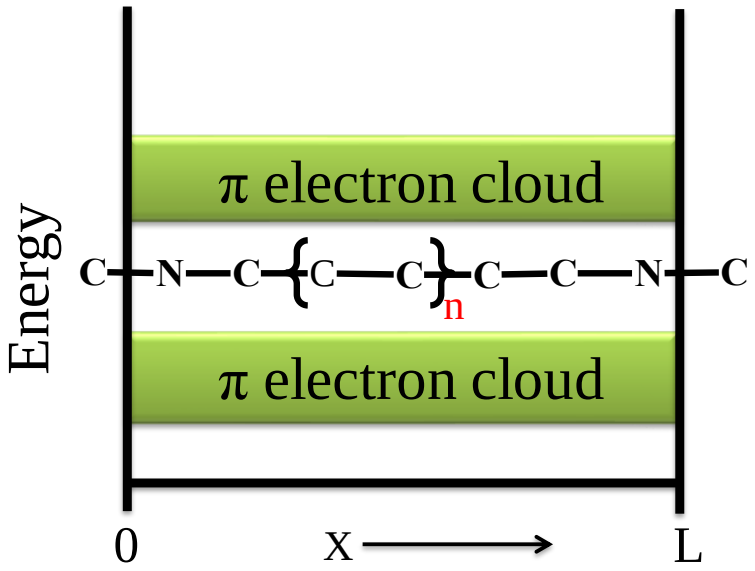

Figure 1.2 Cyanine dyes energy level diagram for a particle in a box as a function of chain length (L).

where h is the Planck's constant, L is the length of the box (i.e., length of the conjugated system), m is the mass of an electron and n is the number of electrons in the box (i.e., the number of π–electrons in the conjugated system).[12] The two parameters n and L are both related to the number of carbon atoms (N) in the system, and the HOMO–LUMO energy difference is decreasing with increasing size of the conjugated system: $\Delta E \sim 1/N$.[13, 14] One can easily calculate the wavelength, λ, corresponding to the energy gap between the HOMO-π and the LUMO-π* level from the particle-in-the-box model. A decreasing energy difference between the HOMO and LUMO suggests the redshift of the absorption, *i.e.*, from ultraviolet (UV) to visible (Vis) light, then blue to redshift, and finally into the nearinfrared (NIR) region.

Several cyanine dyes have been reported with different structures, polymethine chain length, and various functional groups in the past. Lately, a new nomenclature was introduced, i.e., 'Cy-dye', which was used to refer to a range of symmetric carbocyanine dyes.[15] Cy-dyes are named according to the number of methine groups (n = 0, 1, 2, 3) in their polymethine chain. If n = 0, 1, 2, or 3,

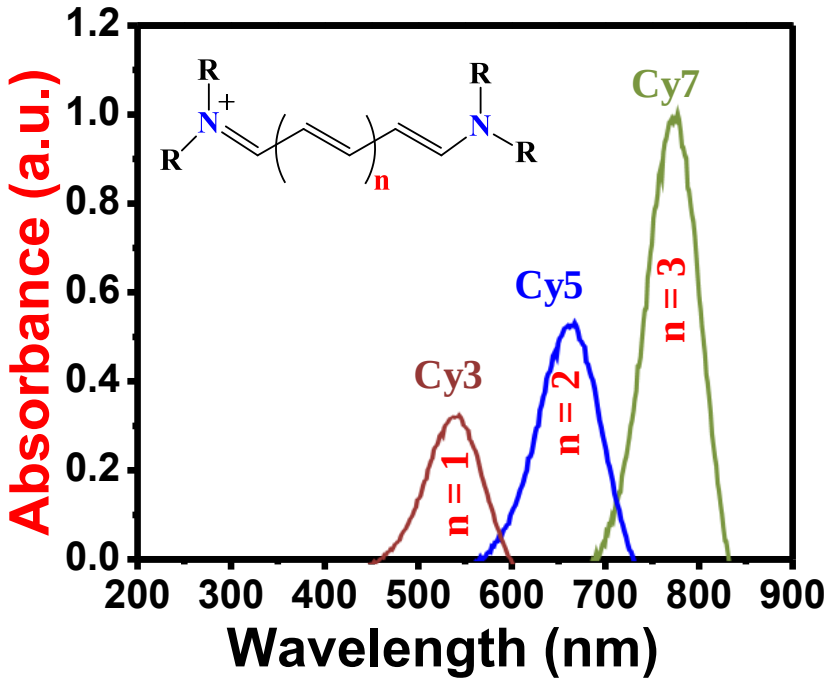

Figure 1.3 The influence of the chain length (n) on the absorption spectra of cyanine dyes. The addition of the vinylene unit in chromophore leads to a regular bathochromic shift of the band maxima.

they would be named as monomethine (Cy1), trimethine (Cy3), pentamethine (Cy5), and heptamethine (Cy7) cyanine dyes respectively. Terms like Cy3, Cy5, or Cy7 have been widely used in the literature to describe various cyanine derivatives possessing different structures and substitutions.

Generally, monomethine cyanine dyes exhibit absorption in the visible wavelength region. However, the addition of a vinylene unit (CH=CH) in the polyene-chain causes a redshift (bathochromic; shifts to longer wavelength) of about 100 nm.[16, 17] In general, Cy3 molecules absorb in the visible region, whereas there is a systematic redshift in the absorption for Cy7 (NIR region), as shown in **Figure 1.3**.[12, 18] The cyanine dyes which have small bandgap and sharp absorption band in the NIR region are desirable. Such cyanine dyes are of great interest for various biological applications.

Also, the spectral characteristics and electronic properties of polymethine cyanine dye can be modified by incorporating terminal

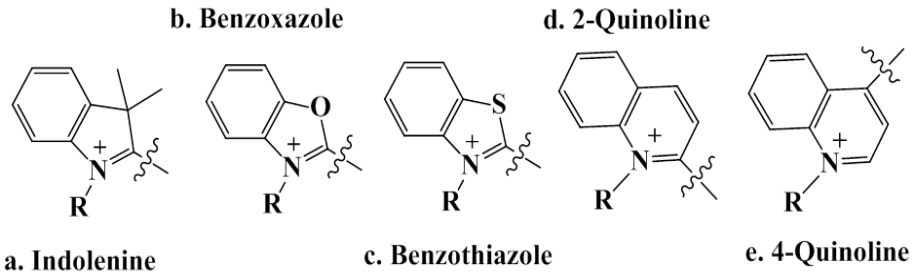

Figure 1.4 Examples of heterocyclic rings that have been used to make polymethine cyanine dyes (a) indolenines, (b) benzoxazoles, (c) benzothiazoles, (d) 2-quinolines and (e) 4-quinolones.

substituents with electron-donating or electron-accepting capabilities. Moreover, most of the polymethine chains are commonly substituted at both ends with heterocyclic groups like indolenines, benzoxazoles, benzothiazoles, 2-quinolines, 4-quinolones, *etc.* as shown in **Figure 1.4.**[19–22] Cyanine dyes have been used to enhance the spectral sensitivity of silver halide in photographic emulsions since the 18th century. They exhibit unique optical properties such as high molar extinction coefficients and tunable absorption. At the same time, they are easy to synthesize and offer great possibilities for structural modifications, so that these can be tailored to have desired properties. Substituents at various positions in the structure allow for the tuning of solubility, optical, and electrochemical properties, as well as the introduction of functional groups that react with specific targets. Nowadays, the class of cyanine dyes has grown exponentially and has been used widely as an exogenous dye for various applications due to their fluorescence properties. Additionally, there has been a dramatic increase in research on fluorescent cyanine dyes due to their applications in biology and medicine.

1.3 Introduction to ICG

Several cyanine dyes have been synthesized and used for medical applications due to their absorption and fluorescent emission properties.[23–27] However, the most popular cyanine dye for medical applications is ICG. It is the only U. S. FDA approved NIR exogenous

chromophore that has been used for various clinical applications since 1959.[28, 29] It has been utilized for measuring cardiac output, determining plasma volume, studying ophthalmic angiography, hepatic function and object localization in tissue, *etc.*[29–31]

1.3.1 Structure and Physiochemical Properties of ICG

ICG is one of the water soluble heptamethine cyanine dye, which has strong absorption and emission in the NIR region. The molecular structure of the ICG is shown in **Figure 1.5**, where the value of n is 3 in generic cyanine structure (generally called as Cy7). Also, both the ends are substituted with two indolenine rings connected by polymethine chain. The molecular weight of ICG is 775 Da. The molecule is composed of two polycyclic moieties (red shaded) at both ends, which gives ICG lipophilic property. However, the sulfate groups

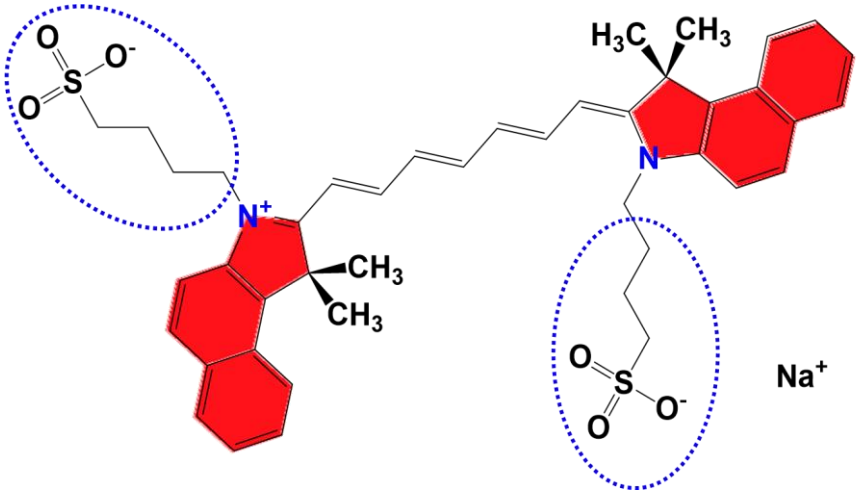

Figure 1.5 Molecular structure of free ICG.

(blue dash circle), which are connected to the polycyclic ring, endows it with the hydrophilic nature. Altogether, it is an amphiphilic molecule, which is advantageous for clinical applications.

1.3.2 Photophysical Properties of ICG

The absorption and emission spectrum of cyanine dyes is a consequence of the delocalization of the π-electrons across the polymethine unsaturated bridge system. **Figure 1.6** shows the absorption and emission spectra of aqueous ICG. ICG has the

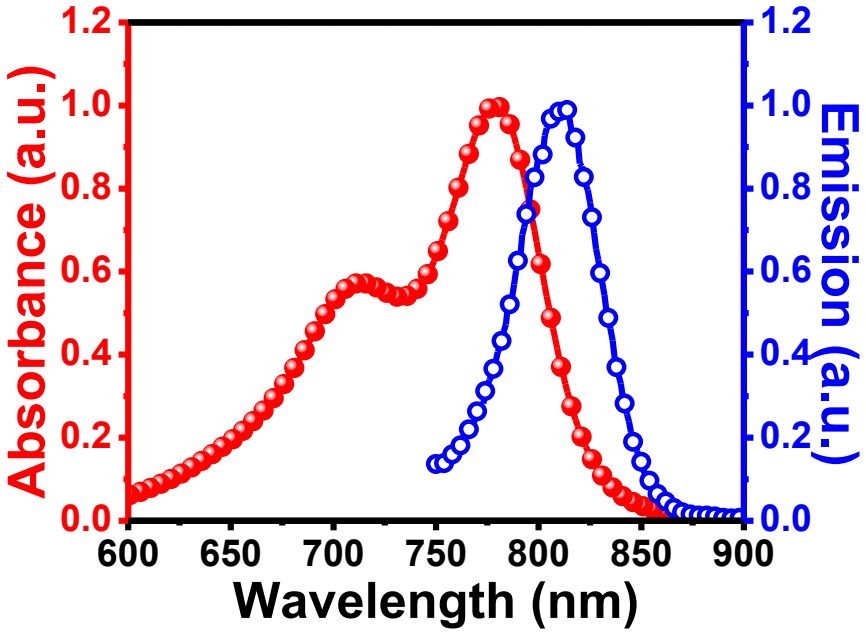

Figure 1.6 Absorption (red) and emission (blue) spectra of ICG.

absorption maxima at ~780 nm, which represents the monomeric form. The shoulder peak at ~ 710 nm represents the ICG dimeric form. ICG gives emission with maxima at ~810 nm upon 780 nm excitation.[32] Until now, the ICG has been widely used due to its NIR absorption and emission properties, but the higher energy optical properties of ICG were never discussed in the literature. In this thesis, chapter 4 describes the higher energy spectral characteristics of the ICG and its applications in biology. Generally, the spectral properties of ICG in aqueous solution depends directly on the dye concentration, temperature, light exposure, and the solvent polarity. It is prone to form aggregates at higher concentrations. The aggregates in solution exhibit distinct changes in the absorption and emission band compared to that of the monomeric form.[33]

1.3.3 Aggregation of ICG in Solution

Like other cyanine dyes, ICG tends to form aggregates, due to its tendency to possess strong intermolecular Van der Waals forces. The aggregation process depends on the concentration and solvent of the ICG. In aqueous solution, ICG monomers are prominent at lower concentrations (below ~15 µM); however, at higher concentration

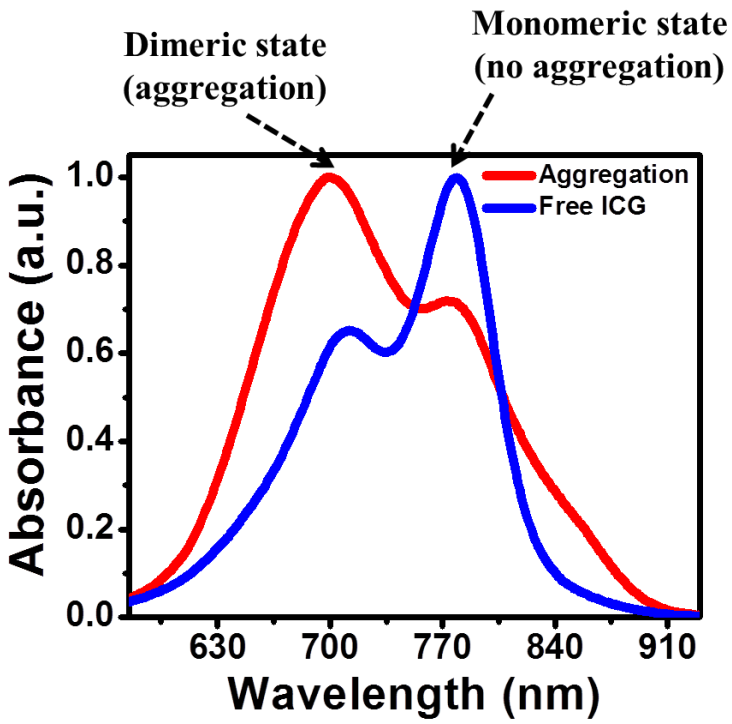

Figure 1.7 Absorption spectra of the monomeric and dimeric state of the ICG dye.

dimers and oligomers are prominent.[33, 34] In comparison to the monomeric species, the dimeric and higher-order aggregates exhibit distinct changes in the NIR absorption band in the solution. The dimeric aggregation process influences the shape of the ICG absorption spectrum in an aqueous solution that progressively takes on a mirror image, as shown in **Figure 1.7.**[35] The dimerization of the dye has been considered as the first step of aggregation.

In the aqueous solution, ICG has the tendency to form higher-order aggregates. The formation of higher-order aggregates is intrinsically associated with the spectral changes of the monomeric form of the ICG absorption band, as shown in **Figure 1.8.** Higher-order aggregates in ICG, which exhibit a hypsochromic shift (towards the blue) compared to the monomer band and termed as H-aggregates ('H' for hypsochromic).[36] Conversely, aggregates showing a bathochromic shift (towards the red) compared to the monomer spectrum of ICG is denoted as J-aggregates ('J' is named after Jelly, who was among the first to investigate these shifts).[37] The J aggregates were made up of the parallel arrangement of the ICG

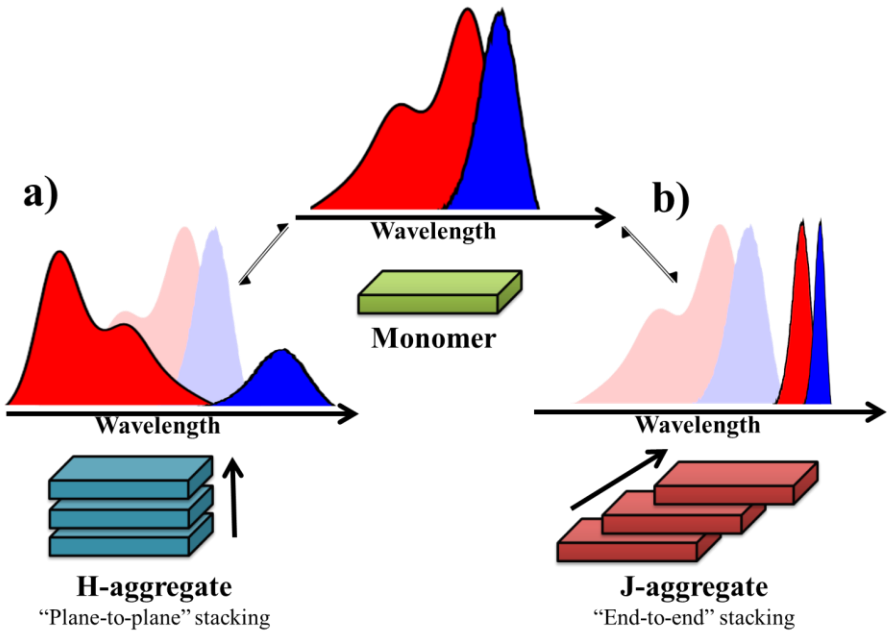

Figure 1.8 Schematic illustration of the changes in absorption (red) and fluorescence (blue) spectra during H and J-aggregates formation.

molecules, *i.e.*, stacked end-to-end forming a head-to-tail arrangement (J-dimer).[38] Similarly, the H-aggregates stacked in a plane-to-plane manner, forming a sandwich-type arrangement (H-dimer), as shown in **Figure 1.8**.[39] The formation of the H-aggregated results in the hypochromic effect in fluorescence emission and also results in poor photochemical and thermal stability. For H-aggregates, the absorption spectrum is blue-shifted relative to the monomer (green). The H-aggregates can undergo a non-radiative relaxation to the lower excited state, the fluorescence from this state is forbidden. Therefore H-aggregates are usually non-fluorescent. However, for J-aggregates (red), the absorption spectrum is red-shifted relative to the monomer, and the fluorescence is intense.

1.3.4 Applications of ICG

ICG is a U. S. FDA approved water soluble heptamethine cyanine dye. The amphiphilic nature of ICG facilitates the enhancement of its solubility in physiological fluids and its bioavailability. At first, ICG was developed by Brooker and introduced by Fox *et al.* for measuring

the cardiac output using an indicator dilution technique.[40–42] However, in the human body, ICG circulation time is very short, *i.e.*, nearly 3-5 minutes, which is due to the binding of plasma albumin and high-density lipoproteins such as alpha lipoprotein, *etc.* This results in exclusive clearance by the liver, which helps to utilize it to study hepatic function since 1958.[28, 29, 43–49] Additionally, due to its NIR absorption and fluorescence emission, it is also used for ophthalmic angiography since 1972.[30, 35, 50] Lately, ICG has been employed for controlling the thermal coagulation of the biological tissues using a diode laser.[51] Due to lower light scattering, minimal auto-fluorescence and, higher tissue penetration in biological samples, ICG (as NIR dye) has also achieved notable attention in many other fields of medicine. Nowadays, ICG has been widely employed for numerous diagnostic and therapeutic applications by virtue of its NIR optical properties. Here, biological applications of the ICG are briefly discussed for disease diagnosis and therapy.

1.3.4.1 NIR Photoacoustic Imaging

Photoacoustic imaging is a non-invasive imaging technique that brings together the significant features of optical and ultrasound techniques.[52] In contrast to other optical imaging techniques, where light must travel in and out of the biological tissue, in photoacoustic imaging, light travels only into the tissue, followed by conversion of light in pressure wave (photoacoustic effect) due to the presence of

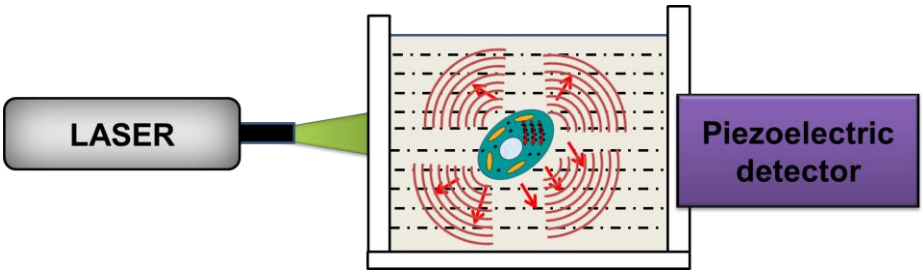

Figure 1.9 General mechanism of photoacoustic imaging, where due to light incident on biological samples, there is a rise in temperature, results in thermal expansion and generation of photoacoustic signals.

endogenous optical absorbers in the body.[53] It is a non-invasive and non-ionization imaging technique that could unveil different diseased states, including cancer.[54] When the laser light is incident on the biological samples, it results in the thermoelastic expansion in the sample volume generating the acoustic wave, as shown in **Figure 1.9**.[55] The image reconstruction is done after detecting acoustic signals by ultrasonic array transducers. The reconstructed image shows the optical absorption of the tissue. The use of UV-Vis wavelength range for imaging results in limited penetration depth, which is due to the presence of intrinsic chromophores and autofluorescence. However, the NIR illumination could help in the visualization of the deep-seated inhomogeneities due to minimal absorption and scattering from the tissue in this range. In various studies, ICG has been used as an exogenous contrast agent for photoacoustic imaging.[56–58] These studies report the significant improvement in the signal-to-noise ratio (SNR) and the contract of the imaging for early-stage cancer detection.[59] Some research studies have also shown the application of nanoencapsulated ICG for photoacoustic imaging.[60, 61] ICG in the conjugation with other metals was also employed for photoacoustic imaging.[62, 63] In 2012, ICG-enhanced single-wall carbon nanotubes were employed for photoacoustic imaging, which gave significantly high contrast in photoacoustic imaging from the animal model.[64] Additionally, various ICG loaded polymeric nanoparticles (NPs) were utilized for the photoacoustic therapy of the cancer cells.[65, 66] Huina Wang *et al.* have reported the *in-vivo* photoacoustic imaging of breast carcinoma using ICG loaded polylactic-co-glycolic acid (PLGA)-lipid NPs that were decorated with folate receptors for enhanced photoacoustic imaging.[67] Further, tissue targeting ICG loaded nanoliposomes were used for *in-vivo* clinical photoacoustic imaging by Beziere and co-workers.[68] Therefore, free and nanoencapsulated ICG has been used as a photoacoustic agent for photoacoustic imaging and therapy in recent years.[69–71]

1.3.4.2 ICG as an Exogenous Contrast Agent for NIR Imaging

Among available technologies, optical fluorescence imaging has emerged out as an effective non-invasive technique for the cancer diagnosis[72]. However, imaging with UV and Vis wavelengths suffer from the low SNR due to the interference of strong scattering and endogenous absorption of the biomolecules in this range[73]. On the other hand, imaging in the NIR wavelength range has been widely used due to the significantly lower scattering and least endogenous absorption by biological tissues in the wavelength range from 650 nm to 1100 nm, which is termed as tissue diagnostic window[5, 74]. Moreover, this wavelength range has almost zero endogenous fluorescence from biological tissues, which makes it a suitable region for deep tissue fluorescence imaging due to high SNR.[75–81] ICG has been used as a NIR exogenous dye for cancer diagnosis applications. The extensive use of ICG in molecular labeling is due to the low autofluorescence of biological tissue in the NIR spectrum and good biological compatibility of ICG as compared to other NIR dyes. Erythrocyte-derived optical nanoprobes doped with ICG demonstrated an enhanced capability of fluorescence imaging in comparison to free ICG, which can serve as potentially effective nanoprobes for the disease diagnosis.[82] Similarly, several other nanoformulations of ICG have been used for NIR imaging.[83–87]

1.3.4.3 ICG Application in Multimodal Bioimaging

Conventional imaging techniques like computed tomography, magnetic resonance imaging (MRI), ultrasound, and optical imaging (OI) are unable to provide complete structural and functional information, which leads to the emergence of multimodal imaging. In multimodal imaging, two or more imaging techniques are employed in a single examination to co-register complementary images.[88] NIR optical imaging, in combination with MRI, provides three dimensional (3D) anatomical and molecular information of the tissue with high

spatial resolution and virtually no limit on penetration depth.[89] A combination of molecular imaging with exogenous contrast agents provides high-resolution images, which helps in the early detection of cancer.[90] A variety of molecular probe has been developed for MRI and NIR fluorescence imaging. Exogenous contrast agent for both the imaging modalities was employed for better SNR.[91] MRI/NIR optical multimodal imaging is one of the best techniques due to its high sensitivity and use of nonradioactive materials.[92] Recently, utilization of the magnetic NPs as an exogenous contrast agent for MRI has been reported to enhance its sensitivity and contrast.[93] Additionally, ICG loaded magnetic resonance nanomaterials have been used for the MRI/optical concurrent imaging.[94, 95] In 2002, Lee Josephson used protease achievable iron oxide/ICG NPs as an exogenous MRI/NIR optical contrast agent for multimodal imaging.[96] Considerable interest has been shown towards MRI/NIR diffusion optical tomography imaging was done after the administration of the ICG for the precise imaging of cancer.[97]

1.3.4.4 NIR Optical Imaging Assisted Surgery

NIR fluorescence imaging is one of the potential imaging modalities in life sciences for the visualization of diseased cells and tissues, both *in-vitro* and *in-vivo*. Locating a positive margin of the diseased tissue during the surgical procedure is required for the complete removal of the diseased tissue and decrease their reoccurrence. NIR optical imaging assisted surgery is simple and provides real-time information on the diseased tissue.[98, 99] This technique combines a microscope-integrated NIR light source for the illumination of the operating area for visualization of the diseased tissue for resection.[100] In 2010, ICG mediated video angiography was used during a surgical procedure for localizing a fistula and confirm its disconnection.[101] In 2012, Fabrice P. Navarro *et al.*. report the fabrication of the 30 nm lipid NP encapsulating ICG for tumor diagnosis and lymph node resection.[102] NIR molecular imaging-guided surgery revolutionized the clinical oncology for the precision of the surgery, which maximizing tumor

excision, and minimizing the risk of metastasis or recurrence.[103–108]

1.3.4.5 Tissue Welding and Soldering

Laser tissue welding or soldering is a sutureless method of wound closure or fusing two-piece of tissue that has been used successfully in nerve, skin, and arterial anastomoses.[109] After heat generation by laser exposure, an adhesive substance is formed at the tissue edges, which form a weld upon cooling.[110] The advantages of laser welding over traditional wound closure are no foreign body reaction, less scar formation, no leakage due to suture holes, and shorter operating times.[110] However, traditional methods of laser welding have a minimal surface area of tissue to weld, such as in anastomoses.[111] The excess heating occurs with the use of traditional surgical continuous waves (CW) lasers such as the Argon and CO_2 lasers. These studies used an artificial biomaterial made mostly of elastin and fibrin to weld to the porcine aorta, which allowed greater surface area for welding and measurement of optical properties of the weld site. Later a pulsed diode laser was used to maintain thermal confinement and therefore minimizes excess heating. [112] Photosensitive dyes with high absorption at the laser wavelength are added to the weld site to increase heating and to minimize thermal damage to surrounding unstained tissue. ICG has shown its property to be utilized as a photosensitizer to assist laser welding or soldering.[113–115] Moreover, the ICG packed nano shell scaffold-based laser tissue soldering has shown the significant improvement of tissue fusion.[116] Additionally, the combination of metal and photosensitizer (gold with ICG) was used for tissue soldering, and various parameters for these techniques were optimized for effective outcomes such as laser power density, time, number of scans, *etc.*[114] Therefore, ICG could also be used as a photosensitizer for tissue welding applications.

1.3.4.6 Photothermal and Photodynamic Therapy

Photothermal therapy (PTT) is a promising laser-based approach for targeted cancer therapy by laser ablation.[117, 118] In this technique, due to the absorption of laser light of a particular wavelength, there is a localized rise in temperature.[119] The rise in temperature results in cell death, as shown in **Figure 1.10**. Several investigations have demonstrated the ability to destroy diseased cells by introducing exogenous photothermal agent, which improves the therapeutic efficiency.[120] The desirable characteristics of the agent should

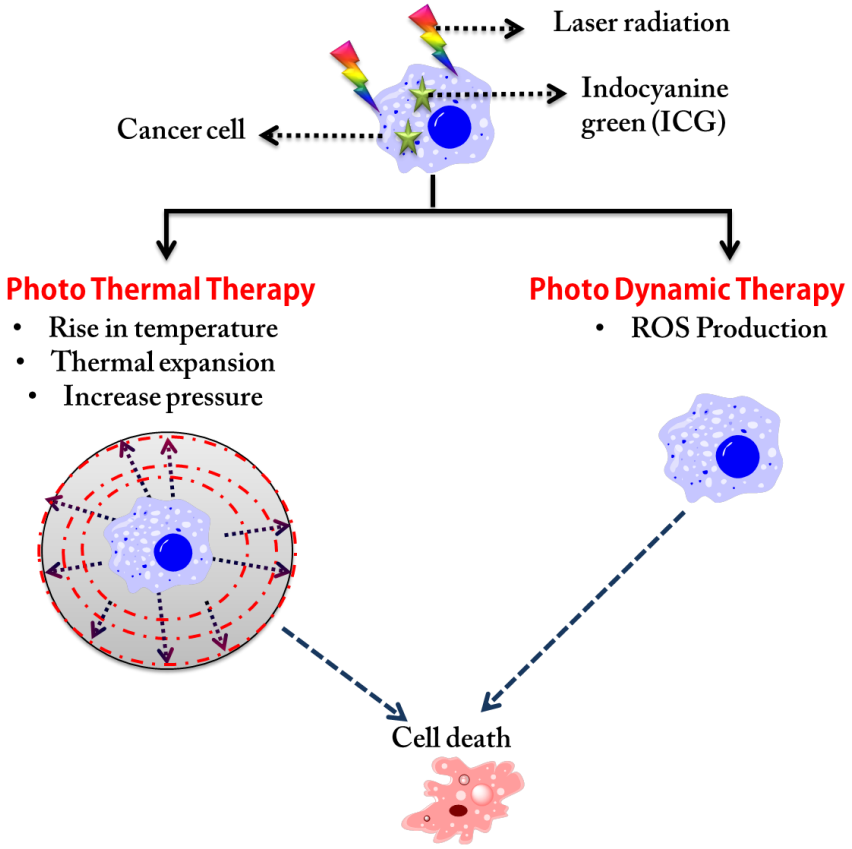

Figure 1.10 ICG mediated photothermal and photodynamic therapy.

include a strong absorption coefficient, efficient heat conversion property, high photostability, and inherent low toxicity. The short circulation time and no visible toxicity of ICG prompted an investigation of its capability to be used as a photosensitizer for therapeutic applications.[121, 122] Due to the inherent capability of producing heat upon irradiation of NIR light, ICG acts as a photothermal agent for cancer therapy.[123, 124] However, due to the

rapid degradation of the optical properties of ICG in aqueous solution, its application is limited in the clinical settings. Several reports have been published showing significant improvement in the efficiency of the encapsulated ICG for PTT, such as PLGA encapsulated ICG NPs.[125] Self-assembled ICG in phospholipid-polyethylene glycol (PL-PEG) makes a sufficient increase in temperature in contrast to free ICG. Additionally, the targeting ability of these nanocarriers was improved by conjugating integrin αvβ3 monoclonal antibody (mAb) on these NPs.[126] Similarly, targeted NPs encapsulating ICG and decorated with anti-epidermal growth factor receptor (anti-EGFR) antibodies have been reported as a proof of principle for PTT of cancer upon irradiation of 3 W/cm^2.[127] Moreover, there are several reports which show the theranostic application of ICG.[128–132] Dextran-based ICG NPs and of erythrocytes derived ICG NPs show their effectiveness for NIR imaging and PTT of cancer.[133, 134] Surface modification of NPs improves the specificity of cells, such as folic acid conjugated ICG NPs shows improved efficiency for PTT than free ICG and ICG NPs.[135]

In contrast to PTT, photodynamic therapy (PDT) uses a photosensitizer, which produces reactive oxygen species (ROS) upon exposure to light, which results in cell death at a particular site.[136] The mechanism of PDT is shown in **Figure 1.10**. ICG is a NIR active chromophore, which generates ROS upon laser irradiation results in cancer therapy.[137–139] The phototoxic effect of ICG was studied when irradiated with 809 nm diode laser on MDA-MB 231 breast cancer cell line.[140] Due to poor optical stability, ICG has not been used as a photosensitizer in clinics. Various research groups showed improved optical stability and effectiveness when ICG is delivered by nanocarriers. In this direction, many efforts have been made to encapsulate ICG in biocompatible and biodegradable material such as in polymeric, micelles, metallic, and composite NPs.[141–146] ICG loaded composite NPs have shown promising efficiency of targeting leukemia cells and have been improved the lives of leukemia

patients.[147] Further advancement has been made for targeted PDT; the nanoencapsulated ICG surface was modified with targeting moieties for targeted delivery of the ICG, which further improves the effectiveness of PDT.[148]Furthermore, ICG has been used as a photosensitizer for combinational therapy consist of photothermal and photodynamic therapies, which achieved significantly improved therapeutic efficiency.[149–152]

1.4 Focus of the Thesis

During the twenty-first century, the applications of the ICG have been remarkably increased, confirming the multifunctional role of ICG in medicine. As discussed above, ICG has been widely used as an exogenous NIR contrast agent for various biomedical applications. Despite numerous applications, the use of ICG in clinical applications is still limited. The main drawback of ICG is non-specific binding to the plasma lipoproteins resulting in the rapid elimination of ICG through the liver.[153] Additionally, the off-site delivery, undesirable aggregation, poor aqueous optical and thermal stability, and poor cellular uptake. Due to these limitations, ICG has not been used to the fullest for disease diagnosis. Nanotechnology played an important role to overcome the limitations of the ICG. However, the available ICG NPs are not completely biocompatible and showing long- and short-term toxicity. Therefore, one of the main objectives of this thesis is the development of a new fabrication technique for the reformulation of ICG in biocompatible and biodegradable NPs. A simple two-step green chemistry-based nanoencapsulation of the ICG has been done using amino acid-based homopolymers. The fabrication was done at room temperature without the involvement of any toxic reagents. The rationale behind this encapsulation is to enhance the optical stability and efficient delivery of ICG in the cells. In this thesis, ICG containing essential amino acid-based carrier has been developed. The results shown in this thesis suggest that amino acid based nanoencapsulated ICG could be used in clinics. Additionally, apart from the development of NIR active NPs for NIR bioimaging, the other major objective of

this thesis is to understand the origin of the higher energy absorption peaks of ICG and their applications. The high energy absorption bands are due to the transition of electrons to the higher energy states, namely S_2 and S_3. The electrons could be excited to these states in a nonlinear fashion and give emission upon relaxation to S_0 state. This is the first-ever study on the nonlinear excitation of the ICG and its biological applications for two-photon (2P) and three-photon(3P) bioimaging. Further, the effect of nanoencapsulation on multiphoton imaging has also been studied in this thesis.

1.5 Thesis Organization

This thesis contains six chapters. Chapter 2 describes the detailed information of the materials, methods, and working principles of used instrumentations. The cell culture technique has also been demonstrated in this chapter. Chapter 3 introduces the new formulation of the ICG to overcome its limitation for NIR bioimaging. In Chapter 4, the newly found optical properties of the ICG have been reported. These newly found optical properties of ICG have been used for the multiphoton bioimaging applications. Chapter 5 shows the effect of nanoencapsulation on multiphoton imaging. Whereas chapter 6 concludes the thesis by summarizing the results of the present study with the scope of future work.

1.6 Reference

1. Langhals H (2004) Color chemistry. synthesis, properties, and applications of organic dyes and pigments. Angew Chemie Int Ed 43:5291–5292. https://doi.org/10.1002/anie.200385122
2. Hunger K, John Wiley & Sons. (2003) Industrial dyes : chemistry, properties, applications. Wiley-VCH
3. Filarowski A (2010) Perkin's mauve: the history of the chemistry
4. Con HJ (1925) New applications of biological stains. J Chem Educ 2:184–185

5. Hilderbrand SA, Weissleder R (2010) Near-infrared fluorescence: application to in vivo molecular imaging. Curr Opin Chem Biol 14:71–79. https://doi.org/10.1016/j.cbpa.2009.09.029

6. Williams CG (1857) Researches on Chinoline and its Homologues. R Soc Edinburgh 21:377–401

7. James TH (1977) The theory of the photographic process. Macmillan

8. Hamer FM (1950) The cyanine dyes. Chem Soc 327–355. https://doi.org/10.1039/QR9500400327

9. Doja MQ (1932) The cyanine dyes. Chem Rev 11:273–321. https://doi.org/10.1213/01.ANE.0000087882.04234.11

10. Hamer FM, Heilbron IM, Reade JH, Walls HN (1932) Cyanine dyes and related compounds. J Chem Soc 0:251–260

11. Autschbach J (2007) Why the Particle-in-a-Box Model Works Well for Cyanine Dyes but Not for Conjugated Polyenes. J Chem Educ 84:1840. https://doi.org/10.1021/ed084p1840

12. Simpson WT (1948) Electronic states of organic molecules. J Chem Phys 16:1124–1136. https://doi.org/10.1063/1.1746743

13. Brooker LGS, Keyes GH, Williams WW (1942) Color and Constitution. V. [1] The Absorption of Unsymmetrical Cyanines. Resonance as a Basis for a Classification of Dyes. J Am Chem Soc 64:199–210. https://doi.org/10.1021/ja01254a002

14. Kuhn H (1949) A Quantum-Mechanical Theory of Light Absorption of Organic Dyes and Similar Compounds. J Chem Phys 17:1198–1212. https://doi.org/10.1063/1.1747143

15. Ernst LA, Gupta RK, Mujumdar RB, Waggoner AS (1989) Cyanine dye labeling reagents for sulfhydryl groups. Cytometry 10:3–10. https://doi.org/10.1002/cyto.990100103

16. Kuhn H (1949) A quantum-mechanical theory of light

absorption of organic dyes and similar compounds. J Chem Phys 17:1198–1212. https://doi.org/10.1063/1.1747143

17. Przhonska O V., Hu H, Webster S, *et al.* (2013) Electronic transitions in a series of 2-azaazulene polymethine dyes with different π-conjugation lengths. Chem Phys 411:17–25. https://doi.org/10.1016/j.chemphys.2012.11.017

18. Bricks JL, Slominskii YL, Panas ID, Demchenko AP (2018) Fluorescent J-aggregates of cyanine dyes: Basic research and applications review. Methods Appl Fluoresc 6:. https://doi.org/10.1088/2050-6120/aa8d0d

19. Shershov VE, Spitsyn MA, Kuznetsova VE, *et al.* (2013) Near-infrared heptamethine cyanine dyes. Synthesis, spectroscopic characterization, thermal properties and photostability. Dye Pigment 97:353–360. https://doi.org/10.1016/J.DYEPIG.2012.12.031

20. Wang L, Xiang J, Sun H, *et al.* (2015) Controllable cy3-MTC-dye aggregates and its applications served as a chemosensor. Dye Pigment 122:382–388. https://doi.org/10.1016/J.DYEPIG.2015.07.018

21. Chen X, Peng X, Cui A, *et al.* (2006) Photostabilities of novel heptamethine 3H-indolenine cyanine dyes with different N-substituents. J Photochem Photobiol A Chem 181:79–85. https://doi.org/10.1016/J.JPHOTOCHEM.2005.11.004

22. Yarmoluk S, Kovalska VB (2011) Advanced Fluorescence Reporters in Chemistry and Biology III

23. Fortina P, Delgrosso K, Sakazume T, *et al.* (2000) Simple two-color array-based approach for mutation detection. Eur J Hum Genet 8:884–894. https://doi.org/10.1038/sj.ejhg.5200558

24. Rye HS, Yue S, Wemmer DE, *et al.* (1992) Stable fluorescent complexes of double-stranded DNA with bis-intercalating asymmetric cyanine dyes: Properties and applications. Nucleic

Acids Res 20:2803–2812. https://doi.org/10.1093/nar/20.11.2803

25. Deligeorgiev T, Vasilev A (2006) Cyanine dyes as fluorescent non-covalent labels for nucleic acid research. In: Functional Dyes. pp 137–183

26. Zeng Z, Benson SC, Glazer AN (1995) Fluorescence energy-transfer cyanine heterodimers with high affinity for double-stranded DNA. II. Applications to multiplex restriction fragment sizing. Anal Biochem 231:256–260. https://doi.org/10.1006/abio.1995.1528

27. Tatikolov AS (2012) Polymethine dyes as spectral-fluorescent probes for biomacromolecules. J. Photochem. Photobiol. C Photochem. Rev. 13:55–90

28. Wheeler HO, Cranston WI, Meltzer JI (1958) Hepatic uptake and biliary excretion of indocyanine green in the dog. Proc Soc Exp Biol Med Soc Exp Biol Med 99:11–4

29. Gilbert Cherrick BR, Stein SW, Leevy CM, Davidson CS (1959) Indocyanine green: observations on its physical properties, plasma decay, and hepatic extraction

30. Benson RC, Kues HA (1978) Fluorescence properties of indocyanine green as related to angiography. Phys Med Biol 23:017. https://doi.org/10.1088/0031-9155/23/1/017

31. Haruna M, Kumon K, Yahagi N, *et al.* (1998) Blood volume measurement at the bedside using ICG pulse spectrophotometery. Anesthesiology 89:1322–8. https://doi.org/10.1167/8.5.1.

32. Lipowska M, Patonay G, Strekowski L (1993) New near-infrared cyanine dyes for labelling of proteins. Synth Commun 23:3087–3094. https://doi.org/10.1080/00397919308011153

33. Behera GB, Behera PK, Mishra BK (2007) Cyanine dyes : Self aggregation and behaviour in surfactants: A review. J Surf Sci

Technol 23:1–31

34. Zhou JF, Chin MP, Schafer SA Aggregation and degradation of indocyanine green. 2128:

35. Desmettre T, Devoisselle JM, Mordon S (2000) Fluorescence properties and metabolic features of indocyanine green (ICG) as related to angiography. Surv Ophthalmol 45:15–27. https://doi.org/10.1016/S0039-6257(00)00123-5

36. Brooker LGS (1948) CHEMISTRY OF THE CYANINE DYES. Ann N Y Acad Sci 50:108–108. https://doi.org/10.1111/j.1749-6632.1948.tb39843.x

37. Jelley EE (1936) Spectral absorption and fluorescence of dyes in the molecular state. Nature 138:1009–1010

38. Rotermund F, Weigand R, Penzkofer A (1997) J-aggregation and disaggregation of indocyanine green in water. Chem Phys 220:385–392. https://doi.org/10.1016/S0301-0104(97)00151-1

39. Mishra,Amaresh, Behera,Rajani K., Behera,Pradipta K., *et al.* (2000) Cyanines during the 1990s: A Review. Chem Rev 100:1973–2012. https://doi.org/10.1021/cr990402t

40. Fox IJ, Wood EH (1957) Applications of dilution curves recorded from the right side of the heart or venous circulation with the aid of a new indicator dye. Proc Staff Meet Mayo Clin 32:541–50

41. Fox IJ, Brooker LG, Heseltine DW, *et al.* (1957) A tricarbocyanine dye for continuous recording of dilution curves in whole blood independent of variations in blood oxygen saturation. Proc Staff Meet Mayo Clin 32:478–84

42. Maarek JMI, Holschneider DP, Harimoto J, *et al.* (2004) Measurement of cardiac output with indocyanine green transcutaneous fluorescence dilution technique. Anesthesiology 100:1476–1483. https://doi.org/10.1097/00000542-200406000-00020

43. Caesar J, Shaldon S, Chiandussi L, *et al.* (1961) The use of indocyanine green in the measurement of hepatic blood flow and as a test of hepatic function. Clin Sci 21:43–57

44. Leevy CM, Mendenhall CL, Lesko W, Howard MM (1962) Estimation of hepatic blood flow with indocyanine green. J Clin Invest 41:1169–1179

45. van Berge-Henegouwen GP, Ferguson DR, Hofmann AF, De Pagter AGF (1978) Familial and nonfamilial benign recurrent cholestasis distinguished by plasma disappearance of indocyanine green but not cholylglycine. Gut 19:345–349. https://doi.org/10.1136/gut.19.5.345

46. El-Desoky A, Seifalian AM, Cope M, *et al.* (1999) Experimental study of liver dysfunction evaluated by direct indocyanine green clearance using near infrared spectroscopy. Br J Surg 86:1005–1011. https://doi.org/10.1046/j.1365-2168.1999.01186.x

47. Jarrar D, Wang P, Song GY, *et al.* (2000) Metoclopramide: a novel adjunct for improving cardiac and hepatocellular functions after trauma-hemorrhage. Am J Physiol Endocrinol Metab 278:E90–E95

48. Sourisa JS, Leeb C-H, Cheng S-H, *et al.* (2010) Surface Charge-Mediated Rapid Hepatobiliary Excretion of Mesoporous Silica Nanoparticles. Biomaterials 31:5564–5574. https://doi.org/10.1016/j.biomaterials.2010.03.048.Surface

49. Halle BM, Poulsen TD, Pedersen HP (2014) Indocyanine green plasma disappearance rate as dynamic liver function test in critically ill patients. Acta Anaesthesiol Scand 58:1214–1219. https://doi.org/10.1111/aas.12406

50. Tadayoni R, Paques M, Girmens JF, *et al.* (2003) Persistence of fundus fluorescence after use of indocyanine green for macular surgery. Ophthalmology 110:604–608. https://doi.org/10.1016/S0161-6420(02)01761-X

51. Mordon S, Desmettre T, Devoisselle JM, Soulie S (1996) Fluorescence Measurement of 805 nm Laser-Induced Release of 5,6-CF From DSPC Liposomes for Real-Time Monitoring of Temperature: An In Vivo Study in Rat Liver Using lndocyanine Green Potentiation. Lasers Surg Med 18:265–270. https://doi.org/10.1143/JPSJ.13.227

52. Zhang R, Pan D, Cai X, *et al.* (2015) αvβ3-targeted Copper Nanoparticles Incorporating an Sn 2 Lipase-Labile Fumagillin Prodrug for Photoacoustic Neovascular Imaging and Treatment. Theranostics 5:124–133. https://doi.org/10.7150/thno.10014

53. Tam AC (1986) Applications of photoacoustic sensing techniques. Rev Mod Phys 58:381–431. https://doi.org/10.1103/RevModPhys.58.381

54. Stantz KM, Liu B, Cao M, *et al.* (2006) Photoacoustic spectroscopic imaging of intra-tumor heterogeneity and molecular identification. Proceeding SPIE 6086:8605. https://doi.org/Artn 608605\rDoi 10.1117/12.645106

55. Bell AG (1880) On the production and reproduction of sound by light. Am J Sci s3-20:305–324. https://doi.org/10.2475/ajs.s3-20.118.305

56. Kim G, Huang S-W, Day KC, *et al.* (2007) Indocyanine-green-embedded PEBBLEs as a contrast agent for photoacoustic imaging. J Biomed Opt 12:044020. https://doi.org/10.1117/1.2771530

57. Kohl Y, Kaiser C, Bost W, *et al.* (2011) Near-infrared dye-loaded PLGA nanoparticles prepared by spray drying for photoacoustic applications. Int J Artif Organs 34:249–254. https://doi.org/10.5301/IJAO.2011.6405

58. Proskurnin MA, Zhidkova T V., Volkov DS, *et al.* (2011) In vivo multispectral photoacoustic and photothermal flow cytometry with multicolor dyes: A potential for real-time assessment of circulation, dye-cell interaction, and blood

volume. Cytom Part A 79 A:834–847. https://doi.org/10.1002/cyto.a.21127

59. Yoon HK, Ray A, Koo Lee YE, *et al.* (2013) Polymer-protein hydrogel nanomatrix for stabilization of indocyanine green towards targeted fluorescence and photoacoustic bio-imaging. J Mater Chem B 1:5611–5619. https://doi.org/10.1039/c3tb21060j

60. Fukasawa T, Hashimoto M, Nagamine S, *et al.* (2014) Fabrication of ICG Dye-containing Particles by Growth of Polymer/Salt Aggregates and Measurement of Photoacoustic Signals. Chem Lett 43:495–497. https://doi.org/10.1097/ALN.0000000000001828

61. Kanazaki K, Sano K, Makino A, *et al.* (2014) Development of human serum albumin conjugated with near-infrared dye for photoacoustic tumor imaging. J Biomed Opt 19:096002. https://doi.org/10.1117/1.JBO.19.9.096002

62. Gao C, Deng Z-J, Peng D, *et al.* (2016) Near-infrared dye-loaded magnetic nanoparticles as photoacoustic contrast agent for enhanced tumor imaging. Cancer Biol Med 13:349–359. https://doi.org/10.20892/j.issn.2095-3941.2016.0048

63. Ferrauto G, Carniato F, Di Gregorio E, *et al.* (2017) Large photoacoustic effect enhancement for ICG confined inside MCM-41 mesoporous silica nanoparticles. Nanoscale 9:99–103. https://doi.org/10.1039/c6nr08282c

64. May Y, Tabakman SM, Liu Z, *et al.* (2012) Family of Enhanced Photoacoustic Imaging Agents for High-Sensitivity and Multiplexing Studies in Living Mice. ACS Nano 6:4694–4701. https://doi.org/10.1021/nn204352r

65. Zhong J, Yang S, Zheng X, *et al.* (2013) In vivo photoacoustic therapy with cancer-targeted indocyanine green-containing nanoparticles. Nanomedicine 8:903–919. https://doi.org/10.2217/nnm.12.123

66. Wang G, Zhang F, Tian R, *et al.* (2016) Nanotubes-Embedded Indocyanine Green–Hyaluronic Acid Nanoparticles for Photoacoustic-Imaging-Guided Phototherapy. ACS Appl Mater Interfaces 8:5608–5617. https://doi.org/10.1186/s40945-017-0033-9.Using

67. Wang H, Liu C, Gong X, *et al.* (2014) In vivo photoacoustic molecular imaging of breast carcinoma with folate receptor-targeted indocyanine green nanoprobes. Nanoscale 6:14270–14279. https://doi.org/10.1039/c4nr03949a

68. Beziere N, Lozano N, Nunes A, *et al.* (2015) Dynamic imaging of PEGylated indocyanine green (ICG) liposomes within the tumor microenvironment using multi-spectral optoacoustic tomography (MSOT). Biomaterials 37:415–424. https://doi.org/10.1016/j.biomaterials.2014.10.014

69. Sano K, Ohashi M, Kanazaki K, *et al.* (2015) In vivo photoacoustic imaging of cancer using indocyanine green-labeled monoclonal antibody targeting the epidermal growth factor receptor. Biochem Biophys Res Commun 464:820–825. https://doi.org/10.1016/j.bbrc.2015.07.042

70. Lu HD, Wilson BK, Heinmiller A, *et al.* (2016) Narrow Absorption NIR Wavelength Organic Nanoparticles Enable Multiplexed Photoacoustic Imaging. ACS Appl Mater Interfaces 8:14379–14388. https://doi.org/10.1021/acsami.6b03059

71. Oddo L, Cerroni B, Domenici F, *et al.* (2017) Next generation ultrasound platforms for theranostics. J Colloid Interface Sci 491:151–160. https://doi.org/10.1016/j.jcis.2016.12.030

72. Weissleder R (2002) Scaling Down Imaging: Molecular Mapping of Cancer in Mice. Nat Rev Cancer 2:11–18. https://doi.org/10.1038/nrc701

73. Zhang H, Kim DM, Tai Y, *et al.* (2016) Penetration depth of photons in biological tissues from hyperspectral imaging in shortwave infrared in transmission and reflection geometries. J

Biomed Opt 21:126006 (1–10). https://doi.org/10.1117/1.JBO.21.12.126006

74. Weissleder R (2001) A Clearer Vision for in vivo Imaging. Nat Biotechnol 19:316–317. https://doi.org/10.1038/86684

75. Ke S, Wen X, Gurfinkel M, *et al.* (2003) Near-infrared optical imaging of epidermal growth factor receptor in breast cancer xenografts. Cancer Nanotechnol 63:7870–7875

76. Moon WK, Lin Y, O'Loughlin T, *et al.* (2003) Enhanced tumor detection using a folate receptor-targeted near-infrared fluorochrome conjugate. Bioconjug Chem 14:539–545. https://doi.org/10.1021/bc0340114

77. Becker A, Hessenius C, Licha K, *et al.* (2001) Receptor-targeted optical imaging of tumors with near-infrared fluorescent ligands. Nat Biotechnol 19:327–331. https://doi.org/10.1038/86707

78. Tung CH, Bredow S, Mahmood U, Weissleder R (1999) Preparation of a cathepsin D sensitive near-infrared fluorescence probe for imaging. Bioconjug Chem 10:892–896. https://doi.org/10.1021/bc990052h

79. Ballou B, Fisher GW, Hakala TR, Farkas DL (1997) Tumor detection and visualization using cyanine fluorochrome-labeled antibodies. Biotechnol Prog 13:649–658. https://doi.org/10.1021/bp970088t

80. Sevick-muraca EM, Houston JP, Gurfinkel M (2002) Fluorescence-enhanced , near infrared diagnostic imaging with contrast agents. Curr Opin Chem Biol 6:642–650

81. Hellebust A, Richards-Kortum R (2012) Advances in molecular imaging : targeted optical contrast agents for cancer diagnostics. Nanomedicine 7:429–445

82. Mac JT, Vankayala R, Patel DK, *et al.* (2018) Erythrocyte-Derived Optical Nanoprobes Doped with Indocyanine Green-Bound Albumin: Material Characteristics and Evaluation for

Cancer Cell Imaging. ACS Biomater Sci Eng 4:3055–3062. https://doi.org/10.1021/acsbiomaterials.8b00621

83. Mac JT, Nuñez V, Burns JM, *et al.* (2016) Erythrocyte-derived nano-probes functionalized with antibodies for targeted near infrared fluorescence imaging of cancer cells. Biomed Opt Express 7:1311. https://doi.org/10.1364/BOE.7.001311

84. Rodriguez VB, Henry SM, Hoffman AS, *et al.* (2008) Encapsulation and stabilization of indocyanine green within poly(styrene-alt-maleic anhydride) block-poly(styrene) micelles for near-infrared imaging. J Biomed Opt 13:014025. https://doi.org/10.1117/1.2834296

85. Frangioni J V. (2003) In vivo near-infrared fluorescence imaging. Curr Opin Chem Biol 7:626–634. https://doi.org/10.1016/j.cbpa.2003.08.007

86. Lim YT, Noh YW, Han JH, *et al.* (2008) Biocompatible polymer-nanoparticle-based bimodal imaging contrast agents for the labeling and tracking of dendritic cells. Small 4:1640–1645. https://doi.org/10.1002/smll.200800582

87. Xu RX, Huang J, Xu JS, *et al.* (2009) Fabrication of indocyanine green encapsulated biodegradable microbubbles for structural and functional imaging of cancer. J Biomed Opt 14:034020. https://doi.org/10.1117/1.3147424

88. Li Z, Yin S, Cheng L, *et al.* (2014) Magnetic targeting enhanced theranostic strategy based on multimodal imaging for selective ablation of cancer. Adv Funct Mater 24:2312–2321. https://doi.org/10.1002/adfm.201303345

89. Santra S, Kaittanis C, Grimm J, Perez JM (2009) Drug/dye-loaded, multifunctional iron oxide nanoparticles for combined targeted cancer therapy and dual optical/magnetic resonance imaging. Small 5:1862–1868. https://doi.org/10.1002/smll.200900389

90. Sharma P, Bengtsson NE, Walter GA, *et al.* (2012) Gadolinium-doped silica nanoparticles encapsulating indocyanine green for near infrared and magnetic resonance imaging. Small 8:2856–2868. https://doi.org/10.1002/smll.201200258

91. Fang C, Zhang M (2009) Multifunctional magnetic nanoparticles for medical imaging applications. J Mater Chem 19:6258–6266. https://doi.org/10.1039/b902182e

92. Kim HM, Lee H, Hong KS, *et al.* (2011) Synthesis and High Performance of Nanocomposites as MR / Near-Infrared Multimodal Cellular Imaging Nanoprobes. ACS Nano 5:8230–8240

93. Shi X, Wang SH, Swanson SD, *et al.* (2008) Dendrimer-functionalized shell-crosslinked iron oxide nanoparticles for in-vivo magnetic resonance imaging of tumors. Adv Mater 20:1671–1678. https://doi.org/10.1002/adma.200702770

94. Park H, Yang J, Seo S, *et al.* (2008) Multifunctional nanoparticles for photothermally controlled drug delivery and magnetic resonance imaging enhancement. Small 4:192–196. https://doi.org/10.1002/smll.200700807

95. Ravoori MK, Singh S, Bhavane R, *et al.* (2016) Multimodal Magnetic Resonance and Near-Infrared-Fluorescent Imaging of Intraperitoneal Ovarian Cancer Using a Dual-Mode-Dual-Gadolinium Liposomal Contrast Agent. Sci Rep 6:1–11. https://doi.org/10.1038/srep38991

96. Josephson L, Kircher MF, Mahmood U, *et al.* (2002) Near-infrared fluorescent nanoparticles as combined MR/optical imaging probes. Bioconjug Chem 13:554–560. https://doi.org/10.1021/bc015555d

97. Ntziachristos V, Yodh AG, Schnall M, Chance B (2000) Concurrent MRI and diffuse optical tomography of breast after indocyanine green enhancement. Proc Natl Acad Sci 97:2767–2772. https://doi.org/10.1073/pnas.040570597

98. Alander JT, Kaartinen I, Laakso A, *et al.* (2012) A Review of indocyanine green fluorescent imaging in surgery. Int J Biomed Imaging 2012:26. https://doi.org/10.1155/2012/940585

99. Tsuchimochi M, Hayama K, Toyama M, *et al.* (2013) Dual-modality imaging with99mTc and fluorescent indocyanine green using surface-modified silica nanoparticles for biopsy of the sentinel lymph node: An animal study. EJNMMI Res 3:1–11. https://doi.org/10.1186/2191-219X-3-33

100. Hill TK, Abdulahad A, Kelkar SS, *et al.* (2015) Indocyanine green-loaded nanoparticles for image-guided tumor surgery. Bioconjug Chem 26:294–303. https://doi.org/10.1021/bc5005679

101. Hanel RA, Nakaji P, Spetzler RF (2010) Use of Microscope-Integrated Near-Infrared Indocyanine Green Videoangiography in the Surgical Treatment of Spinal Dural Arteriovenous Fistulae. Neurosurgery 66:984–985. https://doi.org/10.1227/01.NEU.0000368108.94233.22

102. Navarro FP, Berger M, Guillermet S, *et al.* (2012) Lipid nanoparticle vectorization of IndoCyanine Green improves fluorescence imaging for tumor diagnosis and lymph node resection. J Biomed Nanotechnol 8:730–741. https://doi.org/10.1166/jbn.2012.1430

103. Bu L, Shen B, Cheng Z (2014) Fluorescent imaging of cancerous tissues for targeted surgery. Adv Drug Deliv Rev 76:21–38. https://doi.org/10.1016/j.addr.2014.07.008

104. De la Garza-Ramos R, Bydon M, Macki M, *et al.* (2014) Fluorescent techniques in spine surgery. Neurol Res 36:928–938. https://doi.org/10.1179/1743132814Y.0000000340

105. Kong SH, Noh YW, Suh YS, *et al.* (2015) Evaluation of the novel near-infrared fluorescence tracers pullulan polymer nanogel and indocyanine green/γ-glutamic acid complex for sentinel lymph node navigation surgery in large animal models.

Gastric Cancer 18:55–64. https://doi.org/10.1007/s10120-014-0345-3

106. Zeng C, Shang W, Wang K, *et al.* (2016) Intraoperative identification of liver cancer microfoci using a targeted near-infrared fluorescent probe for imaging-guided surgery. Sci Rep 6:1–10. https://doi.org/10.1038/srep21959

107. Porcu EP, Salis A, Rassu G, *et al.* (2017) Engineered polymeric microspheres obtained by multi-step method as potential systems for transarterial embolization and intraoperative imaging of HCC: Preliminary evaluation. Eur J Pharm Biopharm 117:160–167. https://doi.org/10.1016/j.ejpb.2017.04.010

108. Guan T, Shang W, Li H, *et al.* (2017) From Detection to Resection: Photoacoustic Tomography and Surgery Guidance with Indocyanine Green Loaded Gold Nanorod@liposome Core-Shell Nanoparticles in Liver Cancer. Bioconjug Chem 28:1221–1228. https://doi.org/10.1021/acs.bioconjchem.7b00065

109. HW P, MC O, LS B, *et al.* (1989) Welding of gallbladder tissue with a pulsed 2.15 micronsthulium-holmium-chromium:YAG laser. Lasers Surg Med 9:155–159

110. Murray LW, Su L, Kopchok GE, White RA (1989) Crosslinking of extracellular matrix proteins: a preliminary report on a possible mechanism of argon laser welding. Lasers Surg Med 9:490–6

111. McCue JL, Phillips RKS (1991) Sutureless intestinal anastomoses. Br J Surg 78:1291–1296

112. Naomi E, Joie L (1992) Tissue Welding : Studies of Pulsed Diode Laser Interaction with ICG Stained Porcine Aorta and Elastin-Based Biomaterial

113. DeCoste SD, Farinelli W, Flotte T, Anderson RR (1992) Dye-

enhanced laser welding for skin closure. Lasers Surg Med 12:25–32. https://doi.org/10.1002/lsm.1900120107

114. Khosroshahi ME, Nourbakhsh MS (2011) Enhanced laser tissue soldering using indocyanine green chromophore and gold nanoshells combination. J Biomed Opt 16:088002. https://doi.org/10.1117/1.3611001

115. Schiavon M, Marulli G, Zuin A, *et al.* (2013) Experimental evaluation of a new system for laser tissue welding applied on damaged lungs. Interact Cardiovasc Thorac Surg 16:577–582. https://doi.org/10.1093/icvts/ivt029

116. Schöni DS, Bogni S, Bregy A, *et al.* (2011) Nanoshell assisted laser soldering of vascular tissue. Lasers Surg Med 43:975–983. https://doi.org/10.1002/lsm.21140

117. Cheng L, Yang K, Chen Q, Liu Z (2012) Organic Stealth Nanoparticles for Highly Effective in Vivo Near-Infrared Photothermal Therapy of Cancer. ACS Nano 6:5605–5613. https://doi.org/10.1039/c0nr00299b

118. Yang K, Xu H, Cheng L, *et al.* (2012) In vitro and in vivo near-infrared photothermal therapy of cancer using polypyrrole organic nanoparticles. Adv Mater 24:5586–5592. https://doi.org/10.1002/adma.201202625

119. Cheng L, He W, Gong H, *et al.* (2013) PEGylated micelle nanoparticles encapsulating a non-fluorescent near-infrared organic dye as a safe and highly-effective photothermal agent for in vivo cancer therapy. Adv Funct Mater 23:5893–5902. https://doi.org/10.1002/adfm.201301045

120. Chitgupi U, Qin Y, Lovell JF (2017) Targeted Nanomaterials for Phototherapy. Nanotheranostics 1:38–58. https://doi.org/10.7150/ntno.17694

121. Yaseen MA, Diagaradjane P, Pikkula BM, *et al.* (2005) Photothermal and photochemical effects of laser light absorption

by indocyanine green (ICG). Proc SPIE 5695:27–35. https://doi.org/10.1117/12.589702

122. Fernandez-Fernandez A, Manchanda R, Lei T, *et al.* (2012) Comparative study of the optical and heat generation properties of IR820 and indocyanine green. Mol Imaging 11:99–113. https://doi.org/10.2310/7290.2011.00031

123. Yaseen MA, Yu J, Wong MS, Anvari B (2007) Laser-induced heating of dextran-coated mesocapsules containing indocyanine green. Biotechnol Prog 23:1431–1440. https://doi.org/10.1021/bp0701618

124. Sato T, Ito M, Ishida M, Karasawa Y (2010) Phototoxicity of indocyanine green under continuous fluorescent lamp illumination and its prevention by blocking red light on cultured müller cells. Investig Ophthalmol Vis Sci 51:4337–4345. https://doi.org/10.1167/iovs.09-4707

125. Patel RH, Wadajkar AS, Patel NL, *et al.* (2012) Multifunctionality of indocyanine green-loaded biodegradable nanoparticles for enhanced optical imaging and hyperthermia intervention of cancer. J Biomed Opt 17:046003. https://doi.org/10.1117/1.JBO.17.4.046003

126. Zheng X, Zhou F, Wu B, *et al.* (2012) Enhanced tumor treatment using biofunctional indocyanine green-containing nanostructure by intratumoral or intravenous injection. Mol Pharm 9:514–522. https://doi.org/10.1021/mp200526m

127. Yu J, Javier D, Yaseen MA, *et al.* (2010) Self-assembly synthesis, tumor cell targeting, and photothermal capabilities of antibody-coated indocyanine green nanocapsules. J Am Chem Soc 132:1929–1938. https://doi.org/10.1021/ja908139y

128. Wu L, Fang S, Shi S, *et al.* (2013) Hybrid polypeptide micelles loading indocyanine green for tumor imaging and photothermal effect study. Biomacromolecules 14:3027–3033. https://doi.org/10.1021/bm400839b

129. Bahmani B, Bacon D, Anvari B (2013) Erythrocyte-derived photo-theranostic agents: Hybrid nano-vesicles containing indocyanine green for near infrared imaging and therapeutic applications. Sci Rep 3:1–7. https://doi.org/10.1038/srep02180

130. Li J, Jiang H, Yu Z, *et al.* (2013) Multifunctional uniform core-shell Fe3O4@mSiO2mesoporous nanoparticles for bimodal imaging and photothermal therapy. Chem - An Asian J 8:385–391. https://doi.org/10.1002/asia.201201033

131. Yue C, Liu P, Zheng M, *et al.* (2013) IR-780 dye loaded tumor targeting theranostic nanoparticles for NIR imaging and photothermal therapy. Biomaterials 34:6853–6861. https://doi.org/10.1016/j.biomaterials.2013.05.071

132. Sheng Z, Hu D, Zheng M, *et al.* (2014) Smart human serum albumin-indocyanine green nanoparticles generated by programmed assembly for dual-modal imaging-guided cancer synergistic phototherapy. ACS Nano 8:12310–12322. https://doi.org/10.1021/nn5062386

133. Liu P, Yue C, Shi B, *et al.* (2013) Dextran based sensitive theranostic nanoparticles for near-infrared imaging and photothermal therapy in vitro. Chem Commun 49:6143–6145. https://doi.org/10.1039/c3cc43633k

134. Burns JM, Vankayala R, Mac JT, Anvari B (2018) Erythrocyte-Derived Theranostic Nanoplatforms for Near Infrared Fluorescence Imaging and Photodestruction of Tumors. ACS Appl Mater Interfaces 10:27621–27630. https://doi.org/10.1021/acsami.8b08005

135. Zheng M, Zhao P, Luo Z, *et al.* (2014) Robust ICG theranostic nanoparticles for folate targeted cancer imaging and highly effective photothermal therapy. ACS Appl Mater Interfaces 6:6709–6716. https://doi.org/10.1021/am5004393

136. Zhou CN (1989) Mechanisms of tumor necrosis induced by photodynamic therapy. J Photochem Photobiol B 3:299–318.

https://doi.org/http://dx.doi.org/10.1016/1011-1344(89)80035-1

137. Fickweiler S, Szeimies RM, Bäumler W, *et al.* (1997) Indocyanine green: Intracellular uptake and phototherapeutic effects in vitro. J Photochem Photobiol B Biol 38:178–183. https://doi.org/10.1016/S1011-1344(96)07453-2

138. Abels C, Fickweiler S, Weiderer P, *et al.* (2000) Indocyanine green (ICG) and laser irradiation induce photooxidation. Arch Dermatol Res 292:404–411

139. Tseng W, Saxton RE, Deganutti A, Liu CD (2003) Infrared laser activation of indocyanine green inhibits growth in human pancreatic cancer. Pancreas 27:42–45. https://doi.org/10.1097/00006676-200310000-00018

140. Bozkulak O, Yamaci RF, Tabakoglu O, Gulsoy M (2009) Photo-toxic effects of 809-nm diode laser and indocyanine green on MDA-MB231 breast cancer cells. Photodiagnosis Photodyn Ther 6:117–121. https://doi.org/10.1016/j.pdpdt.2009.07.001

141. Nagahara A, Mitani A, Fukuda M, *et al.* (2013) Antimicrobial photodynamic therapy using a diode laser with a potential new photosensitizer, indocyanine green-loaded nanospheres, may be effective for the clearance of Porphyromonas gingivalis. J Periodontal Res 48:591–599. https://doi.org/10.1111/jre.12042

142. El-Daly SM, Gamal-Eldeen AM, Abo-Zeid MAM, *et al.* (2013) Photodynamic therapeutic activity of indocyanine green entrapped in polymeric nanoparticles. Photodiagnosis Photodyn Ther 10:173–185. https://doi.org/10.1016/j.pdpdt.2012.08.003

143. Tsujimoto H, Morimoto Y, Takahata R, *et al.* (2014) Photodynamic therapy using nanoparticle loaded with indocyanine green for experimental peritoneal dissemination of gastric cancer. Cancer Sci 105:1626–1630. https://doi.org/10.1111/cas.12553

144. Li Y, Wen T, Zhao R, *et al.* (2014) Localized electric field of

plasmonic nanoplatform enhanced photodynamic tumor therapy. ACS Nano 8:11529–11542. https://doi.org/10.1021/nn5047647

145. Shemesh CS, Hardy CW, Yu DS, *et al.* (2014) Indocyanine green loaded liposome nanocarriers for photodynamic therapy using human triple negative breast cancer cells. Photodiagnosis Photodyn Ther 11:193–203. https://doi.org/10.1016/j.pdpdt.2014.02.001

146. Nomikou N, Curtis K, McEwan C, *et al.* (2017) A versatile, stimulus-responsive nanoparticle-based platform for use in both sonodynamic and photodynamic cancer therapy. Acta Biomater 49:414–421. https://doi.org/10.1016/j.actbio.2016.11.031

147. Barth BM, Altinoğlu EI, Shanmugavelandy SS, *et al.* (2011) Targeted indocyanine-green-loaded calcium phosphosilicate nanoparticles for in vivo photodynamic therapy of leukemia. ACS Nano 5:5325–5337. https://doi.org/10.1021/nn2005766

148. Gluth MB, Kaufmann YC, Dornhoffer JL, Ferguson S (2014) Immunotargeted photodynamic therapy for cholesteatoma: in vitro results with anti-EGFR-coated indocyanine green nanocapsules. Otol Neurotol 36:76–81. https://doi.org/10.1097/MAO.0000000000000590

149. Yaseen MA, Diagaradjane P, Pikkula BM, *et al.* (2005) Photothermal and photochemical effects of laser light absorption by indocyanine green (ICG). Opt Interact with Tissue Cells XVI 5695:27. https://doi.org/10.1117/12.589702

150. Miao W, Kim H, Gujrati V, *et al.* (2016) Photo-decomposable organic nanoparticles for combined tumor optical imaging and multiple phototherapies. Theranostics 6:2367–2379. https://doi.org/10.7150/thno.15829

151. Yan F, Wu H, Liu H, *et al.* (2016) Molecular imaging-guided photothermal/photodynamic therapy against tumor by iRGD-modified indocyanine green nanoparticles. J Control Release 224:217–228. https://doi.org/10.1016/j.jconrel.2015.12.050

152. Wang XH, Peng HS, Yang W, *et al.* (2017) Indocyanine green-platinum porphyrins integrated conjugated polymer hybrid nanoparticles for near-infrared-triggered photothermal and two-photon photodynamic therapy. J Mater Chem B 5:1856–1862. https://doi.org/10.1039/C6TB03215J

153. McCorquodale EM, Colyer CL (2001) Indocyanine green as a noncovalent, pseudofluorogenic label for protein determination by capillary electrophoresis. Electrophoresis 22:2403–2408. https://doi.org/10.1002/1522-2683(200107)22:12<2403::AID-ELPS2403>3.0.CO;2-B

Chapter 2

Materials, Methodology, and Instrumentations

2.1 Introduction

This chapter gives information about the materials and methods used for the successful completion of this thesis. This chapter also provides a detailed account of all the characterization techniques used to carry out the experiments presented in this thesis. Additionally, the detailed information about the cell culture methods such as viability assay and cellular uptake study have been described here.

2.2 Materials

ICG was purchased from Sigma-Aldrich Inc., Burlington, Massachusetts. The stock solution of ICG (645 μM) was prepared by dissolving the powder in deionized (DI) water (Millipore 18.2 MΩ, Sartorius system) and was stored at –80ºC to minimize the thermal degradation. All experiments were performed at room temperature, and freshly prepared ICG solutions were used for all the experiments. Poly-l-lysine (PLL, Molecular weight (M_w) = 120 kDa, ~574 lysine unit, one HBr per lysine residual) was procured from Polysciences (Warrington, Pennsylvania, U.S.). Trisodium citrate dihydrate and ethylenediaminetetraacetic acid (EDTA) were purchased from Merck (Darmstadt, Germany). Poly-l-arginine (PLA, M_w = 70 kDa, ~365 arginine unit, one HCl per arginine residual), sodium phosphate dibasic heptahydrate, and fluoromount mounting media were procured from Sigma-Aldrich (St. Louis, Missouri, U.S.) and were used as received. The stock solutions of the chemicals were prepared in DI water and

stored at 4ºC. The human cervical cancer cell (HeLa) line was procured from the National Centre for Cell Science (NCCS) Pune, India. Dulbecco's Modified Eagle Medium (DMEM), Fetal Bovine Serum (FBS), Coverslips, penicillin-streptomycin, 0.25% trypsin-1mM EDTA and 2.5% trypsin without phenol red were procured from Gibco, Thermo Fisher Scientific. 3-(4, 5-dimethylthiazol-2-yl)-2, 5-diphenyltetrazolium bromide (MTT), and 2-(4-amidinophenyl) indole-6-carboamidine-dihydrochloride (DAPI) were procured from Himedia (India) and Tokyo chemical industry (TCI) respectively.

2.3 Methodology and Instrumentation

2.3.1 Absorption Spectroscopy

When light interacts with matter, it may undergo various processes such as absorption, reflection, scattering, transmission, and emission (fluorescence/phosphorescence), as shown in **Figure 2.1(a).** The light absorbed by the molecule could be used to excite an electron from the ground (S_0) state to the respective excited singlet states such as S_1,

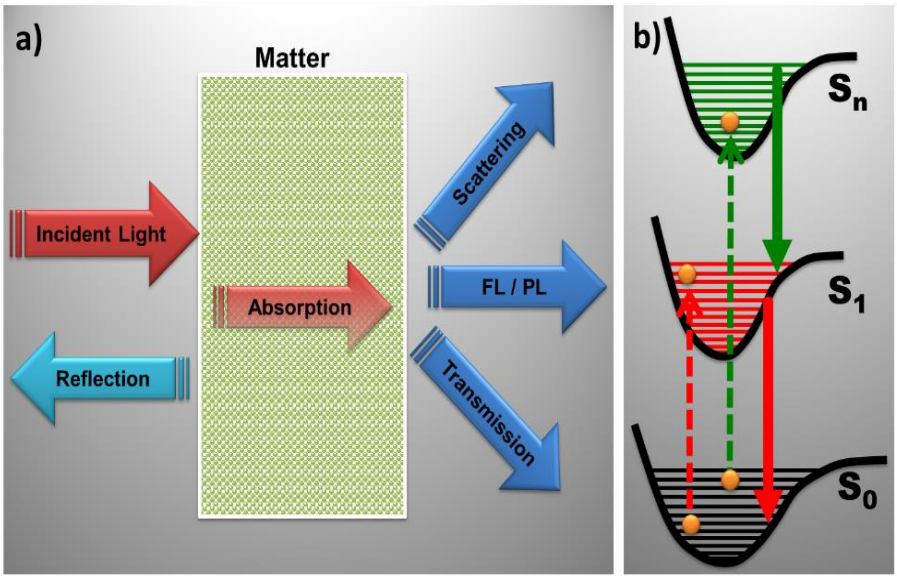

Figure 2.1 Interaction of light with matter (a) processes involve after the incident of light on matter (b) transition of electrons from respective states. The abbreviation are as follows: FL is fluorescence, PL is photoluminescence, S_0 is ground state, S_1, and S_n is first and n^{th} excited singlet state respectively.

S_2…. S_n, as shown in **Figure 2.1(b)**. The transfer of electrons from a lower energy level to a higher energy level or from higher energy levels back down to a lower energy level is known as transitions. The energy of the photons absorbed by the molecule for single-photon phenomena must be greater than or equal to the difference in energy between two energy levels for a transition to occur. As such, the electron will quickly fall back to the lower energy level, and when it does so, it emits a photon with less than the difference in energy levels called fluorescence emission.

In this work, the absorption of the molecules was measured by spectrophotometer. In principle, when the light is irradiated on a sample, it passes through or gets reflected. Therefore, the amount of light absorbed by the sample is calculated by the incident radiation (I_o) and the transmitted radiation (I_T), as shown in **Figure 2.2**. Quantitatively, absorbance is described by an equation known as Beer-Lambert law, as given below in **Equation 2.1.**[1]

$$A = -\log (T) = -\log (I_T/I_o) = \varepsilon cl \text{……} \textbf{Equation. 2.1}$$

In the above equation, A is absorbance or optical density (a unitless quantity), T is transmittance, I_o, and I_T are the intensity of incident and

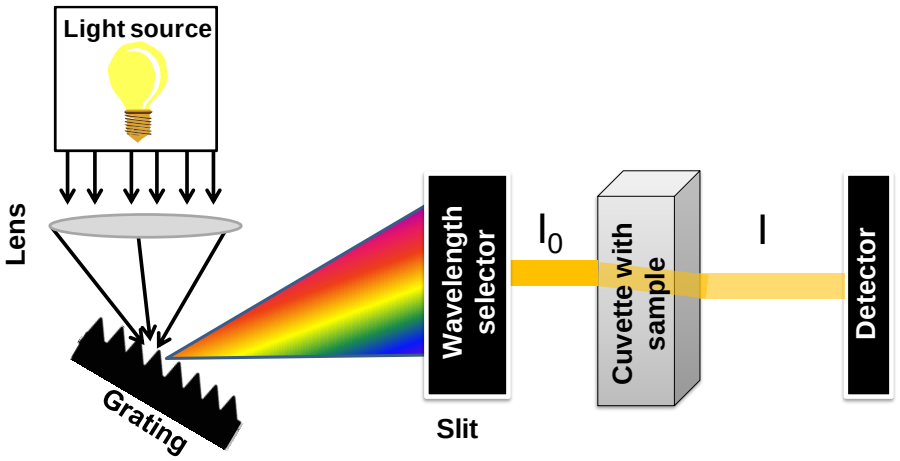

Figure 2.2 The ray diagram and working principle of the UV-Vis-NIR absorption spectroscopy. The abbreviation are as follows: I_0 is incident light, and I is the transmitted light.

transmitted light respectively for a given wavelength. However, ε is the molar extinction coefficient (a constant unique to each compound, given in units of $M^{-1}cm^{-1}$), c is a molar concentration of the sample (M, or mol/L), and l is the path length of the sample cell (in cm). In general, a UV-Vis-NIR spectrometer comprises of a light source (to generate the broad wavelength light) and a lens to focus that light on the grating, which breaks the white light into the light of different wavelengths. Further, the wavelength selector (slit) selects the individual wavelength of light, which is radiated on the sample. The absorbed wavelengths by the sample are recorded by photomultiplier tubes detector (PMT), which converts the light into an electrical signal. All absorption spectra shown in this thesis have been measured using a Perkin Elmer (Lambda 35) UV-Vis-NIR spectrometer. For measurements, a quartz cuvette of (10 mm × 10 mm) or (10 mm × 2 mm) has been used. The absorption data were collected with a 1 nm slit width and 480 nm/min scan rate. Al the data has been plotted and analyzed with the Origin software.

2.3.2 Fluorescence Spectroscopy

Generally, the electrons that are excited to higher energy states after the absorption of light are not stable and come back to the S_0 state by the radiative or non-radiative process. Fluorescence is a process of emission of radiation, where the transition of the molecule occurs from a higher singlet electronic (S_n) state to S_0 state. In general, the fluorescence emission always has a redshift with respect to the absorption wavelength due to loss of energy, and this wavelength shift is called the Stokes shift. The fluorescence and phosphorescence processes have been shown in **Figure 2.3** using a Jablonski diagram, where the transition of electrons from the higher singlet state S_1 to S_0 state is fluorescence emission, and transition from higher triplet state to S_0 state is called phosphorescence.[2] The lifetime of the absorption process is in the order of femtoseconds, the lifetime of fluorescence varies from picosecond to nanoseconds, and the lifetime of

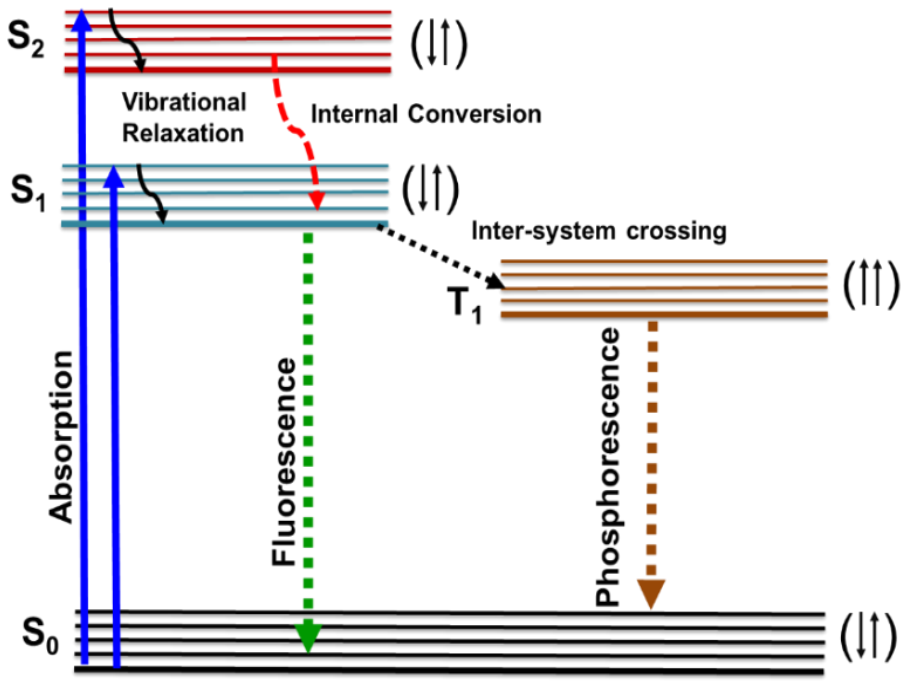

Figure 2.3 Jablonski diagram is showing all possible transitions. The abbreviation are as follows: S_0 is ground state, S_1 and S_2 is first and second excited singlet state and T_1 is first excited triplet state.

phosphorescence is from microsecond to hours.[3] The fluorescence process always follows the Kasha's rule, which suggests that fluorescence always occurs when an electron from the lowest vibrational level of the first excited singlet state relaxes back to the S_0 state.[4] However, the fluorescence emission depends upon the molecule and its chemical environment. Fluorescence gives information about the electronic states and the molecule's relaxation dynamics.

All the steady-state fluorescence measurements were taken using a research-grade fluorometer (HORIBA, Jobin Yvon, model FL3-12). A 400-Watt Xenon lamp was used as an excitation source for all the fluorescence measurements. These measurements were carried out in a right-angle geometry with an excitation/emission slit width of 5 nm, and the samples were kept in a four sides clear quartz cuvette (10 mm X 2 mm or 10 mm X 10 mm). The spectra were collected using inbuilt software of spectrofluorimeter, i.e., FluorEssence

software, which merges fluorometer data-acquisition directly to the origin 8.0 software for further data analysis.

2.3.3 Circular Dichroism (CD) Spectroscopy

Circular dichroism (CD) spectroscopy is a technique, which measures the difference in the absorption between left and right-handed circularly polarized light of the chiral molecules. It is a well-known biophysical method to study the secondary structure (e.g., helices, beta-sheets, turns, etc.) of nucleic acids, and peptides, which have distinct CD bands in far-UV and UV-Vis range. In this method, the instrument has a light source that was converted to monochromatic light using monochromator and slit, which is further irradiated on a photoelastic modulator (PEM). PEM converts horizontally polarized light to circularly polarized light. Also, the optically active sample was irradiated by this signal, and the detector detected the CD signal, as shown in **Figure 2.4.**

Here, CD spectroscopy has been used to study the

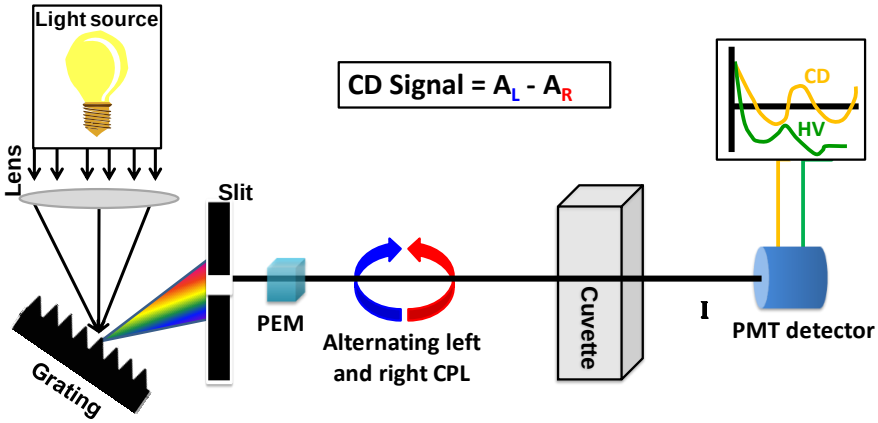

Figure 2.4 The ray diagram and the working principle of the CD spectroscopy. The abbreviation are as follows: PEM is a photoelastic modulator, and PMT is a photomultiplier tube, the CD is circular dichroism, I is Incident intensity, A_L and A_R is the absorption of left and right-handed circularly polarized light, and HV is high voltage.

conformational changes of homopeptide, and perturbation occurred on its confirmation after interaction with ICG. Every peptide molecule gives a signature CD spectrum, which reflects its conformation. Generally, all possible conformations of the peptide structures such as parallel, antiparallel, mixed, and random could be determined from the position and magnitude of the CD spectra bands. CD spectroscopy was used to study interactions between homopeptide, salts, and drug/contrast agents during self-assembly. Generally, small molecules do not exhibit a CD signal in solution. All the homopeptides used in this thesis are titrated with a non-chiral molecule. It must be pointed here that the changes observed in the UV region could be directly related to the interaction of the homopeptide with the small molecule.

All CD spectra measurements were done on a spectropolarimeter (JASCO, model J-815, Tokyo, Japan) equipped with a Peltier junction temperature controller. Far-UV spectra of solutions were recorded between 180 to 250 nm with 0.1 nm intervals, 1 nm slit width, 20 nm/min scanning speed, and a response time of 1 second. A quartz cuvette (Hellma GmbH & Co., Müllheim, Germany) with a 2 mm path length was used for the CD measurements. Samples were prepared by diluting the homopeptide in DI water to get final concentration as stated in CD spectra. Every spectrum was obtained by averaging three scans and was corrected by subtracting the blank spectrum of the solvent (DI water). The temperature of the measurements was maintained at 25 ºC using a Peltier temperature controller.

2.3.4 Time-Correlated Single Photon Counting (TCSPC)

TCSPC has been widely used for time-resolved spectroscopy, it tells about the fluorescence lifetime of chromophores in solutions. In this method, the fluorophore is excited by the pulsed laser, and the fluorescence intensity is monitored as a function of time. In simple words, the fluorescence lifetime of a molecule is the average time electrons spend in the excited state. The lifetime of the molecule

depends on the molecular structure and its local environment.[5] Generally, the excited state decays in an exponential manner, as mentioned below in **Equation 2.2.**

$$I(t) = I_o \exp(-t/\tau) \ldots\ldots\ldots\ldots\ldots\ldots \textbf{Equation 2.2}$$

Where I_o is the incident light intensity, I(t) is the intensity of light at a given time t and τ is the fluorescence lifetime or the time for the intensity decay to 1/e of its initial value. The fluorescence lifetime

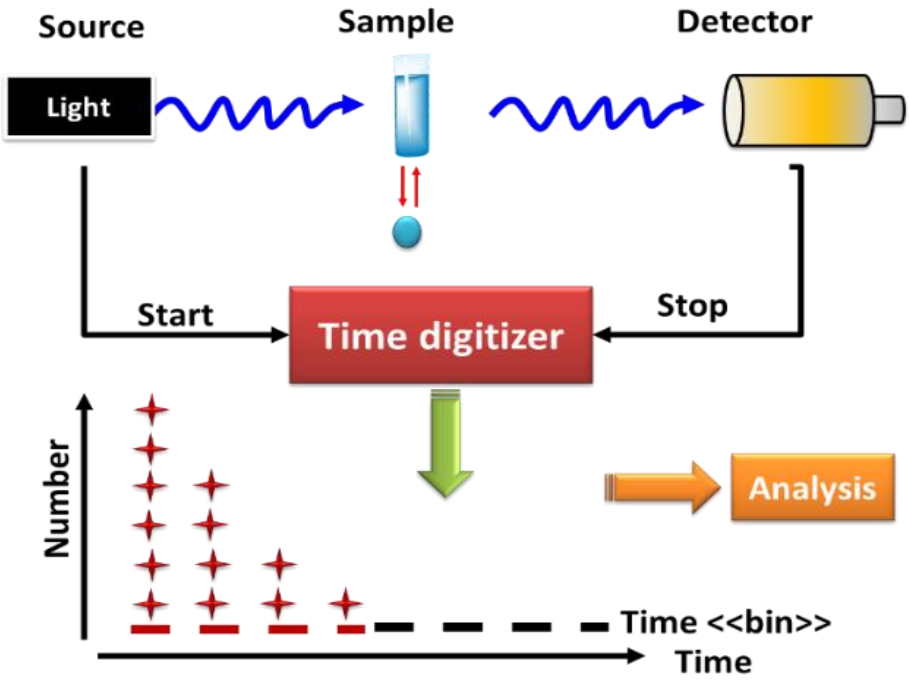

Figure 2.5 Schematic diagram of TCSPC system depicting the fluorescence lifetime measurement principle.

measurement has an advantage over steady-state fluorescence intensity measurement, as it is an "absolute" measurement, rather than "relative" steady-state measurement. It provides information about the dynamic processes occurring on a time scale as short as picoseconds. It detects a single photon of a pulsed laser signal and constructs the decay curves from each time measurement of an individual photon. In this technique, a pulsed excitation source (light-emitting diode (LED) or laser diode) is used for measurement. A pulse of light produces a

"start" timing signal, which gives input into timing electronics (digitizer as shown in **Figure 2.5**). The light excites the sample, which gives emission due to the relaxation process of the fluorophores. This emission pulse is incident on the detector, which then provides a "stop" signal to the timing electronics. The difference between these two signals is plotted with the help of a histogram. This process is repeated several times, which builds up the histogram, with the number of counts in histogram "time bin" is proportional to the intensity of the decay at that time, as long as single-photon timing conditions are observed.[6]

In this thesis, all TCSPC measurements were performed on a nanosecond TCSPC system (Horiba, Jobin Yvon, model: Fluorocube-01-NL). For our studies, a 2 mL solution of the samples was prepared in a quartz cuvette (1 cm X 1 cm), and the samples were excited at different excitation wavelengths (279 nm and 405 nm for the whole work) by picosecond or nanosecond diode laser (model DD-280 and DD-405L). The decays were collected with the emission polarizer at a magic angle of 54.7° by a photomultiplier tube (TBX-07C) with a dark count of less than 20 cps. The instrument response functions (IRF, FWHM~140 ps) were recorded using a ludox solution. The fluorescence decays were analyzed using IBH DAS (version 6.0, HORIBA Scientific, Edison, NJ) decay analysis software by the iterative reconvolution method, and the goodness of the fit was judged by reduced χ^2 value.

2.3.5 Photoluminescence (PL) Spectroscopy

Emission characteristics from the samples, a qualitative analysis was done using photoluminescence (PL) spectroscopy. Photoluminescence measurements were done using a PL spectrometer (DongWoo Optron, DM 500i, Japan), affixed with a 20 mW continuous wave He-Cd laser (excitation wavelength of 325 nm, TEM00 mode) 320 mm and 150 mm focal length monochromators, chopper, a lock-in amplifier, and a PMT detector, were deployed to conduct optical studies. All

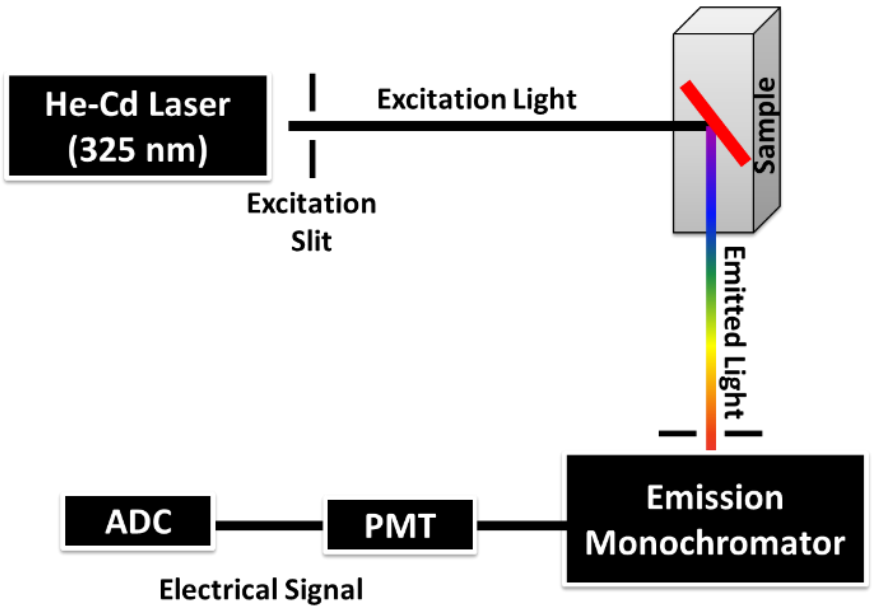

Figure 2.6 Schematic diagram of the PL measurement system. The abbreviation are as follows: ADC is analog-to-digital converter and PMT is a photomultiplier tube.

measurements were performed at room temperature. The schematic of the PL measurement system is shown in **Figure 2.6**. The output of a laser light source (325 nm) is passed through the excitation slit, and the sample is placed in the path of the monochromatic light with an angle of 90°. When the sample is optically excited, it emits light in all directions at various wavelengths, depending on molecular structure. A small portion of the emitted light passes through the emission slit and filtered by the monochromator. Typically, the remaining optical signal has a very low intensity; hence, a PMT detector is used to measure low-intensity optical signals. To get the spectral distribution of the emitted light, the emission monochromator scans the desired wavelength spectrum, and the light intensity measured by the detector is recorded.

2.3.6 Dynamic Light Scattering (DLS) Spectroscopy

Particles suspended in liquids are in Brownian motion due to random collisions of the molecules with the solvent molecules. This Brownian motion causes the particles to diffuse through the medium. The

diffusion coefficient, D, is inversely proportional to the particle size according to the Stokes-Einstein equation (**Equation 2.3**).[7]

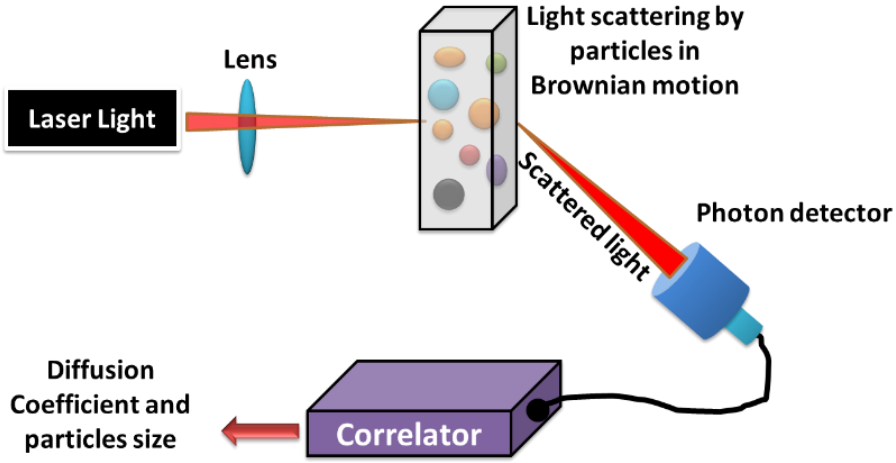

Figure 2.7 The basic working principle of DLS for obtaining diffusion coefficient and particle size information.

$$D = k_B T / 3\pi\eta_o d \ldots\ldots\ldots\ldots\ldots\ldots \textbf{Equation 2.3}$$

Where D is a diffusion coefficient, k_B is Boltzmann's constant, T is temperature, η_0 is the viscosity, and d is the hydrodynamic diameter. This equation shows that, for large particles, D will be relatively small, and thus, the large particles will move slowly. While for the smaller particles, D will be larger, so the particles will move faster. Therefore by observing the motion and determining the diffusion coefficient of particles in liquid media, it is possible to determine their size.[8]

In DLS, the time-dependent intensity fluctuations of the scattered light are collected by the detector. This data is used to calculate the autocorrelation function, which is finally used to calculate the size of the particles. **Figure 2.7** shows the schematic of the dynamic light scattering setup. When laser light is focused onto the sample in the cuvette, the sample in the focused volume scatters the light in all directions. This volume is defined by the scattering angle and detection apertures. However, the observed intensity of the scattered light at any instant will be a result of the interference of scattered light by the particles, and this will depend on the relative positions of the particles.

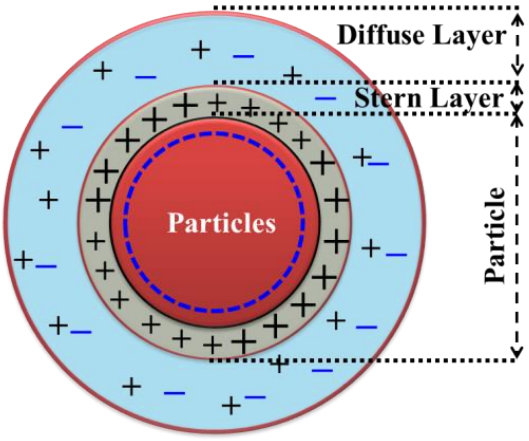

Figure 2.8 Schematic diagram of an electrical double layer.

If the particles are in motion in solution, the relative positions of the particles will change with time, and thus fluctuations in the scattered light intensity will be observed. Since particles are in Brownian motion and move randomly, the scattered light intensity fluctuations are random. The fluctuations will occur rapidly for smaller, faster-moving particles and slowly for larger, slow-moving particles. The light intensity data is acquired over a period of time and is controlled by the digital correlator. The raw data is used to calculate the autocorrelation function; this information is further used to calculate the mean diameter or the size distribution of the particles. This method provides the hydrodynamic diameter of the particles. Further, the measurement of the zeta (ζ) potential was also done using DLS. Particles dispersed in a liquid have a net positive or negative charge. In liquid, the ions that have an opposite charge to the particle surface, get adsorbed on the surface of the particle to keep it electrically neutral. This phenomenon is known as the formation of an electrical double layer and is shown in **Figure 2.8.** The concentration of the counterions is high near the particle surface and gradually decreases with increasing distance from the surface. Equal numbers of positive and negative ions exist in the area far from the particle surface so that electrical neutrality is maintained. This ion distribution is called a diffuse electrical double layer. The diffuse electrical double layer can be divided into two layers: the layer of ions near the particle surface, which is called the

Stern layer. The ions in the Stern layer are strongly attracted to the surface of the particle. The layer outside the Stern layer is called the diffuse layer. In this layer, the ions are diffused. The stability of the dispersing particles is influenced by their surface charge. Zeta potential is used as the index of the surface charge of the particles. It is assumed that the particles are undergoing Brownian motion in a liquid and move not only with the ions in the Stern layer where the ions are attracted strongly near the particle surface but also with a part of the diffuse layer. The electric field from which this movement takes place is called the (slipping plane). Zeta potential is considered to be the potential at the slipping plane, and the potential at the position far from the particle surface is defined as zero. If ζ potential is high, the particles are monodisperse/ not aggregate due to high electrostatic repulsion between particles. On the contrary, a low ζ value (approaching zero) increases the probability of particles colliding and thus forming particle aggregates. Therefore, ζ is used as an index of the dispersion stability of the particles. In this thesis, all ζ measurements were done with a NanoPlus-3 zeta/nanoparticle analyzer (Micromeritics Instrument).

2.3.7 Fluorescence Microscopy Study

The basic principle of fluorescence microscopy is the same as fluorescence spectroscopy. In this thesis, all fluorescence microscopic measurements were performed using an inverted microscope (Nikon, model Eclipse Ti–U). The mercury, Xenon, and halogen lamps were used as the sources for the illumination. The filters cubes used for the selection of the excitations and emission wavelength. The DAPI filter covers an excitation wavelength ranges between 349 - 380 nm, whereas the collection was done by bandpass filters, which allow 435 - 485 nm. Likewise, the Fluorescein isothiocyanate (FITC) covers an excitation wavelength range between 465 - 495 nm with an emission collection window between 515 – 555 nm. Tetramethyl rhodamine (TRITC) filter allows excitation range between 540 ± 12.5 nm with

band allow filter for collection window between 605 ± 55 nm. Most importantly, the NIR excitation filter allows 775 ± 25 nm, whereas the collection window allows 845 ± 27.5 nm. The images were analyzed with ImageJ software (Version 1.46r, National Institutes of Health (NIH)).

2.3.8 Field-Emission Scanning Electron Microscopic (FESEM)

FESEM has been used in this thesis to visualize the morphological structure of the fabricated nanoparticles. In SEM, a beam of accelerated electrons as a source of illumination is used for the imaging. It gives higher resolving power than light microscopy and can reveal the structure of nanometer size particles. In SEM, the electron beam interacts with the sample and loses its energy by various processes.[9] The energy loss is converted into alternative forms such as heat, emission of low-energy secondary electrons (< 50 eV, from which the SEM images are obtained), Auger electrons (surface contamination analysis, top 50 Å), and high-energy backscattered electrons (which are used to determine crystal structures and

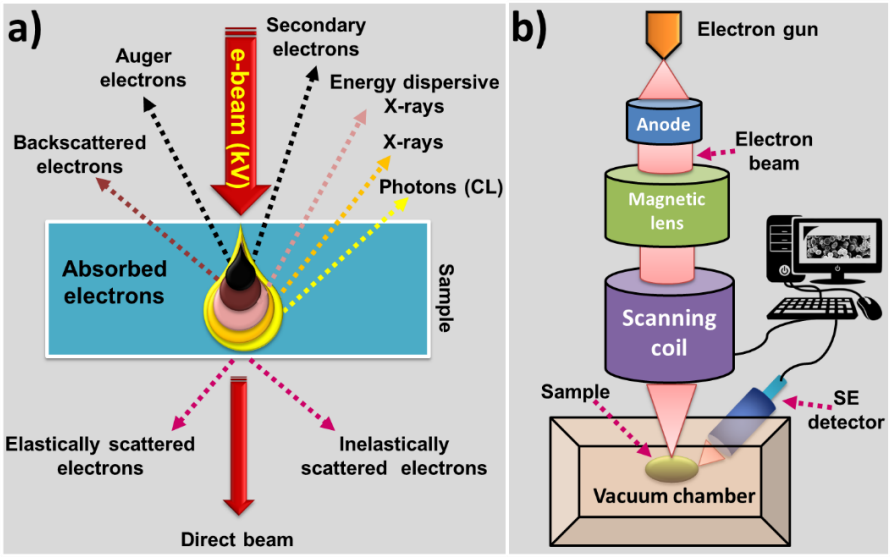

Figure 2.9 Working principle of the FESEM (a) Interaction of electron beam with the sample (b) Schematic representation of the FESEM instrumentation. The abbreviation are as follows: CL is cathodoluminescence, and SE is secondary electrons.

orientations of minerals), light emission (cathodoluminescence (CL)) and X-rays (used for elemental analysis) as shown in **Figure 2.9(a)**. Backscattered electrons and secondary electrons emitted from the sample are commonly used for the imaging application in SEM. Secondary electrons are most important for producing morphology and topography of samples (acquire from inelastic scattering electrons close to the surface), while backscattered electrons (acquire from elastically scattered electrons, higher energy) are most essential for illustrating contrasts in the composition of multiphase samples. In a typical SEM, as shown in **Figure 2.9**, an electron beam is thermionically emitted from an electron gun coupled with a tungsten filament cathode. Tungsten is generally used because it has the highest melting point and lowest vapor pressure of all metals, thereby making it suitable for electron emission. The anode, which is positive with respect to the filament, forms powerful, attractive forces for electrons. This causes electrons to accelerate toward the anode. The anode is arranged as an orifice through which electrons would pass down to the column where the sample is held. In the electron microscope, the electron beam with energy typically between 1-10 keV is focused by a lens system into a spot of 1-10 nm diameter on the sample surface. The focused electron beam is rastered across the surface of the sample through the condenser lens to a spot size of about 0.4 nm to 5 nm diameter. The emitted/scattered electrons after the electron-sample interactions are collected by a detector and converted to voltage, and finally, the SEM image is formed from a two-dimensional density distribution of detected electrons. A variety of signals can be detected, including secondary electrons, backscattered electrons, X-rays, CL, and sample current. This technique is useful for producing relatively quick qualitative impressions of the sample surface. The samples must be viewed in a vacuum, as the molecules in the air would scatter the electrons. SEM is operating in conventional high vacuum mode and usually imaging conductive samples; therefore, non-conductive materials require conductive coating (gold/palladium alloy, carbon, and osmium, etc.). However, in FESEM, the FE gun is used to produce

an electron beam that is smaller in diameter, more coherent, and up to three orders of magnitude greater current density or brightness. In this thesis, all FESEM measurements were performed using a Carl Zeiss Microscope (model-Supra 55) equipped with energy-dispersive X-ray spectroscopy (EDS, Oxford Instruments, X-MAX, 51-XMX1025). The secondary electron images (SEI) were taken between 2-10 kV electron beam with a working distance of ~10 mm. For FESEM measurements, the nanoparticle pellet was dried in a lyophilizer (Alpha 1-2 LD plus, Labmate). Following lyophilization, the dried samples were placed on a double-sided sticky carbon tape mounted on an aluminum stub. Before visualization in SEM, the samples were sputter-coated with gold by direct current (DC) sputter coater (Quorem (Q-150RES)) for better electron conductivity. The subsequent SEM images were analyzed using IMAGE J software (NIH, Bethesda, MD, U. S.).

2.3.9 Multiphoton Microscopy

Confocal microscopy, which uses lasers for excitation of the samples, offers several advantages over conventional optical microscopy, including the elimination of out-of-focus glare and the ability to collect serial optical sections from thick specimens.[10] In the biomedical sciences, a major application of confocal microscopy involves imaging of labeled samples with one or more fluorescent probes. This technique could be used for live cells, fixed cells, and tissue samples. The multiphoton experiments were performed on a laser scanning multiphoton confocal system (Olympus, model no. FV1200MPE, IX-83, Japan). The multiphoton confocal imaging system is equipped with the femtosecond negative chirped infra-red laser. **Figure 2.10** shows the schematic of the multiphoton imaging system used in this thesis. A mode-locked Ti-Sapphire laser (MaiTai, Deep-See, Spectra-Physics) was used as an excitation light source, which provides a pulse with the pulse width ~ 70 fs at 80 MHz repetition rate with the wavelength ranging from 690 nm to 1064 nm. The wavelength selection was made with the help of an acousto-optic modulator.

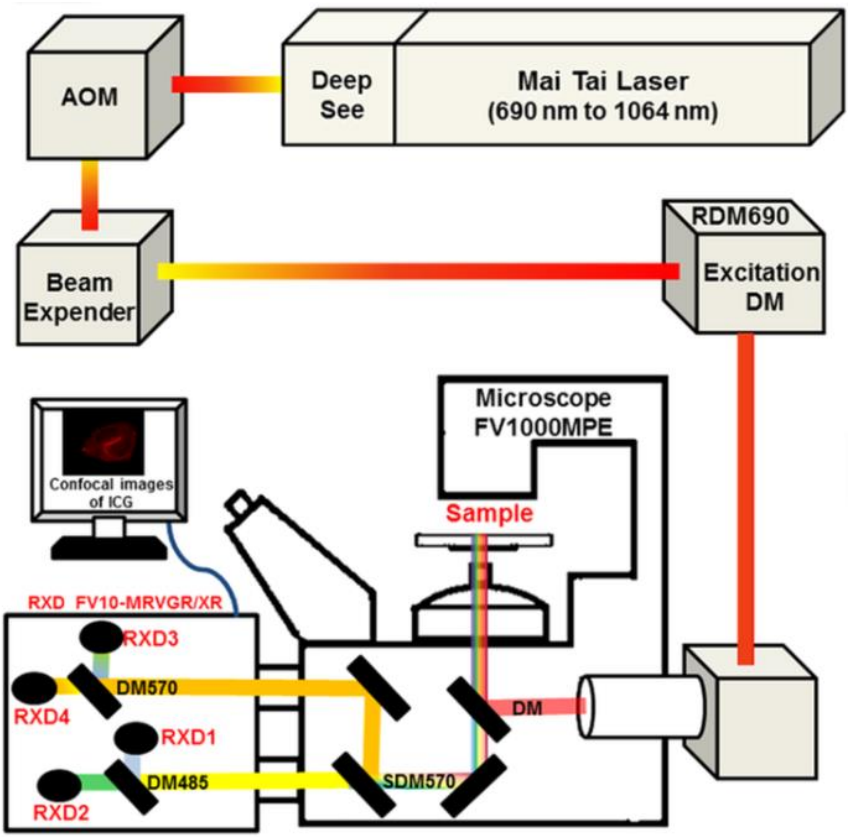

Figure 2.10 Schematic setup of multiphoton Olympus confocal laser scanning microscope equipped with MaiTai laser for multiphoton imaging. The abbreviation are as follows: AOM is acoustic optical modulator, DM is dichroic mirror, RXD1 is BA 420 – 460 nm, RXD2 is BA 495 – 540 nm, RXD3 is BA 380 – 560 nm, and RXD4 is BA 575 – 630 nm.

Docking Studies and Molecular Modeling Simulation

Molecular docking is a useful tool not only for the development and designing of new drugs but also for predicting the interaction between the small molecule and homopeptide. We have used AutoDock 4.2 (graphical user interface) in our study, in which docking is done by pre-calculating energy grids created around the site of interest.[11] ChemDraw Ultra 12 and Chem3D Pro 12 were used to generate the 3D structure of homopeptide and ICG. The energy was minimized using density functional theory.[12] For docking, the preparation of the target macromolecule was done with AutoDock Tools, which involves

the addition of polar hydrogen atoms, and partial charge correction to the target molecule. In the final step, Gasteiger charges were calculated for each atom of the macromolecule. A grid of 40 Å x 40 Å x 40 Å with a grid spacing of 1 Å was positioned around the macromolecule. Docking calculations consist of 25 million energy evaluations (ga_num_evals) using the Lamarckian Genetic Algorithm Local Search (GALS) method. All other parameters were set to defaults, the maximum number of generation (ga_num_generation) was 27,000, and the maximum number of iterations per local search was set to 100. The 6 and 7 Docking results were clustered based on the free energy of binding and hydrogen bond interactions. Finally, the University of California, San Francisco (UCSF)-Chimera, visualization software was used to visualize and analyses the integration of the PLL and ICG.[13]

2.3.10 Cell Culture

The HeLa cells were cultured and maintained at 37 ºC with 5% CO_2 in Dulbecco`s Modified Eagle Media culture medium containing 10% heat-inactivated fetal bovine serum, 1% penicillin, and streptomycin. Cultures at approximately 80% confluence were routinely split in the ratio of 1:3 in 60 mm cell culture dish as follows. Initially, cells were washed in phosphate buffer saline (PBS). One milliliter (1 mL) of PBS containing 0.25% (w/v) of trypsin was added to the 60 mm dish and placed at 37 ºC for 5 min for cell detachment. After the cells were detached from the dishes, 1 mL of pre-warmed culture medium was added, and the cells were transferred to a 15 mL falcon tube. Cells were spun down at 1200 rpm for 2 minutes and plated in a new 60 mm dish with fresh culture medium for imaging experiment. HeLa cells (10^5 cells/mL) were grown on 18 × 18 mm square glass coverslips in six-well plates. For labeling, HeLa cells were incubated with ICG at 37 ºC for 4 hours. Following the incubation, HeLa cells were washed thrice with PBS and fixed for 10 minutes at room temperature with 4% paraformaldehyde and further washed with PBS. Coverslips were

subsequently washed in PBS and mounted on glass slides using fluoromount aqueous mounting media.

2.3.11 Cells Viability Assay

Cell-based colorimetry assays are used in this thesis for the determination of the cytotoxic effects of the nanoparticles. MTT assay, i.e., 3-(4,5-dimethylthiazol-2-yl)-2,5-tetrazolium bromide, is one of the quantitative colorimetric assays used for determination of mammalian cell survival and proliferation.[14] This assay is based on the principle of reduction of MTT from a pale-yellow tetrazolium salt to a dark purple formazan product by mitochondrial succinate dehydrogenase when incubated with metabolically active cells that are live cells as shown in **Figure 2.11**. The principle of MTT assay is the quantification of the mitochondrial activity of the cells. Mitochondrial activity for all the viable cells is almost constant.[15] Therefore, an increase or decrease in the number of viable cells linearly relates to the mitochondrial activity of the cells. The mitochondrial activity of cells is equivalent to the conversion of the MTT salt into the formazan crystals, which can be solubilized for homogenous measurement. MTT enters the cells and reaches to mitochondria, where it is reduced to an

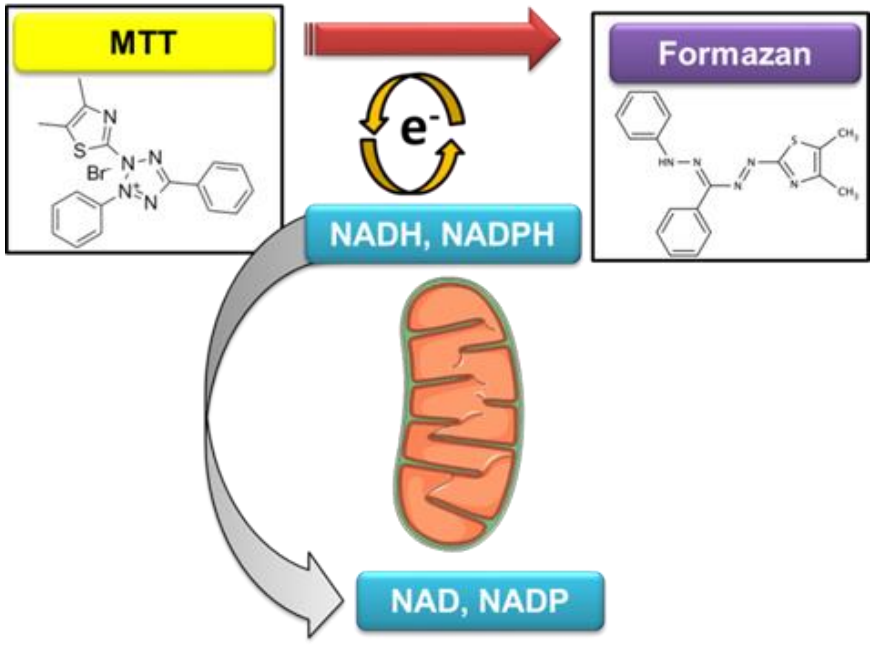

Figure 2.11 Schematic representations of the MTT assay principle.

insoluble, dark purple formazan product. These formazans were solubilized with an organic solvent (e.g., isopropanol or dimethyl sulfoxide); thus, any increase or decrease in viable cell number can be detected by measuring formazan concentration using a microplate reader. In our study, we have performed MTT assay to determine the cytotoxicity of fabricated NPs using HeLa cells, a cancer cell line. For performing MTT assay, 10×10^3 cells/well were seeded in a 96-well flat-bottomed microplate (Eppendorf) and allowed to grow in the complete growth medium. Serial dilutions of compounds were added to each well with the solvent as a control. The microplate was incubated in a humidified incubator at 37 °C with 5% CO_2 supply, for 4 or 24 h. After incubation, 10 µL of MTT (5 mg/mL in PBS) was added to each well and further incubated for an additional 4 h at 37 °C to allow intracellular reduction of the soluble yellow MTT to insoluble purple formazan crystals.

Cellular Viability (%) =

$$\left\{\frac{Abs.\ of\ NPs\ treated\ cells\ with\ MTT\ treatment - Abs.\ of\ NPs\ treated\ cells\ without\ MTT}{Abs.\ of\ control\ cells\ with\ MTT\ treatment - Abs.\ of\ control\ cells\ without\ MTT}\right\} * 100$$ ……..…...…**Equation 2.4**

Where Abs. is absorbance, these crystals were dissolved by adding 200 µL of DMSO, and the absorbance was read at 570 nm and 690 nm using a microplate reader (Synergy H1, multi-mode microplate reader). Cells viability was determined by the formula mentioned in **Equation 2.4**.

2.4 References

1. Swinehart DF (1962) The Beer-Lambert law. J Chem Educ 39:335. https://doi.org/10.1021/ed039p333

2. Frackowiak D (1988) The Jablonski diagram. J Photochem Photobiol B Biol 2:399. https://doi.org/10.1016/1011-1344(88)85060-7

3. Dobrucki JW, Kubitscheck U (2005) Fluorescence Microscopy. Nat Methods 2:910–919. https://doi.org/10.1002/9783527687732.ch3

4. Kasha M (1950) Characterization of electronic transitions in complex molecules. Discuss Faraday Soc 9:14–19. https://doi.org/10.1016/j.vaccine.2018.07.004

5. Phillips D, Drake RC, O'Connor DV, Christensen RL (1985) Time Correlated Single-Photon Counting (Tcspc) Using Laser Excitation. Instrum Sci Technol 14:267–292. https://doi.org/10.1080/10739148508543581

6. Wahl M (2014) Technical Notes: Time-correlated single photon counting. PicoQuant GmbH 1–14. https://doi.org/10.1016/0022-2313(89)90051-3

7. Miller CC (1924) The Stokes-Einstein Law for Diffusion in Solution. Proc R Soc A Math Phys Eng Sci 106:724–749. https://doi.org/10.1098/rspa.1924.0100

8. Stetefeld J, McKenna SA, Patel TR (2016) Dynamic light scattering: a practical guide and applications in biomedical sciences. Biophys Rev 8:409–427. https://doi.org/10.1007/s12551-016-0218-6

9. McMullan D (1995) Scanning electron microscopy 1928–1965. Scanning 17:175–185. https://doi.org/10.1002/sca.4950170309

10. Denk W, Strickler JH, Webb WW (1990) Two-photon laser scanning fluorescence microscopy. Science (80) 248:73–76. https://doi.org/10.1126/science.2321027

11. Morris GM, Huey R, Lindstrom W, *et al.* (2009) AutoDock4 and AutoDockTools4: Automated Docking with Selective Receptor Flexibility. J Comput Chem 30:2785–2791. https://doi.org/10.1002/jcc.21256.AutoDock4

12. Evans DA (2014) History of the Harvard ChemDraw Project. Angew Chemie Int Ed 53:11140–11145. https://doi.org/10.1002/anie.201405820

13. Pettersen EF, Goddard TD, Huang CC, *et al.* (2004) UCSF Chimera — A Visualization System for Exploratory Research and Analysis. J Comput Chem 25:1605–12. https://doi.org/10.1002/jcc.20084

14. Morgan DM (1998) Tetrazolium (MTT) assay for cellular viability and activity. Methods Mol Biol 79:179–83

15. Riss TL, Moravec RA, Niles AL, *et al.* (2004) Cell Viability Assays. Eli Lilly & Company and the National Center for Advancing Translational Sciences

Chapter 3

Fabrication of the Biodegradable and Biocompatible Essential Amino-acid Based Nanoparticles for NIR Bioimaging

3.1 Introduction

Cancer is one of the deadliest diseases worldwide.[1] An early-stage cancer diagnosis is an extremely crucial step towards successful treatment as well as for improving the patient survival rate.[1] The ability to visualize the deep-seated inhomogeneities in the biological samples is a crucial step for early-stage cancer diagnosis. Fluorescence based optical imaging permits non-invasive assessment of the tissue inhomogeneities for evaluation of the disease progression. However, the visualization of the deep-seated inhomogeneity within the tissue is challenging due to the presence of endogenous absorber, autofluorescence, tissue thickness, and light scattering by biological tissue samples. The use of exogenous contrast agents in the NIR region offers advantages for deep tissue imaging due to the least light absorption and scattering, results in a higher number of photons penetration inside the tissue.

ICG is the only U. S. FDA approved NIR fluorescent dye, which is used for various clinical applications such as liver function monitoring, cardiac output, and hepatic function measurement, *etc.*[2, 3] Despite its several clinical applications, ICG has not been used to the fullest for deep tissue imaging in its free-form. The free form of ICG suffers from off-site delivery, non-specific binding with plasma

This chapter is largely taken from ***Kumari, A.,*** *Kumari, K., and Gupta, S. "Protease Responsive Essential Amino-Acid Based Nanocarriers for Near-Infrared Imaging" Scientific Reports, 2019, 9, 20334.*

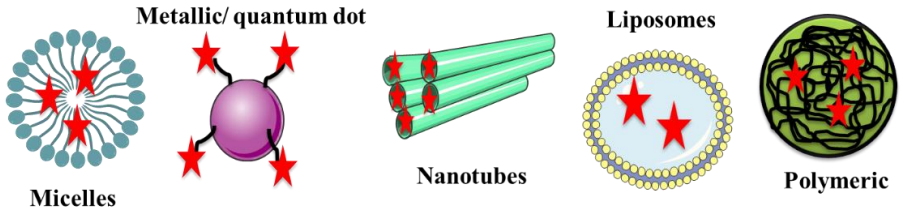

Figure 3.1 Various types of nanocarriers.

proteins, concentration-dependent aggregation, and poor optical and thermal stability.[4, 5] These limitations restrain the application of ICG to be used as an exogenous contrast agent for *in-vivo* deep-tissue bioimaging. Nanobiotechnology is an appropriate approach to address these shortcomings. Nanoencapsulation has been found to improve the molecule's half-life and the effective concentration of the therapeutic dose due to the site-specific delivery, which reduces the side-effects of the drug/contrast agents.[6–9] In recent years, various nanocarriers have been developed as drug carriers such as metal nanoparticles (NPs), polymer-based NPs and liposomes, *etc.* as shown in **Figure 3.1.**[10–16] However, the major constraint of most NPs is their poor biocompatibility, non-biodegradability, and long and short-term tissue toxicity.[17–20] As a result, considerable interests have been shown towards the fabrication of the NPs using biomacromolecules such as lipids, amino acids, and proteins for the delivery of drugs and contrast agents.[21–24] Here, in this chapter, the new formulation ICG was done utilizing essential amino-acid based homopolymers to overcome the limitations of free ICG for NIR imaging.

PLL is a homopolymer of an essential amino-acids, Lysine, which plays a vital role in the body.[25] The body utilizes it for bone development, protein synthesis, and the production of collagen by promoting absorption of calcium.[26, 27] Also, it helps in the production of various hormones, antibodies and enzymes, and tissue repair.[28] It is a cationic homopeptide, generally being used for cell adhesion in the cell culture plates from the last four decades.[29] Recently, it has gained the significant attention of the scientific

community in the domain of gene therapy and surface coating of metal particles.[30–35] The PLL composite with metals gained interest as a potential carrier for drug delivery. Wu *et al.* encapsulated theranostic molecule in triblock copolymer micelles of poly(ethylene glycol)-b-poly(L-lysine)-b-poly(L-leucine) (PEG-PLL-PLLeu), and Wang *et al.* used a composite of PLL with Pt(II)-porphyrins.[36, 37] However, these composites of the PLL are not completely biodegradable, and their fabrication process requires organic solvents, which might have toxic effects. Here, we used a simple two-step green chemistry-based method to fabricate biodegradable nanocarriers from PLL in an aqueous medium.

In the present study, we demonstrate a simple green chemistry-based new formulation of ICG within PLL forming ICG PLL NPs, which has the potential for NIR bioimaging. In comparison to other NPs, these ICG PLL NPs are completely biodegradable and biocompatible. The *in-vitro* cellular uptake study result shows that ICG PLL NPs incubated cells had significantly higher NIR fluorescence emission in comparison to the free-form of ICG. To the best of our knowledge, this is the first report on the green chemistry-based fabrication of ICG encapsulating protease responsive ICG PLL NPs for NIR bioimaging. In addition to ICG, these NPs could also be used for the encapsulation of various theranostic agents such as hydrophobic anticancer molecules and chemotherapeutic drugs, *etc*. for targeted drug delivery.

3.2 Results and Discussion

Here ICG was encapsulated within PLL via a two-step self-assembly method. It is pertinent to note that the assembly of ICG PLL NPs was accomplished in an aqueous medium by mixing of the essential amino-acid homopeptide, ICG, and multivalent anionic salts. All components used for the fabrication were nontoxic for biological samples.

3.2.1 Synthesis of ICG Loaded ICG PLL NPs

The nanoencapsulation of ICG within PLL NPs was done using a simple two-step self-assembly process. The schematic illustration of the fabrication process where ICG was encapsulated within PLL forming ICG PLL NPs is shown in **Figure 3.2**. Concisely, 20 µL of PLL solution (3 mg/mL) was taken in a 1.5 mL microcentrifuge tube, which was gently mixed with the cocktail of salts, i.e., 13.2 µL tri-sodium citrate (0.01 M) and 2 µL disodium phosphate heptahydrate (0.01 M) for 10 seconds. The clear solution turns turbid, which indicates the initiation of the nucleation process. In the next step, 200 µL ICG was added to the cloudy polymer/salt colloidal solution. The reaction was completed by adding 1 mL of deionized water (DI) to the suspension. Fabricated ICG PLL NPs were then aged for 30 minutes at 4°C. For the fabrication of the stable and monodispersed NPs, the molar charge ratio (MCR) of the solution was set to be 2. The MCR was calculated using **Equation 3.1.**

$$\text{MCR} = \frac{Total\ anionic\ charge\ of\ the\ system}{Total\ cationic\ charge\ of\ polypeptide} \quad \textbf{Equation 3.1}$$

After 30 minutes of aging, the ICG PLL NPs suspension was differentially centrifuged three times at 6,500 rotations per minute (RPM) for 1 min followed by centrifugation at 6,000 RPM for 30 min, and 5,500 RPM for 60 min to get monodisperse NPs.

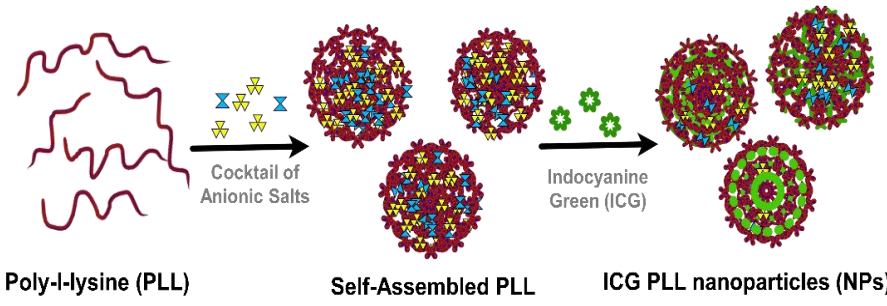

Figure 3.2 Schematic diagram representing the fabrication process of nanoencapsulation of the ICG in the ICG PLL NPs.

3.2.2 Biophysical Characterization

The biophysical characterization of the ICG PLL NPs was done and shown in **Figure 3.3.** The morphology and size distribution of the ICG PLL NPs are determined by FESEM. For FESEM, the NPs were subjected to the freeze-drying step, yet no damage was observed in the NPs, this suggests the robustness of the NPs. The ICG PLL NPs were nearly spherical in shape without any aggregation, as shown in **Figure 3.3(a)**. The inset of **Figure 3.3(a)** shows the image of the NPs pellet, which was used for FESEM characterization. Diameter distribution of lyophilized ICG PLL NPs, analyzed from FESEM images and plotted using IMAGE J software, is shown in **Figure 3.3(b)**. The NPs mean

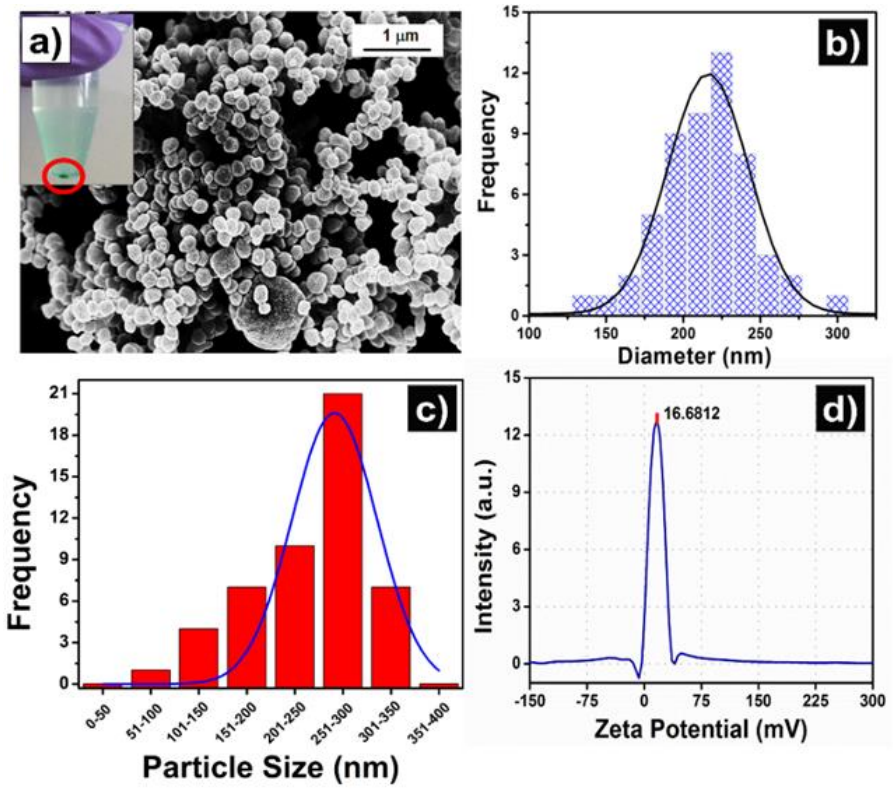

Figure 3.3 Morphological characterization of ICG PLL NPs (a) FESEM image of ICG PLL NPs, the inset shows the green pellet of the NPs (b) frequency diameter distribution of ICG PLL NPs using IMAGE J software. (c) DLS measurement of synthesized ICG PLL NPs shows the average hydrodynamic diameter ranging between 251-300 nm. (d) zeta (ζ) potential of ICG PLL NPs.

diameter was found to be ~225 ± 30 nm.

Additionally, the hydrodynamic diameter and the ζ potential of the ICG PLL NPs in the aqueous solution were measured by DLS. As shown in **Figure 3.3(c)**, the hydrodynamic diameter of ICG PLL NPs ranges between 251 to 300 nm. These NPs also exhibit a high degree of monodispersity with a polydispersity index (PDI) of 0.22. In addition, the ζ potential, which is a function of the particle surface charge and also indicates the stability of the NP, is found to be +16.25 mV, as shown in **Figure 3.3(d).** These results suggest that these particles are stable in the DI water without showing any aggregation.

3.2.3 Effect of pH and MCR on the Particles Size

The self-assembly process for NPs synthesis depends on several factors, such as the concentration of the constituents used for synthesis, pH of the salt solution, incubation time, and MCR, *etc.* The condition for ICG PLL NPs fabrication was optimized by varying multiple parameters. Here, we have shown the effect of variation of parameters such as pH and MCR of the system, on the size of ICG PLL NPs. For studying the pH effect, the samples were prepared by varying the pH value of the salts (ranging from 4.5 to 12). The particle size measurements were carried out by using DLS. As shown in **Figure 3.4(a)**, the diameter of the ICG PLL NPs varies with a change in the pH values of the salts. The optimal pH value of the salt solution was

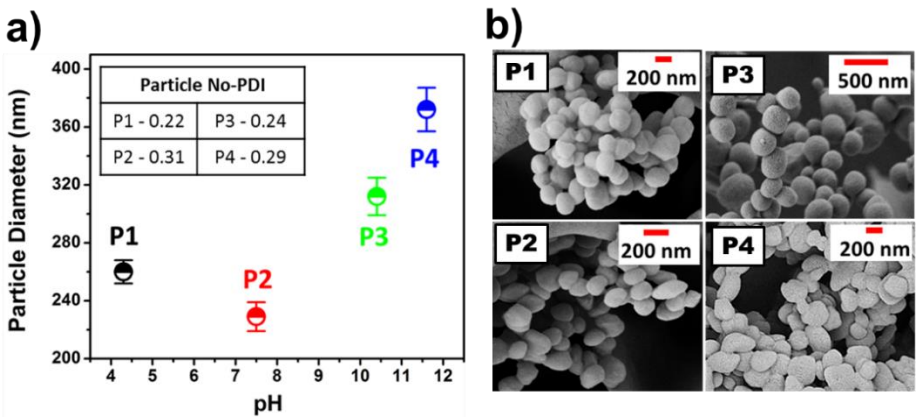

Figure 3.4 Variation in ICG PLL NPs size due to change in salt pH (a) effect of pH on particle size by DLS (b) respective FESEM images.

found to be ~7 (neutral pH) for the fabrication, which produced perfectly spherical ICG PLL NPs of ~229 nm diameter, and the PDI value of 0.31 shows the monodispersity of the formed NPs. The basic pH value of the salt solution (such as 10.4 and 11.6) produced larger size NPs with a particle diameter of more than ~312 nm with lower PDI values. This is due to the variation of the charge ratio of Lysine in this pH. On the other hand, the acidic pH value resulted in the formation of a bit larger ICG PLL NPs with ~260 nm diameter and 0.22 PDI value. This experiment suggests that the neutral pH value of salt solution would give the smallest and most uniform size NPs without aggregation. In addition, to the DLS measurement, the FESEM images of the synthesized NPs at different pH values are shown in **Figure 3.4(b)**.

Similarly, the MCR value of the system plays a crucial role in the fabrication of these NPs. To study the effect of MCR on the size and polydispersity of the NPs, the NPs were fabricated at following MCR values, i.e., 0.5, 1, 1.4, 2, 3, 4, 5, 6, and 7. The size of the NPs was measured by DLS at different MCR values. It was observed that the NPs were not formed when the MCR of the solution was either ≤1 or ≥7 (as shown in solid red circles **Figure 3.5(a)**). However, the stable

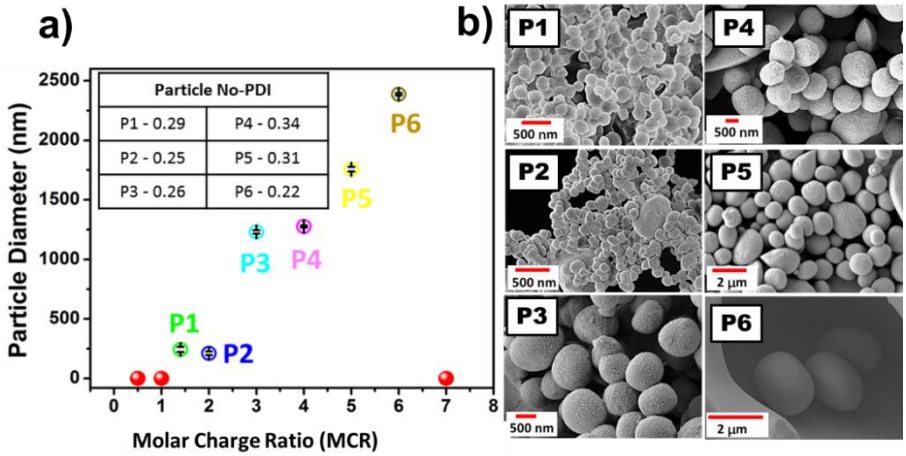

Figure 3.5 Variation in ICG PLL NPs size due to change in the MCR (a) effect of MCR on particle size by DLS (b) respective FESEM images.

NPs were formed when the MCR was within the range of 1 to 7. Different values of the MCR resulted in the different sizes of ICG PLL NPs. The smallest size of the (~222 nm) particles was obtained when the MCR was set to be 2. Further, it was observed that with increasing MCR, there is a linear increase in the particle size. For all the different values of MCR, the PDI was below 0.35, which shows the monodisperse nature of the NPs in aqueous solution. The SEM images of the synthesized NPs at different values of MCR are also shown in **Figure 3.5(b).**

3.2.4 Spectroscopic Characterization

The optical absorption and fluorescence emission spectra of the free ICG and ICG PLL NPs are shown in **Figure 3.6.** The absorption spectrum of the free ICG shows a monomeric peak centered at 782 nm and a smaller aggregated vibrionic shoulder peak at 732 nm[38]. A

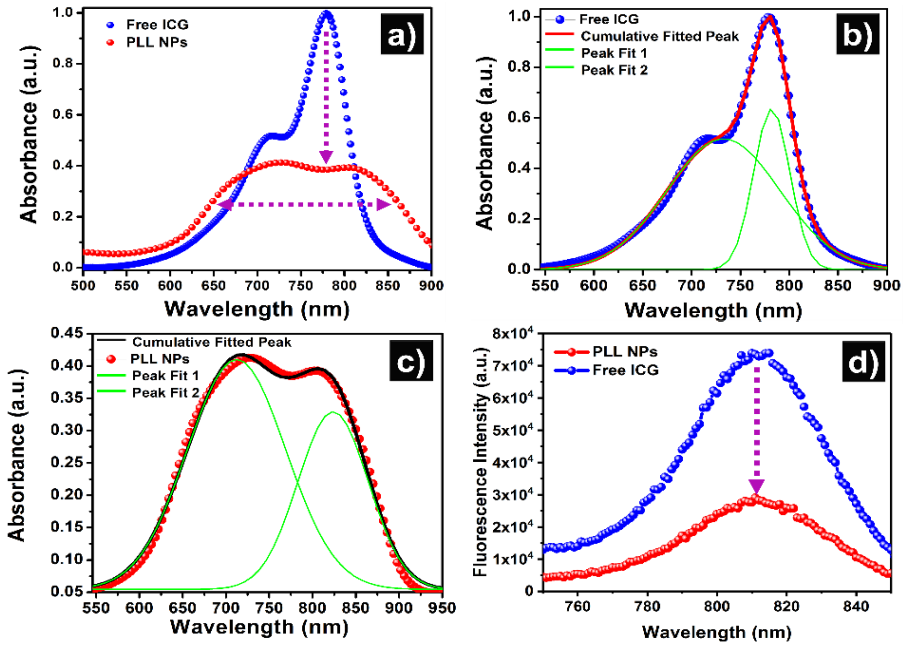

Figure 3.6 Biochemical characterizations of free indocyanine green (ICG) and poly-l-lysine nanoparticles (PLL NPs). (a) Absorption spectra of free ICG and PLL NPs. (b) Absorption spectra curve fitting of free ICG with R^2 = 99.8 %. (c) Absorption spectra curve fitting of PLL NPs with R^2 = 99.4 %. (d) Emission spectra of free ICG and PLL NPs.

significant reduction and noticeable broadening in the absorption spectra are observed for ICG PLL NPs in comparison with the free ICG, as shown in **Figure 3.6(a).** A Gaussian peak fitting was used to differentiate the contribution of the monomeric and aggregated forms of ICG molecules in its free and nanoencapsulated form (ICG PLL NPs), as shown in **Figure 3.6(b and c).** Further, the peak fitted absorption spectrum of ICG PLL NPs in **Figure 3.6(c)**, shows the blue and redshift in these two major peaks of the ICG molecules. The red and blue shift in the absorption peaks indicates the possible H and J aggregation; therefore, this result confirms the encapsulation of the ICG in the aggregated form within ICG PLL NPs. Additionally, a significant broadening of the monomeric peak by 45 nm is observed in the case of ICG PLL NPs in comparison to the free form of the ICG. This suggests that along with aggregates, there might be a significant number of ICG molecules in the monomeric form as well.

In summary, the spectral peak shifting, broadening, and absorption reduction (as shown in **Figure 3.6(a)**) indicate the encapsulation of ICG molecules might be in the aggregated form within ICG PLL NPs. To further confirm the ICG aggregation within ICG PLL NPs, the NIR fluorescence emission of the free ICG and the ICG PLL NPs were collected and compared. The fluorescence emission was recorded from 750 nm to 850 nm after excitation of the samples at 680 nm. The fluorescence spectrum of ICG PLL NPs shows a decrease in fluorescence emission as compared with the free ICG, as shown in **Figure 3.6(d)**. This decrease in fluorescence emission of ICG within ICG PLL NPs could be attributed to aggregation-caused quenching (ACQ).

3.2.5 Interaction Study of Salt, ICG, and Polymer

The constituents of NPs are PLL, ICG, and salts, which form nanostructure via self-assembly mechanism. Their ability to interact with each other and form complex is the fundamental basis for the

fabrication of these NPs (**Figure 3.7**). We used circular dichroism (CD) spectroscopy to probe the influence of salt and ICG in ICG PLL NPs fabrications. **Figure 3.7(a)** shows the CD spectra of aqueous PLL, PLL with a salt solution, and ICG PLL NPs. The CD spectrum of PLL exhibits one negative band in the ultraviolet region at ~207 nm and one positive band at ~218 nm, which confirms its random coil conformation.[39] **Figure 3.7(a)** shows an increase in the band intensity at 207 nm and a decrease in band intensity at 218 nm after the addition of the salt solution, which corresponds to the interaction of PLL molecules with salts. Further, the addition of ICG to the complex of PLL and salt increases the intensity of the peak at ~207 nm and a reduction of the peak at ~218 nm. These changes in CD spectra confirm the formation of the nanostructure, as shown earlier by the SEM imaging. This result suggests that ICG actively interacts with PLL molecules and contributes to the formation of the stable nanostructure.

To further understand the role of ICG in nanostructure formation, *in-silico* studies were carried out on the PLL and ICG complexation. Docking studies are generally carried out to obtain detailed information about the binding interactions involved during the complexation of the macromolecule with the ligand.[40] There have been numerous experimental studies on the self-assembly process for the fabrication of NPs. However, there is rarely any report to show the *in-silico* interaction of ligand and macromolecule during the self-assembly process. In this study, PLL was used as a macromolecule, and ICG was used as a ligand for the *in-silico* studies to show the interaction between them during NP formation. This result shows that the net negative charge on ICG plays an important role in the self-assembly process and contributes to the formation of stable ICG PLL NPs. The docking results show that there is active binding between ICG (ligand) and PLL (macromolecule). Specifically, the binding between ICG and PLL is due to the interaction between the lysine residues of PLL and sulfonate groups of ICG, as shown in **Figure 3.7(c**

and d). It was found that the docked ligand is close to Lysine and lies within the hydrogen bonding distance with the sulfonate group. The distance from Lysine residue of PLL to the adjacent oxygen atom of ICG lies in the range of 1.8 Å to 2.2 Å, which is calculated by the University of California, San Francisco (UCSF) chimera Viewer. Our study reveals that the docked ICG makes two hydrogen bonds with Lysine, and the bond length was < 2.2 Å, thus suggests a possible aggregation of ICG molecule within PLL/salt aggregates. The free energy change of binding of the most populated energy cluster obtained from blind docking of the PLL using AutoDock is found to be -ve 3.28 kcal mol^{-1} at 298 K. This study confirms the experimental findings of CD measurements of ICG-PLL complex formation. This also confirms the active participation of the ICG in the formation of ICG PLL NPs via the self-assembly method.

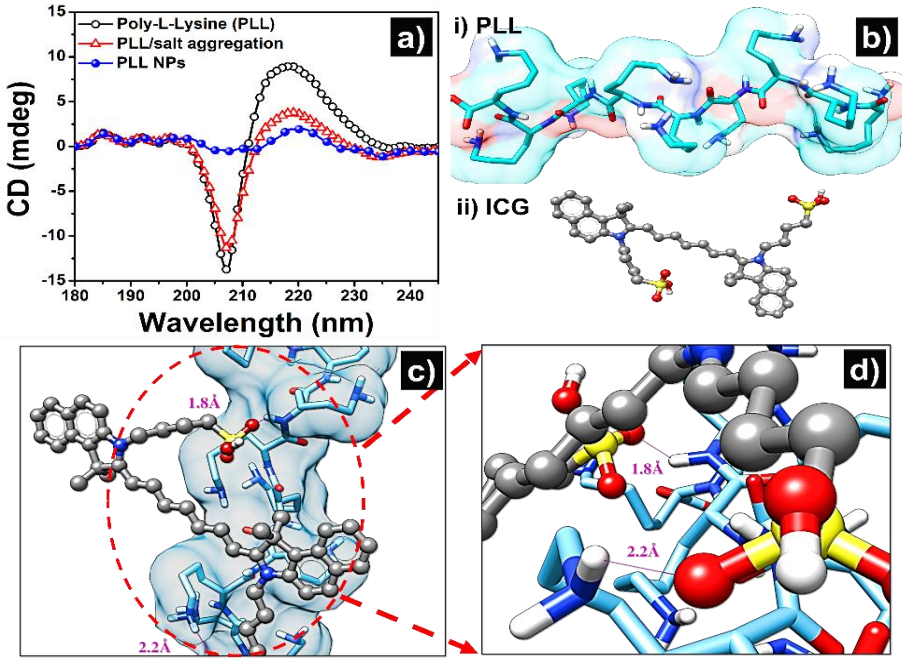

Figure 3.7 Interaction of the PLL and ICG (a) CD spectra of PLL and its interaction with salt and ICG (b) 3D structure of PLL and ICG used for docking (c) complex of PLL and ICG show its favorable docking site (d) docking results with two hydrogen bonds. Where the carbon atoms of ICG are grey, oxygen-red, hydrogen white and sulfur–yellow, carbon atoms of PLL are cyan, nitrogen is blue, and hydrogen is white.

3.2.6 Encapsulation Efficiency

As seen above, due to the possible aggregation of ICG molecules within ICG PLL NPs, these NPs might have higher encapsulation efficiency. The encapsulation efficiency of ICG within ICG PLL NPs was estimated using **Equation 3.2.**

$$EE\ \% = \left(\frac{\text{The concentration of ICG after disassembly of NPs}}{\text{The total concentration of ICG used for the synthesis}}\right) * 100 \ldots \textbf{Equation 3.2}$$

This method provides a molar concentration of entrapped ICG within the ICG PLL NPs. For the concentration estimation, ICG PLL NPs were dissolved in DMSO, which causes the instant release of the ICG from the NPs. Following the addition of DMSO, the ICG content was quantified by measuring the absorption at 798 nm in the UV-Vis-NIR spectrophotometer. The ICG encapsulation efficiency was found to be 43.4 ± 5%.

3.2.7 *In-vitro* Release Study

Smart nanostructure, which could release its cargo under a specific environment are promising carriers for drug delivery.[41, 42] These NPs are designed to deliver the cargo in a specific environment, such

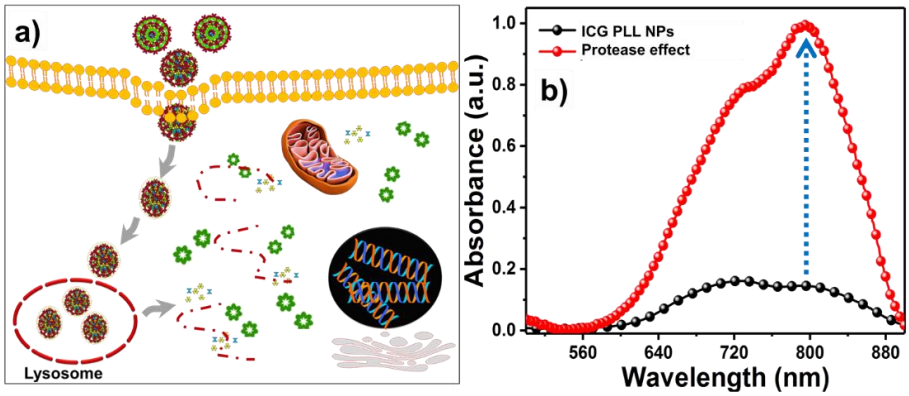

Figure 3.8 Release mechanism (a) ICG release mechanism (b) Absorption spectra showing free ICG specra recovery after incubation with proteolytic enzyme.

as pH, a proteolytic enzyme, *etc*. It has been shown that PLL degrades in the presence of proteolytic enzymes.[43, 44] The design rationale of protease responsive NPs lies in the fact that the proteolytic enzymes are present in the lysosomal compartment, which hydrolyze these NPs and triggers the release of encapsulated cargo.[39, 45, 46] Similarly, the advantage of ICG PLL NPs is that the cargo release will be governed by the proteolytic enzymes. Therefore, ICG PLL NPs would only release ICG when taken up into the cells via endocytosis and trafficked to lysosomes, where proteolytic enzymes degrade ICG PLL NPs, as shown in **Figure 3.8(a)**. However, the degradation byproducts of these NPs are the fragments of Lysine, salts, and the free form of ICG. These byproducts would be utilized by the cells without showing any toxic effect, whereas the ICG would be used to stain the cells for NIR bioimaging. The recovery of free ICG absorption spectra (**Figure 3.8(b)**) after proteolytic enzyme incubation confirms our hypothesis, ICG PLL NPs are readily taken up by the cells via endocytosis and get degraded in the presence of a proteolytic enzyme in the lysosomes of the cells, which subsequently results in the release of the free-form of the ICG from NPs. The schematic of a proposed mechanism for the *in-vitro* release study of the ICG from ICG PLL NPs is shown in **Figure**

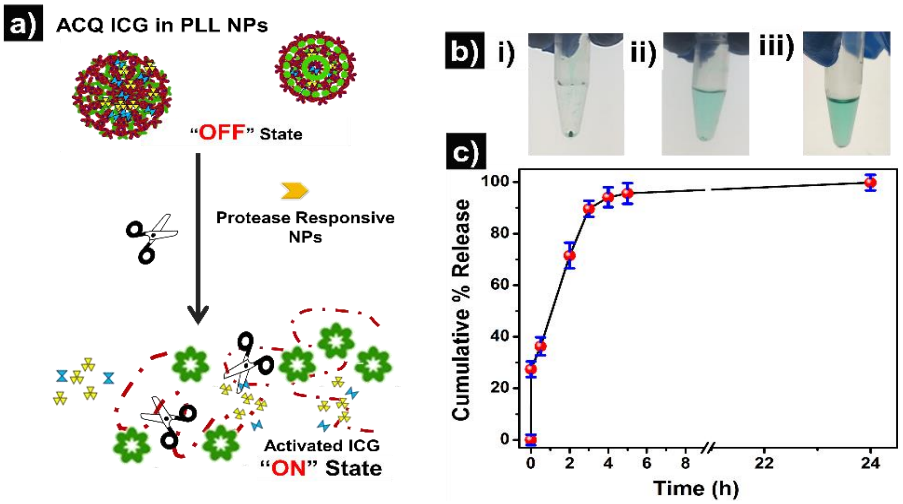

Figure 3.9 Release study of the ICG from polypeptide NPs (a) pictorial visualization of the pellet after every hour release study (b) enzymatic cleavage of the NPs and invitro release stydy in presence of trypsin for 24 h.

3.9(a). As evident from the emission measurements, the fluorescence emission from ICG PLL NPs is significantly lower than the free form of the ICG due to ACQ termed as "OFF state." However, the hydrolysis of ICG PLL NPs via proteolytic enzyme results in the fragments of Lysine, salts, and free form of the ICG termed as activated ICG "ON state." The released activated ICG within the cells is in monomeric form in comparison with an aggregated form within ICG PLL NPs. Thus, the loaded ICG is protected within ICG PLL NPs under the physiological and gets delivered to the cells. The *in-vitro* release behavior of the ICG from ICG PLL NPs was studied after the incubation of NPs with a proteolytic enzyme, which mimics the condition of lysosomes. Under this condition, the ICG release kinetics from ICG PLL NPs was observed and is shown in **Figure 3.9(b and c)**. **Figure 3.9 (b- (i, ii, and iii))** shows the digital picture of the Eppendorf tube showing ICG release from ICG PLL NPs when incubated with a proteolytic enzyme (trypsin) for 5 minutes, 4 hours(h), and 24 h respectively. As seen in **Figure 3.9(b-i)**, 5 minutes incubation of ICG PLL NPs with proteolytic enzyme results in very less release of the ICG. After 4 h of the incubation, more than 90% of ICG was released from the NPs, and a tiny NP pellet was observed. However, no pellet was observed after 24 h of the incubation. **Figure 3.9(c)** shows the ICG release kinetics at different time points. As seen in **Figure 3.9(c)**, an initial abrupt release of about 38 % of ICG from ICG PLL NPs was observed within 30 minutes of trypsin incubation. In the next 4 h, more than 90 % of ICG was released, which confirms the enzymatic degradation property of ICG PLL NPs. This enzymatic degradation of ICG PLL NPs within cells would help them for a controlled release only within cells and would protect ICG while in circulation.

3.2.8 Photo-Stability of Free ICG and ICG PLL NPs

Free ICG is an unstable chromophore; its optical properties get deteriorated when stored or exposed to ambient light. Therefore, for

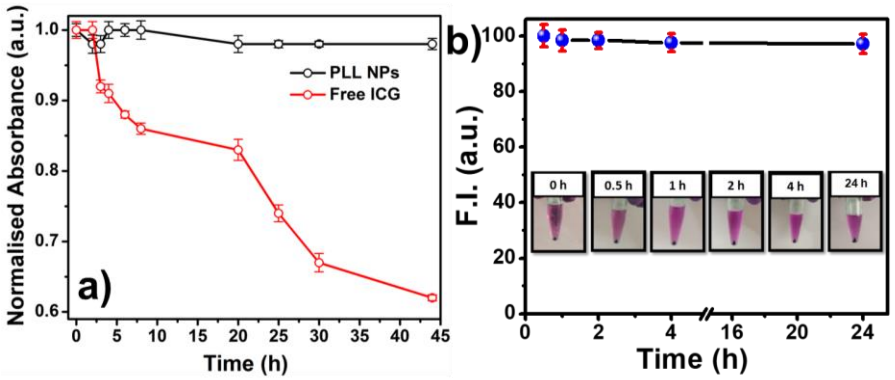

Figure 3.10 Photostability of the ICG PLL NPs (a) ICG PLL NPs vs. free ICG in ambient light exposure at room temperature (b) ICG PLL NPs stability in the presence of culture media.

the imaging-based biomedical applications, it is important to protect free ICG from the exposure of ambient light. The nanoencapsulation of ICG might protect it from unwanted exposure of light and maintain its optical properties. The effect of nanoencapsulation on the optical stability of ICG was studied and compared with the free ICG. To study the effect of light exposure, both the samples were exposed to ambient light at room temperature (RT) for 45 h. At each time point, the absorbance of ICG PLL NPs and free ICG was measured by spectrophotometer. As shown in **Figure 3.10(a)**, ICG PLL NPs are more optically stable than free ICG under ambient light exposure at RT. Moreover, the free ICG almost lost ~40% of its optical activity when exposed to ambient light. This result suggests that the nanoencapsulation of free ICG also protects it from optical degradation. Similarly, the stability of ICG PLL NPs in the physiological environment was studied by incubating them in cell culture media for 24 h at 37 ° C. As shown in **Figure 3.10(b)**, ICG PLL NPs were 93 % stable in the physiological condition. According to the results, ICG PLL NPs are stable nanocarriers for ICG delivery in the cells.

3.2.9 Cellular toxicity and uptake study

For biomedical applications, the safety of these NPs needs to be established. The *in-vitro* cytotoxicity of ICG PLL NPs was evaluated through MTT assay, and cellular imaging was done on HeLa cells, as shown in **Figure 3.11**. The result of cell viability where HeLa cells were incubated with different concentrations of ICG PLL NPs for 24 h, as shown in **Figure 3.11(a).** The cells incubated with 2 µL and 5 µL concentration of ICG PLL NP show more than 94 % viability at both concentrations. However, the cells incubated with 10 µL and 20 µL ICG PLL NPs were also found to be safe and showed ~89 % and ~82 % cellular viability, respectively. A decrease in the cellular viability was observed when cells were incubated with 50 µL of ICG PLL NPs; these cells showed ~60 % cellular viability. The HeLa cells without

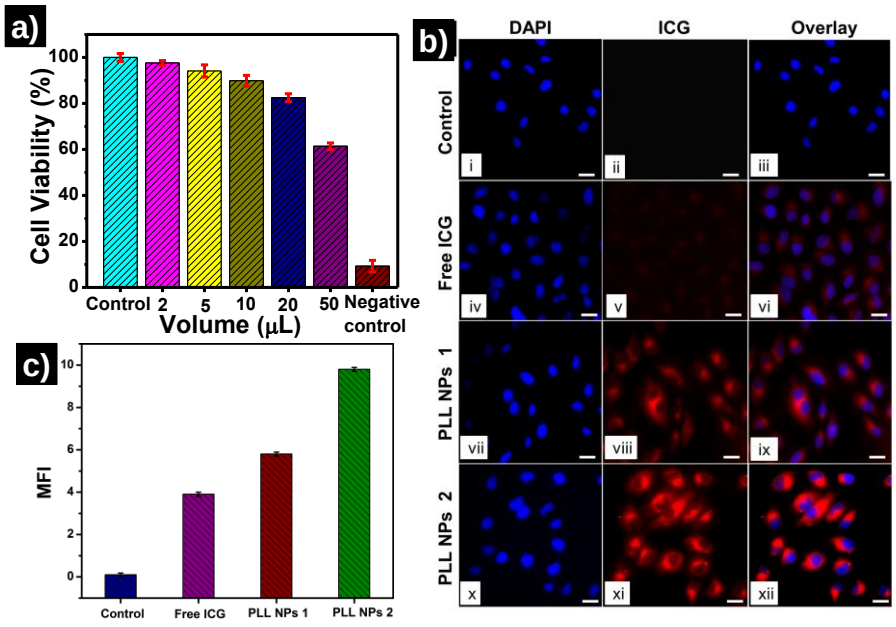

Figure 3.11 Cellular viability and NIR imaging of HeLa cells treated with free indocyanine green (ICG) and ICG encapsulated poly-l-lysine nanoparticles (PLL NPs). (a) The cellular viability of two different concentrations of PLL NPs with positive and negative control. (b) NIR imaging of HeLa cells, where (i-iii) were control cells, (iv-vi) free ICG treated cells and (vii-xii) were treated with two different concentrations of PLL NPs. The DAPI staining nuclei are denoted in blue, and ICG emission was denoted in red colour. Scale bar: 20 µm. (c) Fluorescence intensity quantification by IMAGE J software.

any treatment were used as a positive control. The cells incubated with Triton x were used as a negative control and showed less than 10 % cell viability. This result suggests that ICG PLL NPs are safe to be used as a delivery vehicle, as reported for biomedical applications. Following the cell viability study, experiments were carried out to study the potential of ICG PLL NPs for drug or contrast agent delivery applications. For the bioimaging experiment, HeLa cells were incubated with free ICG, two concentrations of ICG PLL NPs, and PBS (as control) for 4 h. Results of cellular imaging are shown in **Figure 3.11(b)**, where column 1 shows the nuclei of the cells stained with DAPI (blue), column 2 shows the NIR fluorescence emission from ICG (red) and column 3 shows the merged image of the channel 1 and 2. The rows represent the following treatment; the first row shows control. The second row shows free ICG, and two different concentrations of ICG PLL NPs are shown in third and fourth rows, respectively. As expected, no fluorescence emission was detected from control HeLa cells, and a weak fluorescence is observed from free ICG incubated cells. This indicates that free ICG was not readily taken up by the cells in 4 h incubation. However, significantly higher fluorescence emission was observed from ICG PLL NPs treated cells. In addition, if the concentration of ICG PLL NPs is increased, the higher fluorescence emission from the cells is observed.

Cellular imaging results confirm the significantly higher fluorescence emission from ICG PLL NPs treated cells than free ICG treated cells, which shows the effectiveness of ICG PLL NPs for NIR imaging. It is pertinent to note that fluorescence emission is emitted from the cytosol of the cells, this is possible due to proteolytic degradation of ICG PLL NPs in the lysosomes. To quantify the fluorescence emission from the different treatments, the mean fluorescence intensity (MFI) of NIR fluorescence emission from HeLa cells was calculated using IMAGE J software (shown in **Figure 3.11(c)**). It is important to note that control cells showed no fluorescence, and ICG PLL NP treated cells showed the highest NIR

fluorescence. This result supports our *in-vitro* release study, which indicates that ICG PLL NPs are efficient biological nanocarrier for delivering ICG to the cells for enhanced SNR of NIR imaging. In addition to the delivery of ICG to the cells, the ICG PLL NPs can also be used to encapsulate and deliver the therapeutic agents to the targeted cells and tissues.

3.3 Conclusion

In summary, we have demonstrated the green chemistry-based fabrication of ICG encapsulated ICG PLL NPs. The ICG loaded ICG PLL NPs were fabricated using a self-assembly method at room temperature without using any organic or toxic solvents. The NPs have a spherical morphology and high encapsulation efficiency of ICG. These NPs are highly monodispersed with positive zeta potential and without aggregation. The cellular viability studies showed that more than 95 % of ICG PLL NPs treated cells were viable after 24 h of incubation. In addition, the release of the cargo was facilitated only inside the cells via proteolytic enzymatic degradation. The biocompatibility (with zero toxicity) and biodegradability of these NPs make them a suitable carrier for drug delivery and the delivery of exogenous contrast agents. Therefore, these ICG PLL NPs may serve as a potential nanocarrier for various theranostic applications.

3.4 References

1. World Health Organization (2017) Guide to cancer early diagnosis. World Heal Organ 1–48

2. Benson RC, Kues HA (1978) Fluorescence properties of indocyanine green as related to angiography. Phys Med Bol 23:159–163. https://doi.org/10.1088/0031-9155/23/1/017

3. Fickweiler S, Szeimies RM, Bäumler W, *et al.* (1997) Indocyanine Green: Intracellular Uptake and Phototherapeutic

Effects in vitro. J Photochem Photobiol B Biol 38:178–183. https://doi.org/10.1016/S1011-1344(96)07453-2

4. Zhou JF (1994) Aggregation and Degradation of Indocyanine Green. Proc SPIE 2128:495–505. https://doi.org/10.1117/12.184936

5. Weigand R, Rotermund F, Penzkofer a (1997) Aggregation Dependent Absorption Reduction of Indocyanine Green. J Phys Chem A 101:7729–7734. https://doi.org/10.1021/jp9700894

6. Shi J, Votruba AR, Farokhzad OC, Langer R (2010) Nanotechnology in drug delivery and tissue engineering: From discovery to applications. Nano Lett 10:3223–3230. https://doi.org/10.1021/nl102184c

7. Resort K, Hp S (2009) Impact of Nanotechnology on Drug Discovery & Development Pharmanext. ACS Nano 3:16–20

8. Senapati S, Mahanta AK, Kumar S, Maiti P (2018) Controlled drug delivery vehicles for cancer treatment and their performance. Signal Transduct Target Ther 3:7. https://doi.org/10.1038/s41392-017-0004-3

9. Khodabandehloo H, Zahednasab H, Ashrafi Hafez A (2016) Nanocarriers Usage for Drug Delivery in Cancer Therapy. Iran J Cancer Prev In Press: https://doi.org/10.17795/ijcp-3966

10. Rodriguez VB, Henry SM, Hoffman AS, *et al.* (2008) Encapsulation and stabilization of indocyanine green within poly(styrene-alt-maleic anhydride) block-poly(styrene) micelles for near-infrared imaging. J Biomed Opt 13:014025. https://doi.org/10.1117/1.2834296

11. Licha K, Welker P, Weinhart M, *et al.* (2011) Fluorescence imaging with multifunctional polyglycerol sulfates: Novel polymeric near-IR probes targeting inflammation. Bioconjug

Chem 22:2453–2460. https://doi.org/10.1021/bc2002727

12. Manchanda R, Fernandez-Fernandez A, Nagesetti A, McGoron AJ (2010) Preparation and characterization of a polymeric (PLGA) nanoparticulate drug delivery system with simultaneous incorporation of chemotherapeutic and thermo-optical agents. Colloids Surfaces B Biointerfaces 75:260–267. https://doi.org/10.1016/j.colsurfb.2009.08.043

13. Altınoglu EI, Russin TJ, Kaiser JM, *et al.* (2008) Near-Infrared Emitting FluorophoreDoped Calcium Phosphate Nanoparticles for In Vivo Imaging of Human Breast Cancer. ACS Nano 2:2075–2084

14. Yaseen MA, Yu J, Wong MS, Anvari B (2007) Stability assessment of indocyanine green within dextran-coated mesocapsules by absorbance spectroscopy. J Biomed Opt 12:064031. https://doi.org/10.1117/1.2821423

15. Saxena V, Sadoqi M, Shao J (2004) Indocyanine green-loaded biodegradable nanoparticles: Preparation, physicochemical characterization and in vitro release. Int J Pharm 278:293–301. https://doi.org/10.1016/j.ijpharm.2004.03.032

16. Saxena V, Sadoqi M, Shao J (2004) Enhanced photo-stability, thermal-stability and aqueous-stability of indocyanine green in polymeric nanoparticulate systems. J Photochem Photobiol B Biol 74:29–38. https://doi.org/10.1016/j.jphotobiol.2004.01.002

17. Derfus AM, Chan WCW, Bhatia SN (2004) Probing the cytotoxicity of semiconductor quantum dots. Nano Lett 4:11–18. https://doi.org/10.1021/nl0347334

18. Jeng HA, Swanson J (2006) Toxicity of metal oxide nanoparticles in mammalian cells. J Environ Sci Heal Part A 41:2699–2711. https://doi.org/10.1080/10934520600966177

19. Maynard AD, Aitken RJ, Butz T, *et al.* (2006) Safe handling of nanotechnology. Nature 444:267–269. https://doi.org/10.1038/444267a

20. Cheng Z, Al Zaki A, Hui JZ, *et al.* (2012) Multifunctional Nanoparticles: cost versus benefit of adding targeting and imaging capabilities. Science (80-) 338:903–910. https://doi.org/10.1126/science.1226338

21. Loo C, Lin A, Hirsch L, *et al.* (2004) Nanoshell-enabled photonics-based imaging and therapy of cancer. Technol Cancer Res Treat 3:33–40. https://doi.org/10.1177/153303460400300104

22. Wang Y, Bansal V, Zelikin AN, Caruso F (2008) Templated synthesis of single-component polymer capsules and their application in drug delivery. Nano Lett 8:1741–1745. https://doi.org/10.1021/nl080877c

23. Ashley CE, Carnes EC, Phillips GK, *et al.* (2011) Cell-specific delivery of diverse cargos by bacteriophage MS2 virus-like particles. ACS Nano 5:5729–5745. https://doi.org/10.1021/nn201397z

24. Maruyama K (2011) Intracellular targeting delivery of liposomal drugs to solid tumors based on EPR effects. Adv Drug Deliv Rev 63:161–169. https://doi.org/10.1016/j.addr.2010.09.003

25. Tome D, Bos C (2007) Lysine requirement through the human life cycle. J Nutr 137:164 (2S–5S)

26. Datta D, Bhinge A, Chandran V (2001) Lysine : Is it worth more ? Cytotechnology 36:3–32

27. Singh M, Rao DM, Pande S, *et al.* (2011) Medicinal uses of L-lysine : past and future. Int J Res Pharm Sci 2:637–642

28. Anjum F, Mahajan R, Nazir M, *et al.* (2017) Common Bean (Phaseolus vulgaris L.) A Source of Essential Amino Acid: Lysine. Adv Biotechnol Biochem Acid 2017:2–5. https://doi.org/10.29011/2574-7258.00002

29. Yavin E, Yavin Z (1974) Attachment and culture of dissociated cells from rat embryo cerebral hemispheres on polylysine-coated surface. J Cell Biol 62:540–6. https://doi.org/10.1083/jcb.62.2.540

30. Wagner E, Zenke M, Cotten M, *et al.* (1990) Transferrin-Polycation Conjugates as carriers for DNA Uptake into Cells. Proc Natl Acad Sci U S A 87:3410–4. https://doi.org/10.1073/pnas.87.9.3410

31. Liu P, Li Z, Zhu M, *et al.* (2010) Preparation of EGFR Monoclonal Antibody Conjugated Nanoparticles and Targeting to Hepatocellular Carcinoma. J Mater Sci Mater Med 21:551–556. https://doi.org/10.1021/bc700410z

32. Orive G, Tam SK, Pedraz JL, Hallé JP (2006) Biocompatibility of Alginate-Poly-l-lysine Microcapsules for Cell Therapy. Biomaterials 27:3691–3700. https://doi.org/10.1016/j.biomaterials.2006.02.048

33. Babic M, Horak D, Trchova M, *et al.* (2008) Poly(L-lysine)-Modified Iron Oxide Nanoparticles for Stem Cell Labeling. Bioconjug Chem 19:740–750. https://doi.org/10.1021/bc700410z

34. Maruyama A, Ishihara T, Kim JS, *et al.* (1997) Nanoparticle DNA Carrier with Poly(L-lysine) Grafted Polysaccharide Copolymer and Poly(D,L-lactic acid). Bioconjug Chem 8:735–742. https://doi.org/10.1021/bc9701048

35. Zheng X, Zhou F, Wu B, *et al.* (2012) Enhanced tumor

treatment using biofunctional indocyanine green-containing nanostructure by intratumoral or intravenous injection. Mol Pharm 9:514–522. https://doi.org/10.1021/mp200526m

36. Wu L, Fang S, Shi S, *et al.* (2013) Hybrid polypeptide micelles loading indocyanine green for tumor imaging and photothermal effect study. Biomacromolecules 14:3027–3033. https://doi.org/10.1021/bm400839b

37. Wang X, Peng H, Yang W, *et al.* (2017) Indocyanine green-platinum porphyrins integrated conjugated polymer hybrid nanoparticles for near-infrared-triggered photothermal and two-photon photodynamic therapy. J Mater Chem B 5:1856–1862. https://doi.org/10.1039/c6tb03215j

38. Zhou JF, Chin MP, Schafer SA (1994) Aggregation and degradation of indocyanine green. Proc SPIE 2128:495–505. https://doi.org/10.1117/12.184936

39. Wang Y, Chang YC (2003) Synthesis and conformational transition of surface-tethered polypeptide: Poly(L-lysine). Macromolecules 36:6511–6518. https://doi.org/10.1021/ma034093r

40. Yadav P, Bandyopadhyay A, Chakraborty A, Sarkar K (2018) Enhancement of anticancer activity and drug delivery of chitosan-curcumin nanoparticle via molecular docking and simulation analysis. Carbohydr Polym 182:188–198. https://doi.org/10.1016/j.carbpol.2017.10.102

41. Gilmore BF (2012) Proteases as Selective Activators of Triggered Drug Release : A Potential Answer to the Problem of Biomaterial-Associated Infections ? J Biotechnol Biomater 2:1–3. https://doi.org/10.4172/2155-952X.1000e111

42. Habibi N, Kamaly N, Memic A, Shafiee H (2016) Self-

assembled peptide-based nanostructures: Smart nanomaterials toward targeted drug delivery. Nano Today 11:41–60. https://doi.org/10.1016/j.nantod.2016.02.004.Self-assembled

43. Ryser HJ-P, Shen W (1980) Conjugation of Methotrexate to Poly (L-Lysine) as a Potential Way to Overcome Drug Resistance. Cancer 45:1207–1211

44. Shen W, Ryser HJ-P (1978) Conjugation of poly-L-lysine to albumin and horseradish peroxidase : A novel method of enhancing the cellular uptake of proteins. Proc Natl Acad Sci U S A 75:1872–1876

45. Waley SG, Watson J (1953) The Action of Trypsin on Polylysine. Biochemistry 55:328–337. https://doi.org/10.1021/bi00908a017

46. Shazly G, Nawroth T, Langguth P (2008) Comparison of Dialysis and Dispersion Methods for In Vitro Release Determination of Drugs from Multilamellar Liposomes. Dissolution Technol 7–10

Chapter 4

Nonlinear Optical Properties of ICG for Multiphoton Bioimaging

4.1 Introduction

Conventionally ICG is being used as a NIR imaging probe due to its absorption and emission in the NIR wavelength range. However, it also shows absorption in the near UV and visible wavelength range, which are not studied and explored for any application. In this chapter, efforts have been made to study the unexplored optical characteristics of ICG and their possible applications in the field of medicine and biology.

Over the past few decades, multiphoton fluorescence imaging has received much attention due to its several advantages over the NIR fluorescence imaging technique.[1] It provides the 3D imaging capability of thick tissues (few hundred micrometers) with reduced photobleaching and photodamage to the nearby tissues.[2, 3] Additionally, it has the potential to detect early-stage cancer.[1] Generally, researchers have relied upon the endogenous molecules for the contrast in multiphoton imaging. However, it has been shown that the inclusion of exogenous imaging probe could further enhance imaging contrast, sensitivity, and SNR for multiphoton imaging.[2, 3] Development of exogenous multiphoton imaging probe could lead researchers to envision a new age of cancer diagnosis by multiphoton imaging.

In this chapter, the nonlinear excitation properties of ICG have been studied thoroughly for the first time. It has been observed that

This chapter is largely taken from ***Kumari, A.*** *and Gupta, S. "Two-photon excitation and direct emission from S_2 state of U.S. Food and Drug Administration approved near-infrared dye: Application of anti-Kasha's rule for two-photon fluorescence imaging." J. Biophotonics, 2019; 12: e201800086.*

apart from the well-known NIR absorption peak at 780 nm ICG shows two additional absorption bands at ~400 nm and ~230 nm. There was negligible information available in the literature about the origin of these absorption bands and their possible applications. Therefore, in this thesis, an effort has been made to understand the origin of these bands and their potential applications. The results described in this thesis suggest that ICG could be used as an exogenous contrast agent for multiphoton bioimaging.

4.2 Optical Characteristics of ICG

The optical properties of ICG were studied by absorption and fluorescence emission spectroscopy. ICG is a polymethine dye comprising two aromatic nitrogen-containing heterocycles bridged by the heptamethine chain with a molecular weight of 774.96 Da, as shown in **Figure 4.1(a).**[4] It is an amphiphilic molecule with a hydrophilic sulfonate group and a lipophilic polycyclic group. The absorption spectra of ICG in aqueous solution from UV to NIR wavelength range is shown in **Figure 4.1(b)**. Apart from the well-known NIR peak, at ~780 nm with a shoulder peak at ~710 nm, ICG also exhibits peaks at ~400 nm and ~230 nm. Following is the in-depth study of the origin and possible applications of these absorption bands.

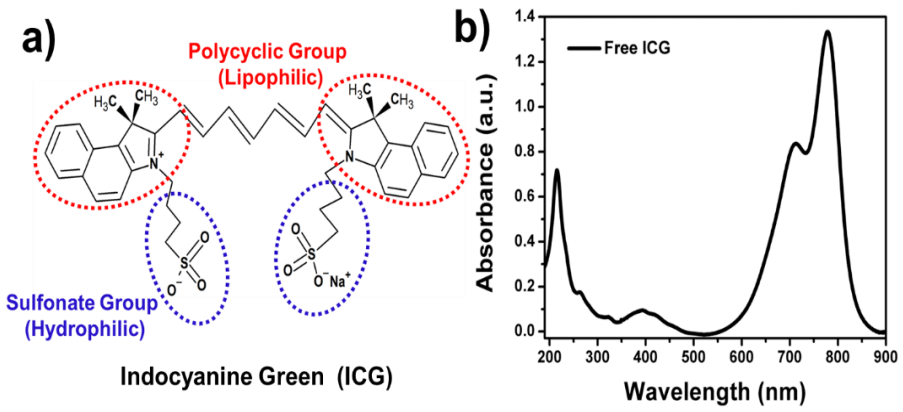

Figure 4.1 Optical characteristics and molecular structure of ICG (a) molecular structure of ICG (b) absorption spectrum of free ICG.

4.2.1 ICG as a Two-photon (2P) Imaging Probe for Multiphoton Bioimaging Application

4.2.1.1 Absorption Spectroscopy

In this section, the application and utility of the peak at 400 nm have been discussed thoroughly. As shown in **Figure 4.2(a),** the presence of an absorption peak at ~780 nm excites electrons of the ICG from the ground (S_0) state to the first excited singlet (S_1) state (S_0 ➔ S_1). Apart from the NIR absorption band, ICG also shows a significant absorption peak at ~393 nm. To obtain more information about these different absorption peaks of ICG, peak fitting-based deconvolution was performed on the absorption spectrum, as shown in Figure 4.2(a). The peak fitting parameters show the presence of three major peaks centered at ~780 nm (Full Width at Half Maxima; FWHM: 50 nm, Area: 36.69 a.u.), ~710 nm (FWHM: 53 nm, Area: 69.06 a.u.), and ~393 nm (FWHM: 109.53 nm, Area: 08.14 a.u.) with R^2 value ~99.99%. Therefore, the presence of an absorption peak at ~393 nm excites ICG electrons from S_0 to the second excited singlet (S_2) state (S_0 ➔ S_2), as shown in **Figure 4.2(b)**.

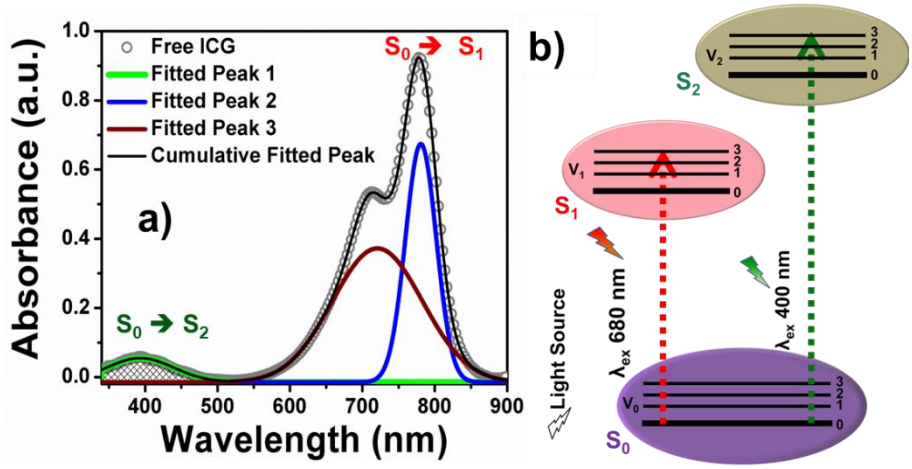

Figure 4.2 Indocyanine green optical characteristics (a) optical absorption spectra (b) Jablonski diagram showing transitions of ICG.

4.2.1.2 Fluorescence Spectroscopy

Further, the ICG fluorescence emission was measured after the excitation at the 680 nm and 400 nm. As shown in **Figure 4.3(a)**, a well-known emission peak was observed at ~810 nm, when ICG was excited by 680 nm. This emission was due to the relaxation of the ICG electrons from S_1 ➔ S_0 state following a 680 nm excitation. The emission-excitation matrix (EEM) spectra of free ICG was measured to study the finer details that how the fluorescence properties vary with excitation wavelength. **Figure 4.3(b)** shows the EEM of the free ICG when excited between 620 nm to 750 nm. The ICG EEM reveals the fluorescence intensity as a function of wavelength and shows a

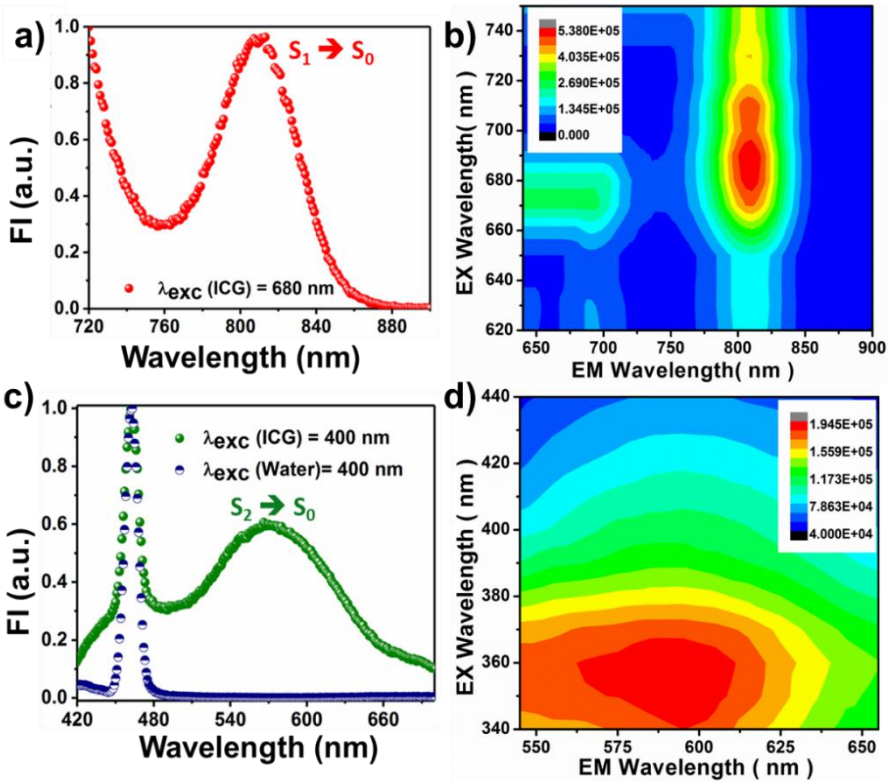

Figure 4.3 Fluorescence emission (a) emission spectra after excitation at 680 nm (b) excitation-emission matrix (EEM) after excitation in the range of 620 to 750 nm (c) emission spectra after excitation at 400 nm (b) EEM of ICG after excitation in the range of 340 to 365 nm. Here S_0 is Ground state, S_1 and S_2 is first and second excited singlet state, EM is Emission, and EX is Excitation.

maximum excitation ranges between 675 nm - 690 nm with emission maxima ranges between 800 nm – 810 nm. Similarly, the fluorescence emission was measured after the excitation at 400 nm. Interestingly, the emission peak was observed at ~575 nm (**Figure 4.3(c)**), showing ICG dual emission property. This emission was peculiar, which makes ICG a molecule that violates the Kasha's rule. The Kasha's rule is a general principle governing the photophysics of electronically excited molecules. It states that fluorescence occurs from the lowest excited states with the lowest energy of a given multiplicity. Although Kasha's rule has general acceptance, however, there are few compounds such as azulenes, cyclazine, and aromatic acenes, which are an exception to this rule and violate Kasha's rule by showing emission from higher excited energy states simultaneously along with lowest excited energy state.[5, 6] Also, a sharp peak at 500 nm is also observed, which is the characteristic Raman peak of water molecules.

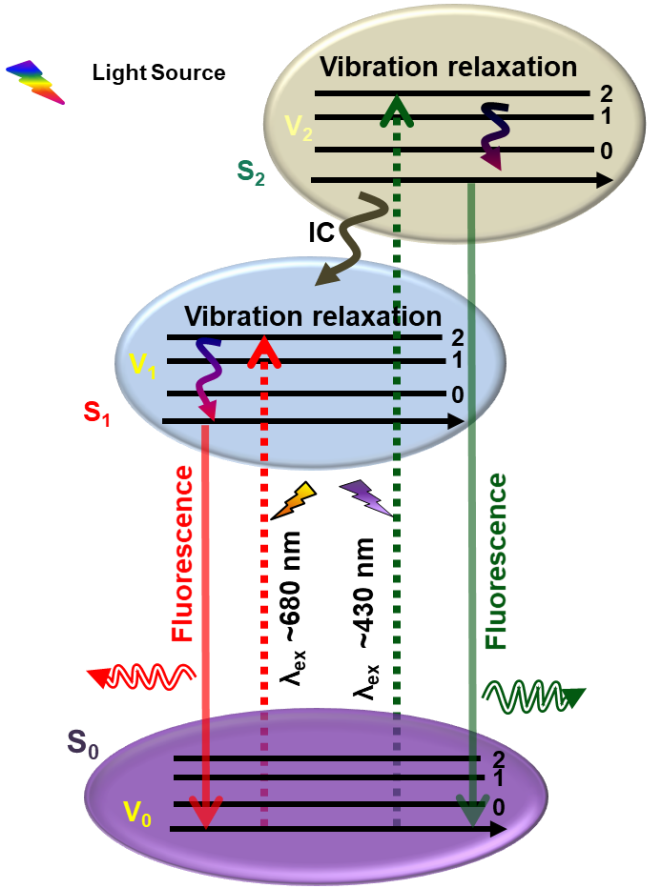

Figure 4.4 Jablonski diagram of the ICG transitions.

It is pertinent to note that the newly found emission of ICG from ICG is due to the transition of electrons from S_2 ➔ S_0 state. Similarly, the EEM for this transition was also measured after excitation from 340 nm to 440 nm, as shown in **Figure 4.3(d)**. The matrix suggests that maximum emission could be achieved after excitation between 340 nm–365 nm. Briefly, the absorption and emission mechanism of ICG is explained in the Jablonski diagram shown in **Figure 4.4**. Jablonski diagram shows all the possible absorption and relaxation pathways of two electronic excitations, i.e., S_1 and S_2 state, respectively. Particularly, if ICG was excited by 680 nm and 400 nm, the transition of electrons from S_0 to S_1 and S_2 state occurs, respectively. It is important to note that, when ICG molecules are excited by 400 nm, the possible emissions can occur either by the direct transition from S_2 ➔ S_0 state or by first undergoing internal conversion (non-radiative) from S_2 ➔ S_1 state followed by fluorescence emission from S_1 ➔ S_0 state. However, a little is known about the S_2 excitation and its corresponding fluorescence emission by ICG molecules. This peculiar direct transition from S_2 ➔ S_0 state causing fluorescence emission of ICG, which is not a typical phenomenon and has never been discussed for biomedical applications, especially for two-photon imaging.

4.2.1.3 Lifetime Measurement

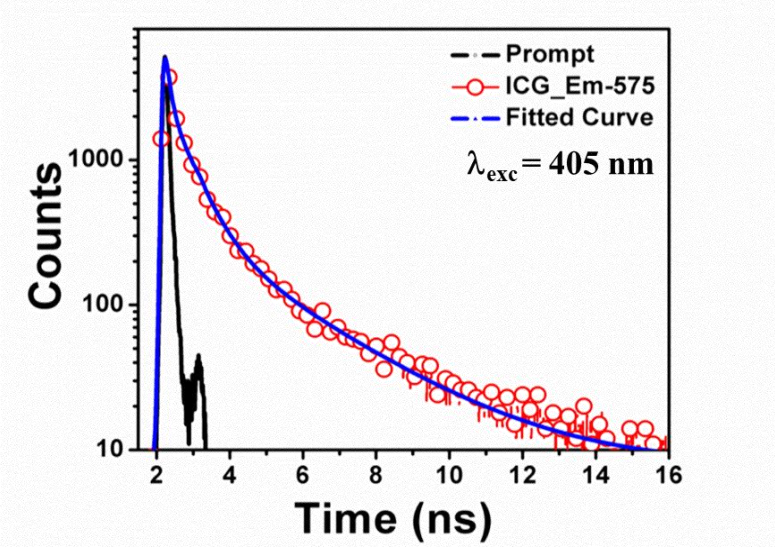

Figure 4.5 Lifetime measurement of the ICG S_2 state.

The fluorescence lifetimes of the S_2 state was calculated from TCSPC. For measurement, a laser of 405 nm was used. The data analysis was done using IBH DAS-6 decay analysis software, and the $\chi 2$ test was used to evaluate the goodness of the fitting. The fluorescence lifetime of S_2 states of ICG was estimated upon excitation at ~405 nm, which was found to be 209 picoseconds (ps), as shown in **Figure 4.5**.

4.2.1.4 Nonlinear Spectroscopy

The aqueous solution of the ICG was irradiated with 790 nm wavelength of a femtosecond laser, which is nearly two times of visible absorption peak of ICG (~400 nm). The fluorescence emission was recorded between 412 – 620 nm. **Figure 4.6(a)** shows, an emission peak at ~556 nm was observed after 790 nm excitation, which resembles the emission peak after single-photon S_2 ➔ S_0 state transition. Also, the fluorescence intensity of ICG was plotted as a function of the femtosecond laser power, as shown in **Figure 4.6(b)**. The log-log plot of fluorescence intensity as a function of the femtosecond laser power at 575 nm exhibits a slope of 2.02, indicating nonlinear 2P excitation of ICG. The nonlinear excitation was described here with the help of the Jablonski diagram showing its working mechanism. Following absorption of 790 nm photons, which excites

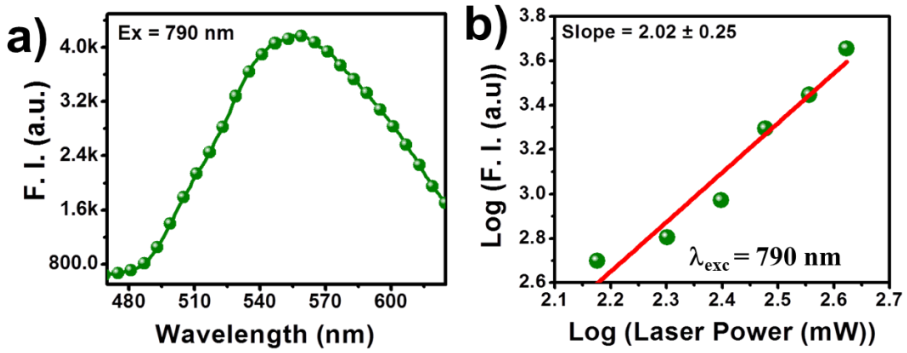

Figure 4.6 Nonlinear excitation spectra of aqueous ICG (a) fluorescence emission collected from 470 nm to 625 nm after multiphoton excitation by 790 nm femtosecond laser (b) fluorescence emission intensity versus femtosecond laser power.

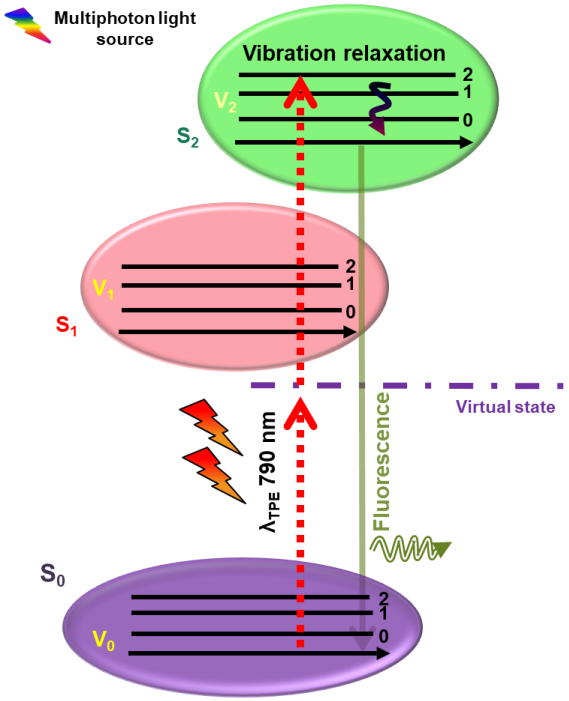

Figure 4.7 Jablonski diagram showing nonlinear excitation working mechanism of the ICG.

electrons of ICG from S_0 ➔ S_2 state, as shown in **Figure 4.7**. This excitation is followed by the direct relaxation of the electrons from S_2 ➔ S_0 state, giving fluorescence emission with the peak intensity at ~575 nm. However, some of these electrons could also follow S_2 ➔ S_1 state transition via internal conversion, but due to instrument limitation, the S_1 ➔ S_0 state transition could not be recorded.

4.2.1.5 Two-photon Bioimaging

The presence of an absorption peak of ICG at 400 nm could excite ICG to the S_2 state, but till now, no report is available, which shows ICG application for multiphoton bioimaging. However, Yang Pu *et al.* reported that ICG could be excited S_2 state by absorbing two-photons of ~800 nm wavelength, but they did not report the direct transition from S_2 ➔ S_0 state causing fluorescence emission.[7, 8] They observed fluorescence emission only from S_1 ➔ S_0 state at ~695 nm after population transfer from S_2 ➔ S_1 state via interconversion (non-radiative relaxation). For the first time, in this thesis, it has been

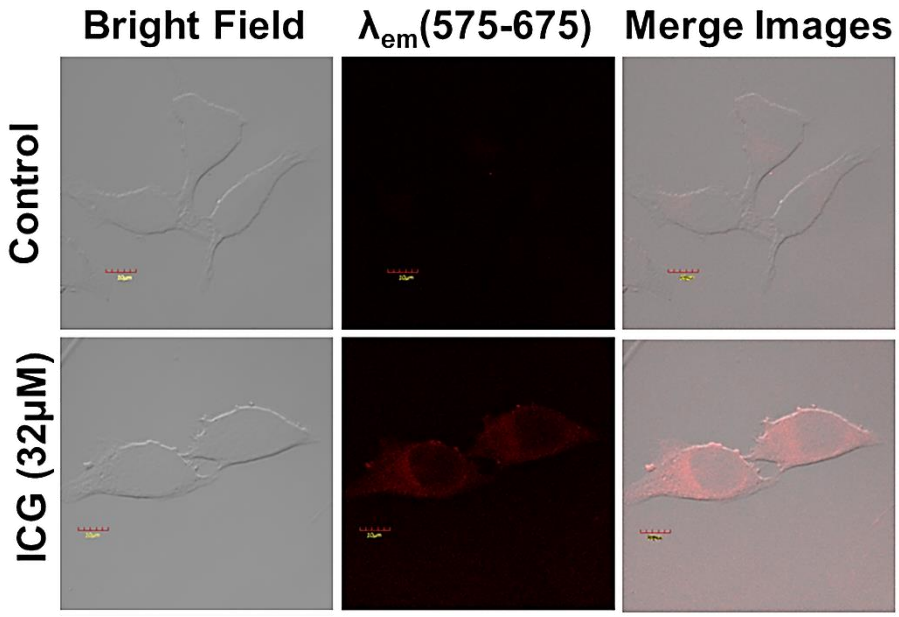

Figure 4.8 Confocal images of HeLa cells incubated with ICG showing emission while excited at 559 nm. (scale bar = 10 μm).

reported that this newly discovered direct S_2 ➔ S_0 state transition property of ICG could be used for a multiphoton biomedical imaging application. **Figure 4.8** shows single-photon confocal fluorescence images of ICG incubated HeLa cells, along with bright field and merged images of the cells. According to the results obtained, ICG incubated cells display fluorescence emission due to direct emission from the S_2 state upon excitation by 559 nm wavelength. These results confirm direct fluorescence emission from S_2 state upon single-photon excitation of ICG. Further, the wavelength dependence of the 2P excitation property of ICG was studied.

For the imaging, ICG treated HeLa cells were excited by femtosecond laser with varying wavelength from 740 nm to 860 nm. **Figure 4.9** shows the fluorescence images (due to direct S_2 state emission) of HeLa cells upon 2P excitation at different wavelengths from 740 nm to 860 nm. Emitted fluorescence due to direct S_2 ➔ S_0 state transition was collected in the emission window from 575 to 630 nm, where non-descanned detectors (NDD) were used to detect the emission. As observed from images, the 790 nm wavelength excitation

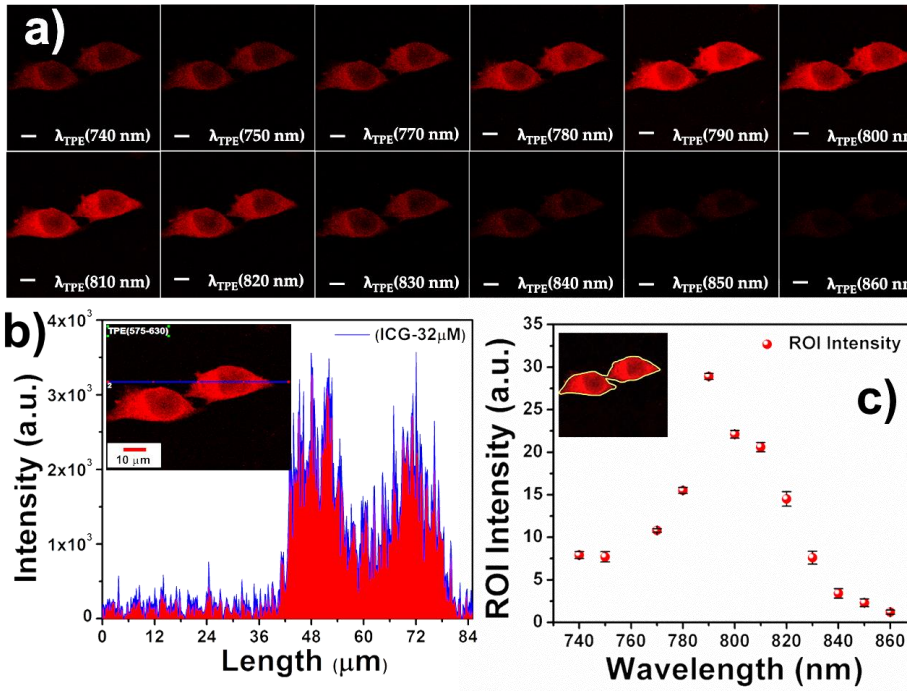

Figure 4.9 Two-photon (2P) imaging of ICG incubated HeLa (a) wavelength dependence excitation from 740 nm to 860 nm; where the scale bar is 10 μm. (b) line intensity of 2P image of HeLa cell (c) Fluorescence intensity versus wavelength plot.

gives the most intense emission, and this wavelength is approximately double of the ~393 nm (the peak wavelength of the absorption band). In addition, the line intensity profile of the 2P images was measured, as shown in **Figure 4.9(b)**. **Figure 4.9(c)** shows the direct S_2 state fluorescence intensity variation of HeLa cells at different excitation wavelengths calculated using IMAGE J, suggesting that 790 nm excitation shows the maximum emission from the cells. Overall, our result suggests that ICG gets excited to the S_2 state after simultaneous absorption of the 2P of ~790 nm wavelength. This property of ICG would further help in probing deeply buried inhomogeneity in the biological tissues, thereby making a revolutionary change in the 2P fluorescence microscopy. Conclusively, in this section, the biomedical imaging application of unexplored direct fluorescence emission from S_2 ➔ S_0 state transition at ~572 nm following 2P absorption has been demonstrated for the first-ever. This work shows that the aqueous ICG

can proficiently emit fluorescence from S_2 state following 2P excitation, which is maximum with the excitation at wavelength ~790 nm. This interesting optical property of ICG makes it a biocompatible exogenous contrast agent for 2PFM in clinical and preclinical applications.

4.2.2 ICG as a Three-photon (3P) Imaging Probe for Multiphoton Bioimaging Application

4.2.2.1 Absorption Spectroscopy

As discussed earlier that apart from the well-known NIR excitation peak at 780 nm, ICG also has peaked at 400 nm and 230 nm. The application and origin of the visible wavelength peak have been discussed in the previous section. Here, for the first time, the application and origin of an unexplored peak at 230 nm will be discussed in this section. For better understanding, each component of the ICG has been highlighted in **Figure 4.10(a).** The molecular structure of the ICG is a combination of the donor (D) – acceptor (A) system, where D is an electron donor (N+) and A, is electron acceptor (N) in polymethine Π-electron system.[9] In addition, at the end of the N atoms, two indolenine groups are present.

The measured absorption spectrum of ICG is shown in **Figure 4.10(b)**, where the whole absorption spectrum is divided into three

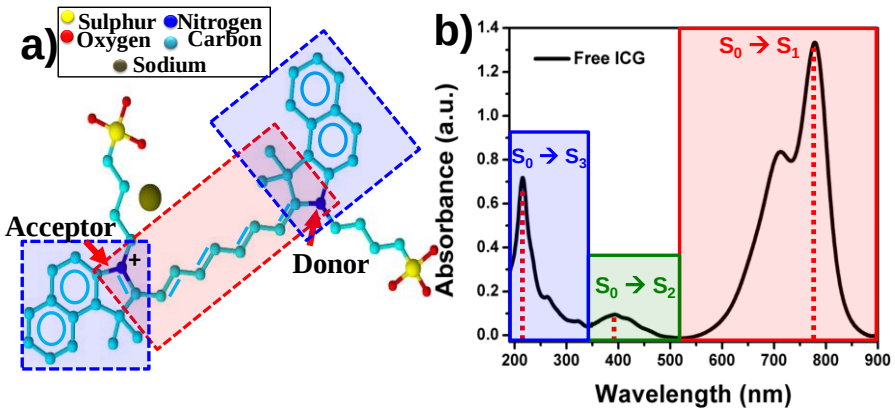

Figure 4.10 ICG (a) molecular structure of the ICG (b) absorption spectrum.

different regions. The major absorption peak of ICG at ~780 nm is attributed to the transition of electrons between S_0 ➔ S_1 states and is due to the transfer of polymethine chain π-electrons between two nitrogen atoms (shaded region by light pink).[9] In addition to this transition, the absorption at ~400 nm excited ICG electrons to the S_0 ➔ S_2 state. Moreover, the presence of higher energy level transitions is also observed, but their origin has never been investigated. At higher energy, the absorption spectrum shows peak maxima at ~230 nm, which is, therefore, excite ICG electrons from S_0 ➔ S_3 states. Moreover, due to the presence of this peak at ~230, ICG could also be used as a UV active biocompatible chromophore for various applications.

4.2.2.2 Fluorescence Emission and Lifetime Measurement

The fluorescence emission spectra of ICG were collected upon

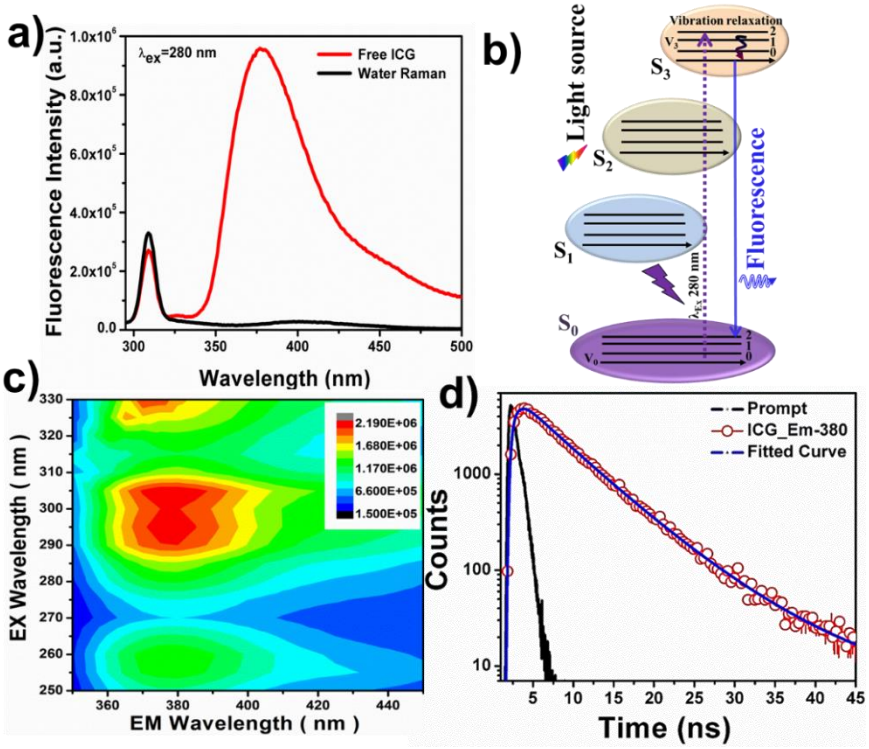

Figure 4.11 ICG spectroscopic studies (a) fluorescence emission (b) Jablonski diagram (c) EEM contour plot for S_3 state (d) TCSPC measurement.

excitation at ~280 nm, which gives rise to a distinct fluorescence emission peak, as shown in **Figure 4.11(a)**. Along with the emission at ~810 nm and ~575 nm after respective excitation, when ICG gives emission at 380 nm after excitation at ~280 nm. **Figure 4.11(b)** shows that the excitation at 280 nm results in the transition of the electrons from S_0 ➔ S_3 state. Following excitation ICG gives emission at 380 nm is due to the transition of electrons from S_3 ➔ S_0 state. Additionally, the EEM contour plots were also recorded to find all possible combinations of excitation and emission wavelengths for all possible transitions of the ICG for S_3 state. As shown in **Figure 4.11(c)**, the S_3 state transition of ICG has excitation and emission maxima at ~300/380 nm, respectively. The fluorescence lifetimes of the S_3 state transition was calculated from TCSPC. For lifetime measurement, a picosecond light-emitting diode (LED) of 279 nm was used.

The data analysis was done using IBH DAS-6 decay analysis software, and the $\chi 2$ test was used to evaluate the goodness of the fitting. The fluorescence lifetime of the S_3 state was found to be 5.7

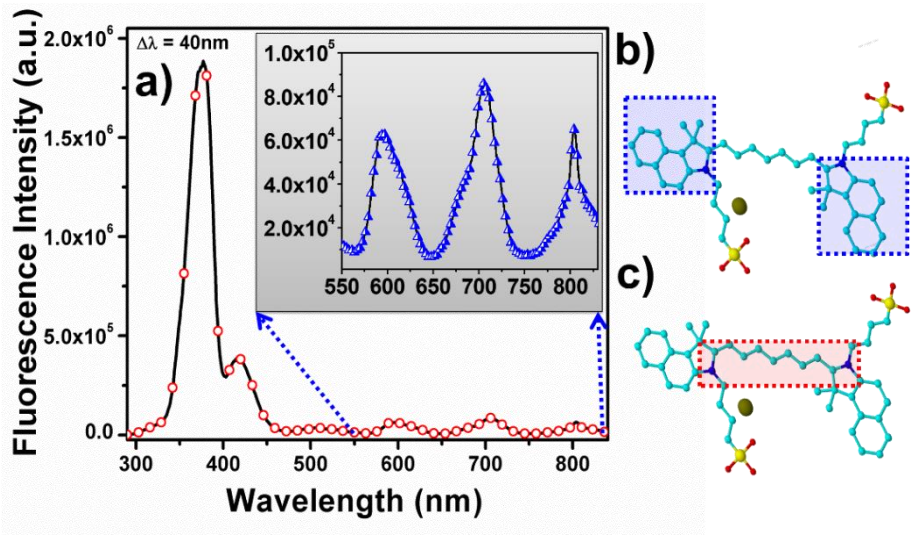

Figure 4.12 The synchronous scan spectrum of the ICG and its components (a) synchronous scan spectrum of the ICG inset: zoom of the spectra from 500 to 850 nm. (b, and c) showing plausible components responsible for the emission in the ICG molecules.

nanoseconds upon 279 nm excitation, as shown in **Figure 4.11(d)**. For these lifetime measurements, the fitting parameter χ^2 was $\leq$ 1.2. This optical property of ICG could be used in various medical, optical, and electronics applications.[10–13]

To further understand the origin of different emissions from ICG, the synchronous fluorescence scan was performed. The synchronous fluorescence scan gives an idea about the number of components present in the molecule, which are responsible for the multicolor emissions. As shown in **Figure 4.12**, four major peaks were reported with a central peak at 380 nm with a shoulder peak at ~420 nm, ~600 nm, ~710 nm, and 800 nm. The peak at ~380 could be due to the presence of two indolenine groups at both ends of the ICG molecular structure (blue shaded region, as shown in **Figure 4.12(b))**.[14, 15] Further, the shoulder peak at 420 nm is due to vibrionic relaxation from S_3 ➔ S_0 state. Moreover, the peak at ~600 nm, is possibly due to the movement of electrons in the green shaded region as shown in **Figure 4.12(c)** and the peaks at 710 nm and 800 nm is due to the movement of electrons of polymethine chain π-electrons between two nitrogen atoms shaded in Figure S1(d). This result confirms the presence of three major components in the ICG, which are mainly responsible for multicolor emission. This result confirms the origin of the emission due to the presence of three different components in the ICG molecule and from different excited singlet states.

4.2.2.3 Nonlinear Fluorescence Spectroscopy

The nonlinear excitation measurement of the ICG molecules has been achieved by a femtosecond laser. The aqueous solution of the ICG was irradiated with 790 nm wavelength of a femtosecond laser, which is nearly three times of UV absorption peak of ICG (~260 nm). Following absorption of ~790 nm photons, ICG gives emission at ~412 nm, as shown in **Figure 4.13(a)**. This emission range resembles with the emission coming after the transitions of ICG electrons from S_3 ➔

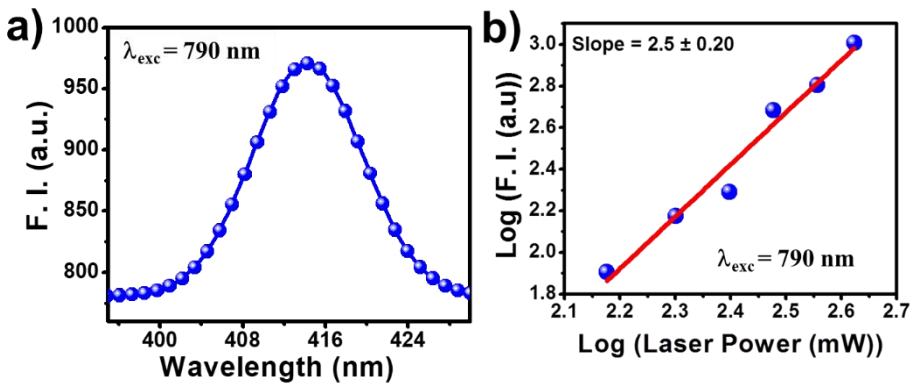

Figure 4.13 Multiphoton excitation spectra of aqueous ICG (a) fluorescence emission collected from 395 nm to 430 nm after 790 nm excitation by femtosecond laser (b) fluorescence emission intensity versus femtosecond laser power.

S_0 state suggesting the nonlinear process has occurred. Furthermore, the fluorescence intensity of ICG was also plotted as a function of the femtosecond laser power. **Figure 4.13(b)** shows the log-log plots of fluorescence intensity as a function of the femtosecond laser power at 412 nm. The log-log plot of the peak at ~412 nm exhibits slope 2.5, indicating nonlinear 3P excitation of the ICG.

4.2.2.4 ICG as a 3P Bioimaging Agent

To the best of our knowledge, the emission at 380 nm of ICG has never been reported, nor utilized for any application in the past. Here, ICG nonlinear excitation from S_0 ➔ S_3 state and its direct emission from S_3 ➔ S_0 state has been used for the 3P bioimaging probe for diagnosis. The 3P excitation to the S_3 state has never been reported and is expected to achieve a higher spatial resolution than ICG mediated 2P bioimaging.[16] For imaging, cervical cancer (HeLa) cells were used. ICG treated HeLa cells were excited by a range of wavelengths from 700 – 900 nm femtosecond laser and the fluorescence images were collected in the window of 420 - 460 nm corresponding to S_3 ➔ S_0 transition (3P). The wavelength-dependent fluorescence emission from HeLa cells was collected for 3P excitation. **Figure 4.14(a-i)** shows the

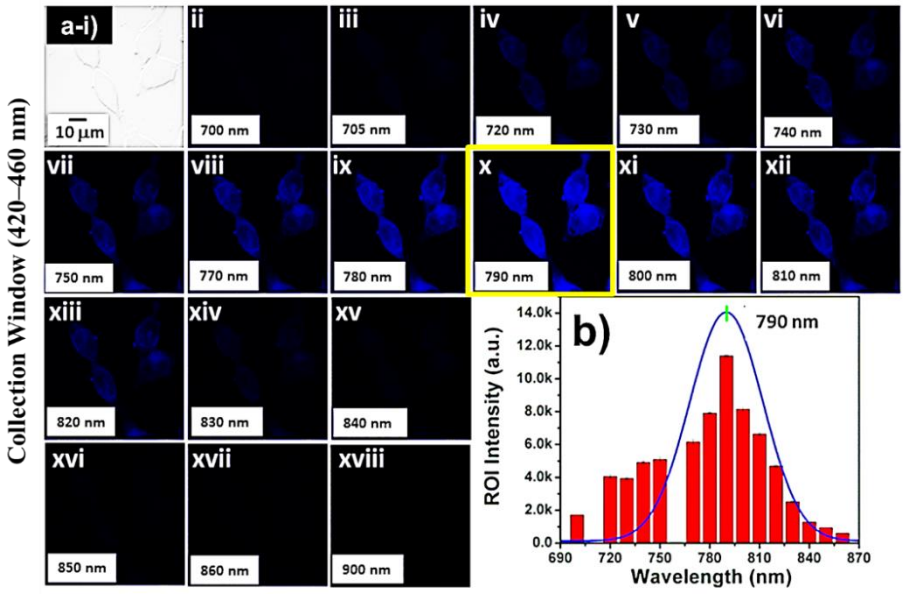

Figure 4.14 Multiphoton imaging of the HeLa cells (a-i) bright field of hela cells (a (ii-xviii) shows the emission of ICG when excited by absorption of 3P from femtosecond laser (b) the fluorescence intensity versus wavelength of excitation.

bright field image of the HeLa cells, and **Figure 4.14(a (ii-xviii)) shows** fluorescence emission images after the respective excitation. The fluorescence intensity versus laser wavelength plot is shown in **Figure 4.14(b)**, which indicates that at 790 nm, excitation highest fluorescence emission is collected. These findings give an insight into the nonlinear excitation property of ICG, which makes it a biocompatible FDA approved exogenous contrast agent for 3P bioimaging.

4.3 Conclusion

Conclusively, this chapter discussed the newly found absorption properties of ICG. The absorption bands at ~400 nm and ~230 nm are due to the transition of electrons from S_0 state to S_2 and S_3 states, respectively. In addition to single-photon excitation to S_2 and S_3 states, electrons can also be excited to these higher excited states in a nonlinear fashion. Additionally, it has been demonstrated that the application of ICG as a novel S_2 state mediated 2P bioimaging, and S_3

state mediated 3P excitation probe for the multiphoton bioimaging. These results could help in reducing the photobleaching and photon-induced toxicity to the cells while probing the deeper inhomogeneity with superior SNR. We believe that these newly identified optical properties of ICG would open doors to new possibilities to utilize ICG in various fields.

4.4 Reference

1. Piston DW (1999) Imaging living cells and tissues by two-photon excitation microscopy. Trends Cell Biol 9:66–69. https://doi.org/10.1016/S0962-8924(98)01432-9

2. Denk W, Strickler JH, Webb WW (1990) Two-photon laser scanning fluorescence microscopy. Science (80) 248:73–76. https://doi.org/10.1126/science.2321027

3. So PTC, Dong CY, Masters BR, Berland KM (2000) Two-photon excitation fluorescence microscopy. Annu Rev Biomed Eng 02:399–429. https://doi.org/10.1146/annurev.bioeng.2.1.399

4. Soper SA, Mattingly QL (1994) Steady-State and Picosecond Laser Flourescence Studies of Nonradioactive Pathways in Tricarbocyanine Dyes: Implications to the Design of Near-{IR} Flourochromes with High Flourescence Efficiencies. J Am Chem Soc 116:3744–3752. https://doi.org/10.1021/ja00088a010

5. Beer M, Longuet-Higgins HC (1955) Anomalous light emission of azulene. J Chem Phys 23:1390–1391. https://doi.org/10.1063/1.1742314

6. Kasha M (1950) Characterization of Electronic Transitions in Complex Molecules. Discuss Faraday Soc 9:14–19. https://doi.org/10.1039/df9500900014

7. Pu Y, Shi L, Pratavieira S, Alfano RR (2014) Enhancing the

depth of tissue microscope imaging using two-photon excitation of the second singlet state of fluorescent agents. Proc SPIE 8940:894017(1)-894017(7). https://doi.org/10.1117/12.2035334

8. Pu Y, Shi L, Pratavieira S, Alfano RR (2013) Two-photon excitation microscopy using the second singlet state of fluorescent agents within the “tissue optical window.” J Appl Phys 114:153102(1–4). https://doi.org/10.1063/1.4825319

9. Karton-Lifshin N, Albertazzi L, Bendikov M, *et al.* (2012) “Donor-Two-Acceptor” dye design: A distinct gateway to NIR fluorescence. J Am Chem Soc 134:20412–20420. https://doi.org/10.1021/ja308124q

10. Freitag M, Teuscher J, Saygili Y, *et al.* (2017) Dye-sensitized solar cells for efficient power generation under ambient lighting. Nat Photonics 11:372–378. https://doi.org/10.1038/nphoton.2017.60

11. Spitler MT, Parkinson BA (2009) Dye sensitization of single crystal semiconductor electrodes. Acc Chem Res 42:2017–2029. https://doi.org/10.1021/ar900232m

12. El-Shishtawy RM (2009) Functional dyes, and some hi-tech applications. Int J Photoenergy 2009:. https://doi.org/10.1155/2009/434897

13. Wang J, Lin W, Li W (2013) Three-channel fluorescent sensing via organic white light-emitting dyes for detection of hydrogen sulfide in living cells. Biomaterials 34:7429–7436. https://doi.org/10.1016/j.biomaterials.2013.06.013

14. Aaron JJ, Tine A, Villiers C, *et al.* (1983) Electronic absorption and fluorescence spectra of indole derivatives. Quantitative treatment of the substituent effects and a theoretical study. CroatChemActa 56:157–168

15. Borrelli R, Ellena S, Barolo C (2014) Theoretical and experimental determination of the absorption and emission spectra of a prototypical indolenine-based squaraine dye. Phys Chem Chem Phys 16:2390–2398. https://doi.org/10.1039/c3cp54298j

16. Hell SW, Bahlmann K, Schrader M, *et al.* (1996) Three-photon excitation in fluorescence microscopy. J Biomed Opt 1:71. https://doi.org/10.1117/12.229062

Chapter 5

Effect of Nanoencapsulation of ICG on Multiphoton Bioimaging

5.1 Introduction

As shown in chapter 3, the nanoencapsulation of ICG overcomes the limitations of free ICG for NIR bioimaging. The ICG PLL NPs were found to be safe for the cells. However, they had a mean diameter of ~225 nm. It is generally believed that sub 100 nm diameter particles have a higher probability of targeting the cancerous tissues via passive targeting mechanism exploiting the enhanced permeability and retention (EPR) effect. Hence, in this chapter, the fabrication of arginine based biocompatible sub 100 nm diameter nanoparticles for the encapsulation of ICG is introduced.

Poly-l-arginine (PLA) is a homopeptide of L-arginine, which has been used in medical applications for many centuries due to its cellular penetrating properties.[1–7] It is a semi-essential amino-acid with various roles in cell metabolism, such as wound healing, protein synthesis, and shows antimicrobial and antitumor activity.[8–13] In particular, owing to the favourable properties of arginine, NPs comprised of PLA gained considerable interest in the delivery of small molecules. [14–16] ICG PLA NPs are expected to improve the optical and aqueous stability of ICG and cellular delivery.

The fabrication of ICG loaded PLA NPs (ICG PLA NPs) its effect on optical properties and multiphoton imaging ability are studied in this

This chapter is largely taken from ***Kumari, A.,*** *Kumari, K., and Gupta, S. "The effect of nanoencapsulation of ICG on two-photon bioimaging" RSC Adv., 2019; 9: 18703-18712.*

chapter. The fabrication of these NPs was done via a similar two-step self-assembly method described earlier in chapter 3. The in-vitro cellular study suggests that both free and nanoencapsulated ICG get endocytosed within the cells. In comparison with free ICG, ICG PLA NPs has been shown significant enhancement in cellular delivery. Additionally, nanoencapsulated ICG treated cells show enhanced contrast for 2P bioimaging in comparison with free ICG. In conclusion, biocompatible and biodegradable ICG PLA NPs could be used for improved 2P bioimaging.

5.2 Result and Discussions

Effect of ICG nanoencapsulation on 2P fluorescence bioimaging is studied and discussed in this chapter. For this purpose, we have used PLA, a biocompatible and biodegradable cationic peptide, to encapsulate ICG.

5.2.1 Fabrication of the ICG PLA NPs

The ICG PLA NPs were fabricated through a simple two-step self-assembly process in an aqueous solution without any organic solvent. A complete green chemistry-based fabrication process was used for this synthesis. The schematic representation of the fabrication process is illustrated in **Figure 5.1**. For fabrication, an aqueous solution of PLA was mixed with the salt solution followed by the addition of free ICG, and this results in the initiation of the self-assembly process and the fabrication of

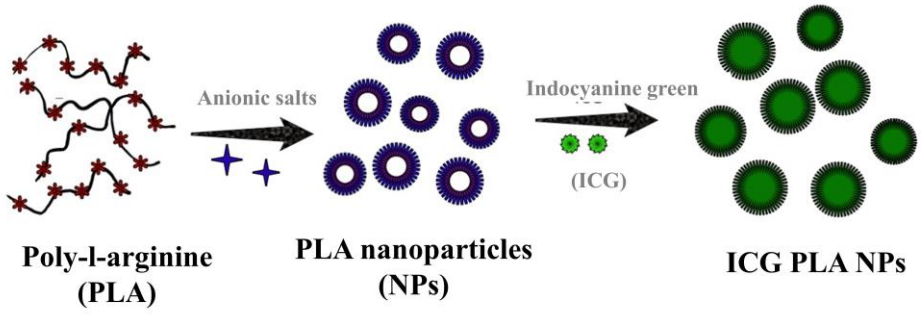

Figure 5.1 Schematic representation of the ICG PLA NPs fabrication.

ICG PLA NPs. Briefly, 10 µL of PLA solution (2 mg/mL) was gently mixed with the 4 µL of the EDTA salts (0.1 M) for 20 seconds. Immediately after the mixing, the clear solution turns turbid, which indicates the initiation of the nucleation process. Followed by the addition of the 250 µL of the ICG (645 µM) to the colloidal solution. Then the 1 mL of DI water was added to the suspension and aged for 1 hour to form ICG PLA NPs. The systematic mixing of these precursors results in the fabrication of the ICG PLA NPs.

5.2.2 Biophysical Characterization of the ICG PLA NPs

The morphological characterization of these NPs was done via FESEM and DLS, as shown in **Figure 5.2(a)**. Diameter distribution of the lyophilized ICG PLA NPs, as determined by analysis of FESEM images, is shown in **Figure 5.2(b)**. The average particle diameter was ~61 ± 20 nm having a spherical shape. Similarly, the DLS study shows that ICG PLA NPs have a mean hydrodynamic diameter of ~154 ± 20 nm shown in **Figure 5.3(a).** The polydispersity index (PDI) was found to be 0.23, which suggests that these NPs were monodisperse in aqueous solution. The difference between the mean diameter in the dry state (SEM measurements) and aqueous state (DLS measurements) could be due to the

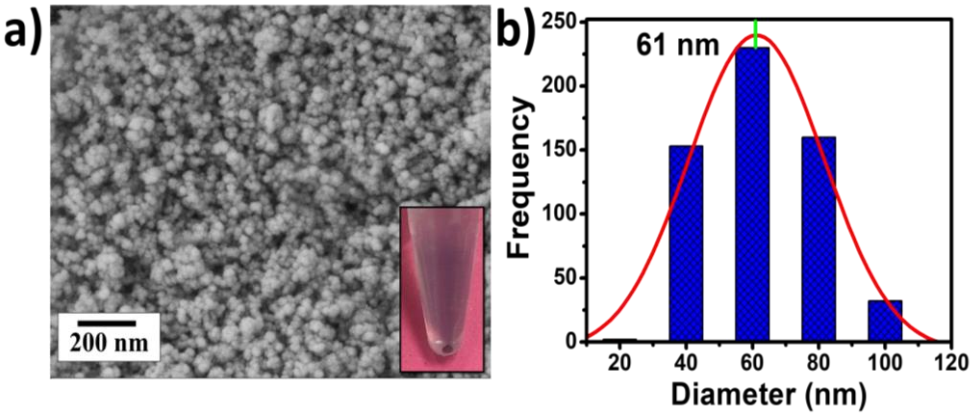

Figure 5.2 Characterization of the ICG PLA NPs (a) FESEM images; Inset: a pellet of the NPs (b) diameter frequency distribution of the particles.

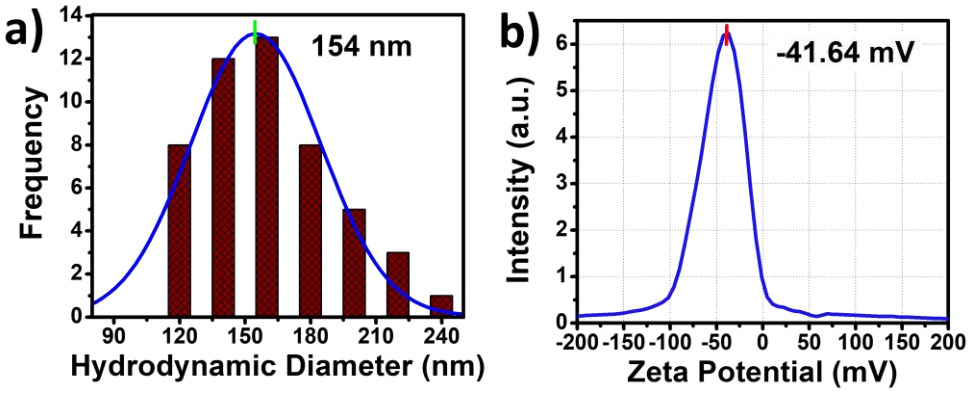

Figure 5.3 Characterization of the ICG PLA NPs (a) hydrodynamic diameter of the NPs (b) zeta potential of the NPs.

shrinkage of NPs in the dry state. Additionally, the zeta (ζ) potential of these NPs was found to be -41.64 mV(**Figure 5.3(b)**), which shows the stability of the NPs in the aqueous solution, and ICG PLA NPs will not aggregate in the aqueous environment.

5.2.3 Spectroscopic Characterization of the Free ICG and ICG PLA NPs

The effect of nanoencapsulation of the ICG on its optical properties is studied and shown in **Figure 5.4**. The free ICG has two major absorption peaks at 780 nm with a shoulder peak at 710 nm and 400 nm, respectively, as shown in **Figure 5.4(a)**. All possible excitation and emission transition were shown using the Jablonski diagram depicting the possible excitation and emission from the ground to higher excited states and vice versa. The presence of an absorption peak at 780 nm and 400 nm leads to the transition of ICG electrons from S_0 ➔ S_1 and S_0 ➔ S_2 states, respectively. Following excitation, ICG releases its energy in the form of the fluorescence emission via the transition of electrons from S_1 ➔ S_0 (800 nm) and S_2 ➔ S_0 (565 nm) state, as shown in the Jablonski diagram. Due to the S_2 ➔ S_0 state transition, ICG could be one of the molecules that violate Kasha's rule.

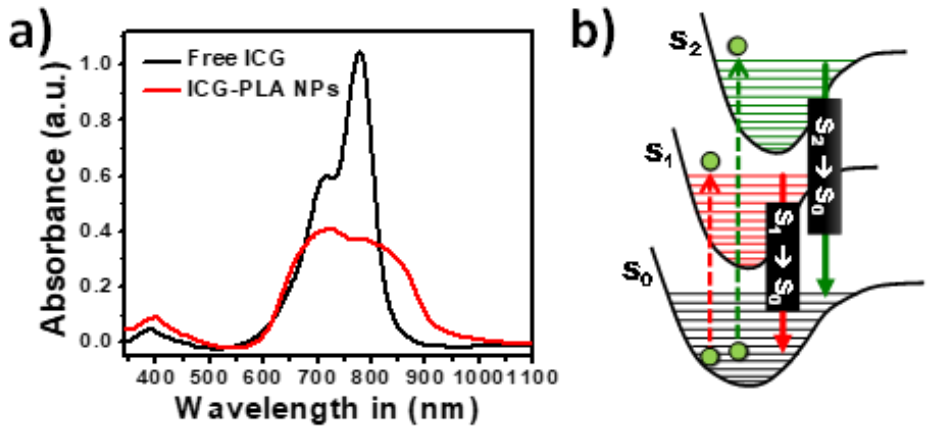

Figure 5.4 Spectroscopic analysis of the free ICG and ICG PLA NPs (a) Absorption spectra (b) Jablonski diagram showing all possible transitions.

In comparison with the absorption spectrum of free ICG, the nanoencapsulated ICG showed significant suppression of the 780 nm peak with a line broadening without any shift in peak position, as shown in **Figure 5.4(a).** However, a minor increase in the absorption at 400 nm is observed in ICG PLA NPs, which could be highly advantageous for 2P excitation to the S_2 state. Similarly, the fluorescence emission of free and nanoencapsulated ICG is measured. ICG emits at 800 nm after 680 nm excitation, as shown in **Figure 5.5(a),** this transition is attributed to the transition of electrons from S_1 ➔ S_0 state. In comparison to the free ICG, the nanoencapsulated ICG shows a significant reduction in the

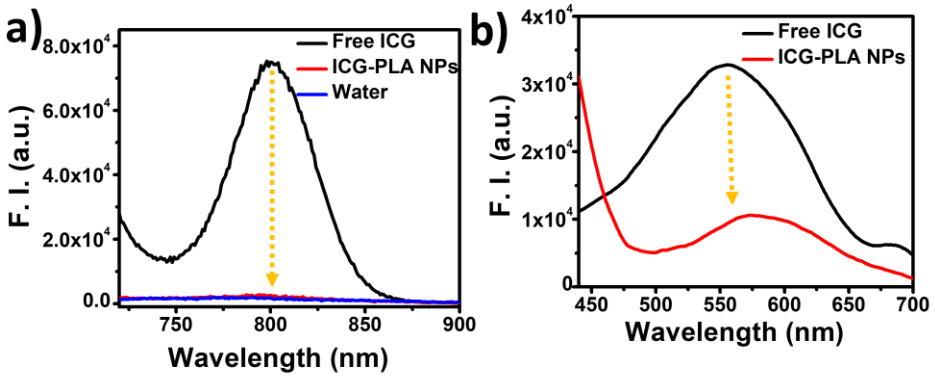

Figure 5.5 Spectroscopic analysis of the free ICG and ICG PLA NPs (a) emission spectra after 680 nm excitation (b) emission spectra after 420 nm excitation.

fluorescence emission peak at 800 nm without any peak shift. Also, when ICG was excited by 420 nm it gives emission at ~565 nm as shown in **Figure 5.5(b),** this transition is due to the transition of electrons from S_2 ➔ S_0 state. In comparison with free ICG, the nanoencapsulated ICG shows a reduction in emission peak intensity with a shift of the peak towards red wavelength, as shown in **Figure 5.5(b)**. It has been shown in the past that ICG emission gets quenched when ICG is inbounded state, [17] due to energy resonance transfer among the bound fluorochromes. Similarly, here both the emission from ICG gets quenched during nanoencapsulation of the ICG in the cationic polymer. However, these spectroscopic results suggest that the fluorescence emission due to S_2 ➔ S_0 state transition does not get much affected after the nanoencapsulation of ICG. Therefore, it might be used as an exogenous contrast agent in 2P bioimaging.

To further confirm the findings of steady-state fluorescence emission, the time-resolved fluorescence measurements on free and nanoencapsulated ICG were carried out. The fluorescence lifetime measurements of the free and nanoencapsulated ICG were measured upon 405 nm excitation. The fluorescence lifetimes of free and nanoencapsulated ICG for S_2 state were found to be 209.4 and 92 ps,

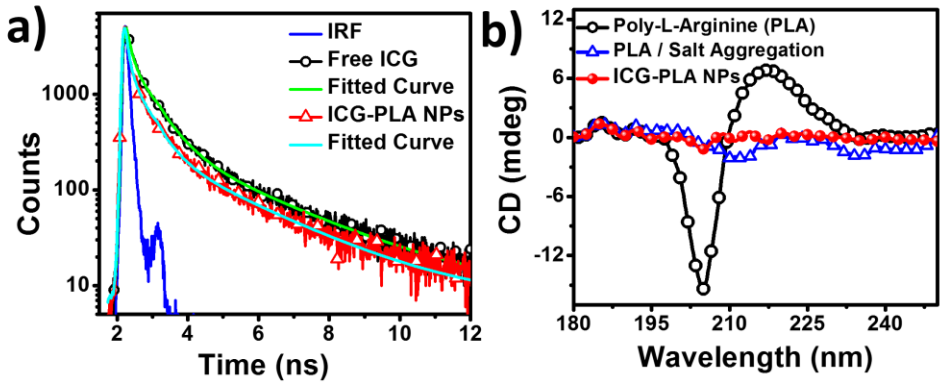

Figure 5.6 Time-resolved studies and CD analysis of the free ICG and ICG PLA NPs (a) TCSPC of the free ICG and ICG PLA NPs at 575 nm upon 405 nm excitation (b) CD spectra of the PLA, PLA/salt and ICG PLA NPs.

respectively, as shown in **Figure 5.6(a).** These results further confirm the quenching of the fluorescence emission of ICG in nanoencapsulated form. The fitting parameter χ^2 was ≤ 1.3 for all the fitting. To further understand the role of ICG during self-assembly of the NPs, CD measurements were carried out. **Figure 5.6(b)** shows the CD spectra of aqueous PLA, PLA and salt aggregates, and ICG PLA NPs. The CD spectra of an aqueous solution of PLA exhibits one negative peak at ~ 204 nm and one positive peak at ~217 nm. This suggests the presence of a random structure for the aqueous solution of PLA homopeptide, as shown in **Figure 5.6(b).** However, the PLA CD spectral alterations due to PLA/salt aggregation is reflected by the changes in the intrinsic CD spectrum of PLA. The peak at ~ 204 nm and ~217 nm got suppress due to the interaction of PLA with salt. Similarly, the PLA/salt aggregates have a small magnitude of two negative peaks at ~212 nm and ~236 nm, which further got suppressed after the addition of ICG. This suggests the complexation of PLA homopeptide largely depends on the amino acid residues, which function as the binding ligands for a small molecule to encapsulate. Initially, the complexation of the PLA is done with the EDTA salt at a fixed molar charge ratio (MCR=9), which results in the complexation between two guanidinium groups and salt. Further, the addition of the ICG in this reaction resulted in the formation of the ICG PLA NPs, which provides more stability to this self-assembled structure, as shown by the red curve in **Figure 5.6(b).** The CD result strongly suggests that the two-guanidinium groups of PLA, act as a ligand, which makes a complex with salt and dye to form stable NPs.

5.2.4 ICG Release, Biosafety and Stability Study of ICG PLA NPs

The nanoencapsulated ICG was shielded from any external factors, which deteriorate its optical properties in free form. However, efficient delivery of ICG to the cellular level is required for improved multiphoton imaging. Here, ICG was nanoencapsulated within salt cross-linked PLA NPs via the

self-assembly method. However, in the nanoencapsulated state, ICG emission was quenched due to energy resonance transfer among the bound fluorochromes and could be regained after enzymatically degradation of the polymer, as shown in **Figure 5.7(a and b)**. The in-vitro ICG release study was done in the presence of a proteolytic enzyme at 37 ℃ using a dispersion method. [18] The sample was prepared and aliquoted in 5 tubes and then centrifuged to collect the NPs. A commonly used protease enzyme trypsin was used to study the ICG release from ICG PLA NPs. The freshly prepared NPs were incubated 1 mL 0f 250 µg/mL of trypsin at 37 ℃ for 24 hours. At different time intervals, the samples were centrifuged, and the absorbance of the supernatant was measured at 778

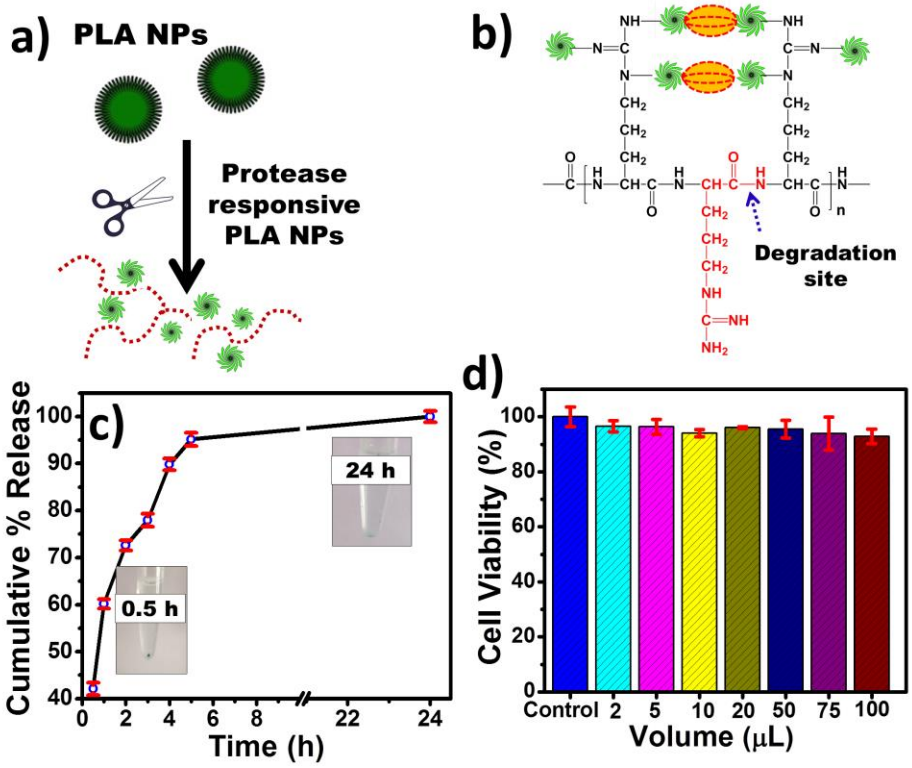

Figure 5.7 Release and cellular toxicity of the ICG PLA NPs. (a) schematic showing the principle of the ICG PLA NPs as a protease responsive NPs (b) mechanism of the fluorescence activation (c) in-vitro release study over 24 hours (d) cellular viability of the ICG PLA NPs over the range.

nm using a UV-Vis-NIR spectrophotometer to quantify ICG release. The NPs were then placed back into the same incubation conditions. The release of ICG form ICG PLA NPs was monitored for over 24 hours. The amount of released ICG was calculated using **Equation 5.1.**

$$\text{Cumulative \% release} = \left\{\frac{\text{Absorption of supernatant after every time point}}{\text{The total concentration of ICG used for the synthesis}}\right\} *100 \quad \textbf{Equation 5.1}$$

The amount of released ICG was determined by measuring the intensity of the absorbance (778 nm) using free ICG as the standard. The ICG release experiments were performed in triplicate, and the results presented are the average data over 24 hours. The instant release of 43 % of ICG from ICG PLA NPs was observed upon 30 minutes of incubation. Therefore, these NPs are protease responsive, where fluorescence signal increased due to cleavage of PLA homopeptide on carboxy-terminal in the presence of the protease as depicted in **Figure 5.7(b)**. This results in small fragments of amino-acid residues,[19] salt, and free ICG. However, within 5 hours of trypsin incubation, nearly 94 % of ICG was released following 98 % released after 24 hours of incubation, as shown in **Figure 5.7(c)**. To explore the biomedical application of the nanoencapsulated ICG, the cellular viability of these NPs was tested using MTT assay over the range of concentration. As shown in **Figure 5.7(d),** no significant cytotoxicity was observed even at a very high concentration of these NPs. Hence, this indicates that these NPs are safe and biocompatible nanocarrier for biomedical applications.

5.2.5 Stability Assessment of the Nanoencapsulated and Free ICG

The optical stability of the nanoencapsulated ICG is a vital parameter for bioimaging applications. Here, the optical stability of the free and encapsulated ICG in physiological conditions was monitored. It is well known that the optical properties of ICG are dependent on temperature,

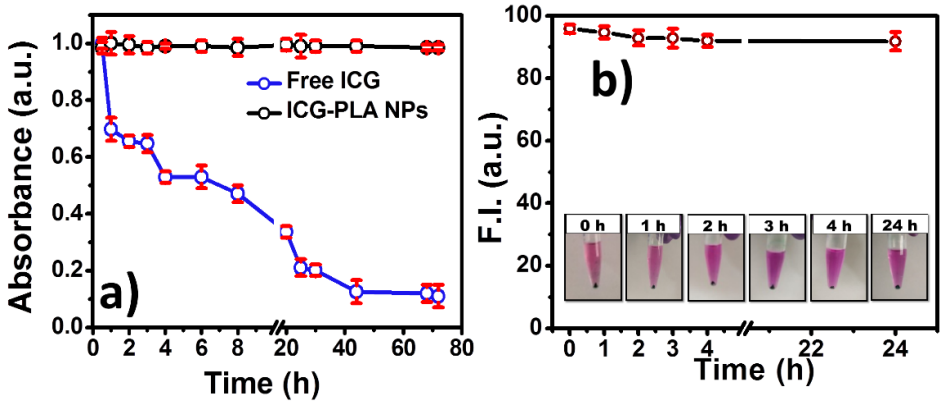

Figure 5.8 Stability of the ICG PLA NPs (a) optical stability at 37 ℃ of ICG PLA NPs and free ICG (b) ICG PLA NPs media stability over 24 hours.

time, and long-term optical exposure. Due to these factors, optical properties degrade gradually. The effect of optical exposure on the optical properties of free and nanoencapsulated ICG over a period of time at physiological temperature was monitored. The free ICG and ICG PLA NPs were incubated at 37 °C for 72 hours in ambient light exposure. As shown in **Figure 5.8(a),** the optical property of ICG PLA NPs was found to be significantly more stable in comparison with the free ICG. The optical property of free ICG started degrading after 30 minutes of the incubation; on the other hand, ICG PLA NPs were stable up to 72 hours, as shown in **Figure 5.8(a).** The stability of ICG PLA NPs in the physiological environment was studied by incubating them in cell culture media for 24 hours at 37 ℃. As shown in **Figure 5.8(b),** ICG PLA NPs were 95 % stable in the physiological condition. According to the results, ICG PLA NPs are stable nanocarriers for ICG delivery in the cells.

5.2.6 Encapsulation Efficiency

To determine the ICG loading efficiency, a batch of ICG-PLA NPs were synthesized and collected via centrifugation. The collected pellet was exposed to dimethyl sulfoxide (DMSO) for the complete disruption of the

NPs, resulting in release free ICG. The encapsulation efficiency of the ICG within ICG PLA NPs was calculated using **Equation 5.2.**

$$EE = \left(\frac{\text{The concentration of ICG after disassembly of NPs}}{\text{The total concentration of ICG used for the synthesis}}\right) * 100 \text{.....Equation 5.2}$$

For calculation, the absorption spectra of disintegrated ICG-PLA NPs were measured at 792 nm as ICG in DMSO shows a peak at 792 nm due to the solvent effect. Further, the ICG concentration within these NPS was calculated by the calibration curve. A total of 56 % of ICG was loaded in one batch of the ICG PLA NPs.

5.2.7 Multiphoton Imaging

The multiphoton imaging ability of the nanoencapsulated ICG was studied after staining the HeLa cells. Previously, our group had reported the nonlinear excitation of free ICG to the S_2 state, followed by its direct relaxation to S_0 state, causing an emission and used for the multiphoton imaging applications.[20] However, the use of the free form of ICG has limitations such as poor photostability and cellular uptake. Herein, ICG PLA NPs were used to overcome the limitations of free ICG, and its nonlinear excitation to the S_2 state followed by emission was reported for 2P bioimaging. These ICG PLA NPs are promising vectors for intracellular drug delivery as they can be taken up by the cells via endocytosis.[21] **Figure 5.9(a)** shows the bright field, and corresponding 2P images of the HeLa cells treated with free ICG and ICG PLA NPs, cells without any treatment were considered as a negative control. The images collected here for 2P ICG emission were due to S_2 ➔ S_0 state transition is shown in the first, and second respectively. However, the first, second, and third rows show the control, free ICG, and ICG PLA NPs treated cells, respectively. As clearly evident by **Figure 5.9(a),** the ICG PLA NPs treated cells showed significantly higher emission in comparison with free ICG treated cells. These results (**Figure 5.9(a))** suggest that ICG PLA NPs are efficiently taken up by the cells in comparison with free ICG. This also indicates that the PLA NPs are highly efficient to deliver

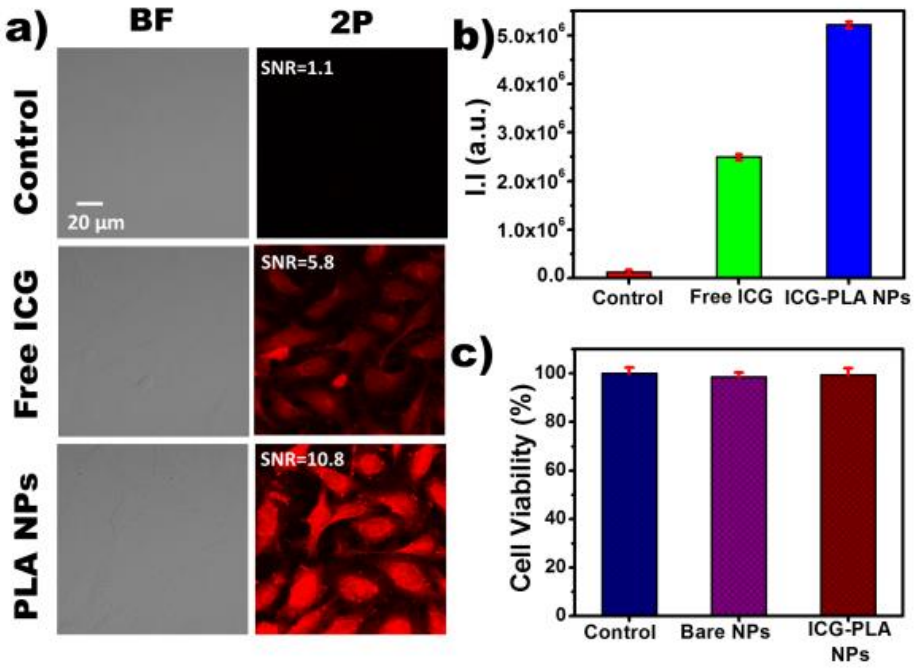

Figure 5.9 Cellular uptake, localization and viability studies (a) Single photon (1P) and 2P imaging (b) cellular viability of the bare and ICG PLA NPs used for the experiment (c) Integral intensity of the 1P and 2P imaging. Where, I.I is integral intensity.

ICG to the cells, and it could be attributed to PLA, which is a known cell-penetrating peptide. Furthermore, for better quantification of the 2P (S_2 ➔ S_0 state) emission, integral fluorescence intensity was calculated using ImageJ and plotted, as shown in **Figure 5.9(b)**. According to the results, the ICG PLA NPs showed considerably higher multiphoton emission than free ICG multiphoton images and corresponding 1P images. Further, nanoencapsulated ICG has nearly five-fold increases in its fluorescence emission in comparison to free ICG for 2P. For bioimaging applications, the biosafety of these nanoparticles was also assessed using cellular viability assay. For cell viability experiments, untreated cells, bare PLA nanoparticle-treated cells, and ICG PLA NPs treated cells were studied. As seen in **Figure 5.9 (b)**, the bare PLA nanoparticle treated, and ICG PLA NPs treated cells show excellent biosafety with more than 98 % cellular viability. These results collectively confirmed the effectiveness of

ICG PLA NPs as a biocompatible and biodegradable exogenous contrast agent for a 2P cellular imaging application.

5.3 Conclusion

We have successfully encapsulated ICG within PLA based nanoparticles, which were used to study the effect of nanoencapsulation on the two-photon imaging ability of ICG. The nanoparticle synthesis was performed by a simple two-step self-assembly process in an aqueous environment without using any organic solvent. It was found that ICG PLA NPs exhibit excellent biosafety and does not show any toxicity to the cells at tested concentrations. The ICG PLA NPs show surprisingly high cellular uptake for two-photon bioimaging. These NPs can be used as a highly efficient and biologically safe exogenous multiphoton contrast agent with remarkably improved photostability in comparison to free ICG.

5.4 References

1. Niu Z, Tedesco E, Benetti F, et al (2017) Rational design of polyarginine nanocapsules intended to help peptides overcoming intestinal barriers. J Control Release 263:4–17. https://doi.org/10.1016/j.jconrel.2017.02.024

2. Vanegas Sáenz JR, Tenkumo T, Kamano Y, et al (2017) Amiloride-enhanced gene transfection of octa-arginine functionalized calcium phosphate nanoparticles. PLoS One 12:1–15. https://doi.org/10.1371/journal.pone.0188347

3. Yamaki T, Uchida M, Kuwahara Y, et al (2013) Effect of poly-L-arginine on intestinal absorption of hydrophilic macromolecules in rats. Biol Pharm Bull 36:496–500. https://doi.org/10.1248/bpb.b12-00974

4. Bygd HC, Akilbekova D, Muñoz A, et al (2015) Poly-l-arginine

based materials as instructive substrates for fibroblast synthesis of collagen. Biomaterials 63:47–57. https://doi.org/10.1016/j.biomaterials.2015.05.045

5. Futaki S (2002) Arginine-rich peptides: potential for intracellular delivery of macromolecules and the mystery of the translocation mechanisms. Int J Pharm 245:1–7

6. Kamiya Y, Yamaki T, Uchida M, et al (2017) Preparation and Evaluation of PEGylated Poly-L-ornithine Complex as a Novel Absorption Enhancer. Biol Pharm Bull 40:205–211. https://doi.org/10.1248/bpb.b16-00781

7. Rothbard JB, Garlington S, Lin Q, et al (2000) Conjugation of arginine oligomers to cyclosporin A facilitates topical delivery and inhibition of inflammation. Nat Med 6:1253–1257. https://doi.org/10.1038/81359

8. Sasidharan S, Bahadur D, Srivastava R (2016) Protein-Poly(amino acid) Nanocore-Shell Mediated Synthesis of Branched Gold Nanostructures for Computed Tomographic Imaging and Photothermal Therapy of Cancer. ACS Appl Mater Interfaces 8:15889–15903. https://doi.org/10.1021/acsami.6b03428

9. Pensado A, Diaz-Corrales FJ, De la Cerda B, et al (2016) Span poly-L-arginine nanoparticles are efficient non-viral vectors for PRPF31 gene delivery: An approach of gene therapy to treat retinitis pigmentosa. Nanomedicine Nanotechnology, Biol Med 12:2251–2260. https://doi.org/10.1016/j.nano.2016.06.007

10. Lind DS (2004) Arginine and Cancer. J Nutr 134:2837S – 2841S

11. Tanvir F, Yaqub A, Tanvir S, Anderson W (2017) Poly-L-arginine Coated Silver Nanoprisms and Their Anti-Bacterial Properties.

Nanomaterials 7:296. https://doi.org/10.3390/nano7100296

12. Kudo S, Nagasaki Y (2015) A novel nitric oxide-based anticancer therapeutics by macrophage-targeted poly(l-arginine)-based nanoparticles. J Control Release 217:256–262. https://doi.org/10.1016/j.jconrel.2015.09.019

13. Sepahi M, Jalal R, Mashreghi M (2017) Antibacterial activity of poly-l-arginine under different conditions. Iran J Microbiol 9:103–111

14. Chiu JZS, Tucker IG, McLeod BJ, McDowell A (2015) Arginine-tagging of polymeric nanoparticles via histidine to improve cellular uptake. Eur J Pharm Biopharm 89:48–55. https://doi.org/10.1016/j.ejpb.2014.11.014

15. Cho HJ, Chong S, Chung SJ, et al (2012) Poly-L-arginine and dextran sulfate-based nanocomplex for Epidermal Growth Factor Receptor (EGFR) siRNA delivery: Its application for head and neck cancer treatment. Pharm Res 29:1007–1019. https://doi.org/10.1007/s11095-011-0642-z

16. Lozano M V., Lollo G, Alonso-Nocelo M, et al (2013) Polyarginine nanocapsules: A new platform for intracellular drug delivery. J Nanoparticle Res 15:. https://doi.org/10.1109/ISIT.2016.7541463

17. Tung CH, Mahmood U, Bredow S, Weissleder R (2000) In vivo imaging of proteolytic enzyme activity using a novel molecular reporter. Cancer Res 60:4953–4958. https://doi.org/10.1158/0008-5472.CAN-06-3315

18. Shazly G, Nawroth T, Langguth P (2008) Comparison of Dialysis and Dispersion Methods for In Vitro Release Determination of Drugs from Multilamellar Liposomes. Dissolution Technol 7–10

19. Zhao XR, Chen YL, Wang L, et al (2016) Highly sensitive fluorescence detection of trypsin based on gold nanoparticle probes. Anal Methods 8:393–400. https://doi.org/10.1039/c5ay02405f

20. Kumari A, Gupta S (2019) Two-photon excitation and direct emission from S2 state of U.S. Food and Drug Administration approved near-infrared dye: Application of anti-Kasha's rule for two-photon fluorescence imaging. J. Biophotonics 12:e201800086

21. Yamaki T, Kamiya Y, Ohtake K, et al (2014) A mechanism enhancing macromolecule transport through paracellular spaces induced by poly-L-arginine: Poly-L-arginine induces the internalization of tight junction proteins via clathrin-mediated endocytosis. Pharm Res 31:2287–2296. https://doi.org/10.1007/s11095-014-1324-4

Chapter 6

Conclusion and Scope of Future Work

6.1 Conclusion

Nanotechnology in the medical field is going to play an important role in the diagnosis and treatment of various diseases. The present thesis provides an in-depth and systematic study of nanoencapsulation of the ICG within essential amino-acids based homopolymers. In particular, PLL, which is a cationic homopolymer of lysine, has been used to reformulate ICG in ICG PLL NPs. The results suggested that the reformulated ICG PLL NPs were more optically stable, biologically safe, and effectively taken up by the cells in comparison with the free form of ICG. Thus the ICG PLL NPs could be used as an exogenous contrast agent for NIR bioimaging.

It must be noted here that ICG, which is the only U. S. FDA approved exogenous contrast agent, has been explored only for its NIR excitation and emission in the literature. Most importantly, in this thesis, for the first time, an effort has been dedicated towards unraveling several exciting properties of ICG, *i.e.*, violation of Kasha's rule, nonlinear excitation to higher-lying excited states and utilization of ICG as an exogenous contrast agent for multiphoton bioimaging. Apart from a well-known NIR absorption peak at ~780 nm, ICG also shows two distinct peaks in the visible and near UV wavelength range. The presence of an absorption peak at ~400 nm excites ICG electrons to the $S_0 \rightarrow S_2$ state. Followed by this excitation, ICG gives emission at 575 nm during relaxation from $S_2 \rightarrow S_0$ state.

Moreover, in this thesis, the nonlinear excitation of ICG

electrons to the S_2 state has been shown and utilized for the S_2 state mediated 2P bioimaging. In addition to that, the presence of the absorption peak in the near UV range at ~230 nm has also been investigated, which excites ICG electrons from S_0 ➔ S_3 state. Followed by this excitation, ICG gives emission at ~380 nm due to the direct transition of electrons from S_3 ➔ S_0 state. The nonlinear excitation to the S_3 state has also been shown and utilized for the S_3 state mediated 3P bioimaging. Thus the measurement of absorption of ICG near the whole optical range from near UV region to NIR region unraveled several new exciting properties, which could be promising for multiphoton imaging.

Despite its application, ICG has several limitations, which might affect its newly found nonlinear optical properties also. These shortcomings might be addressed by nanoencapsulation. So, in order to utilize ICG as a multiphoton exogenous contrast agent, it has been nanoencapsulated within PLA NPs. The effect of nanoencapsulation of the ICG on the optical properties of higher excited states and its application for multiphoton imaging was studied. Results suggest that the significant enhancement of the multiphoton emission was observed from the ICG PLA NPs treated cells in comparison with free ICG treated cells. Finally, it was established that in addition to the NIR imaging application, ICG could also be used as an exogenous contrast agent for preclinical and clinical multiphoton imaging applications for the disease diagnosis. However, the major shortcomings of ICG could be addressed by the nanoencapsulation within polypeptides based nanoparticles, and those were fabricated using green chemistry approach.

6.2 Future Prospects

The carried out research work presented in this thesis has highlighted the nonlinear optical properties of ICG and the importance of nanoencapsulated ICG for NIR and multiphoton bioimaging. This work shows the future potential of ICG to be utilized as a first U. S.

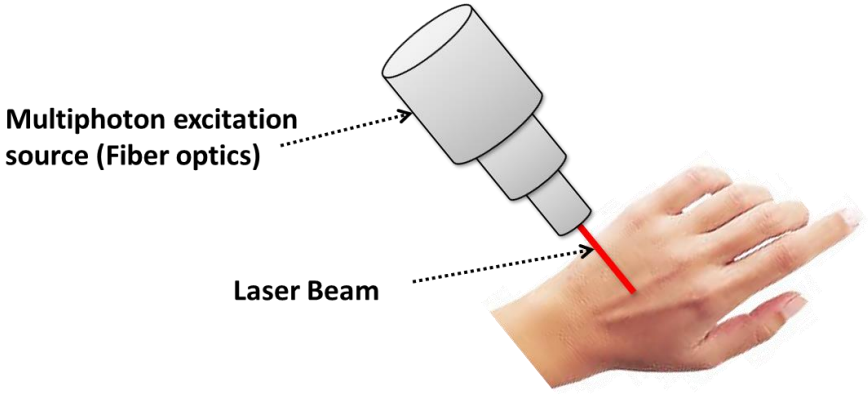

Figure 6.1 Application of ICG as an exogenous contrast agent for multiphoton bioimaging.

FDA approved an exogenous contrast agent for multiphoton bioimaging. Especially, ICG mediated preclinical and clinical *in-vivo* multiphoton imaging can be performed immediately. Another possible direction is the development of the surface-modified polypeptide based nanoparticles for targeted imaging and therapy of the diseased cells/tissue *in-vivo*, which could further improve the contrast and SNR.

Also, this work can be a foundation for various research where newly found optical properties of ICG can be used. Several future studies may be extended to study the optoelectronic applications of ICG. One of the vital applications in optoelectronics is white-light (WL) emission, which has been seen in the case of ICG. As shown in **Figure 6.2,** when ICG is excited using a He-Cd laser wavelength of 325 nm, it shows the WL emission. For this experiment, a photoluminescence (PL) system (Dongwoo Opteron) was used. The ICG electrons, which got excited to S_3 states by absorbing 325 nm laser light, release its energy in the form of emission during S_3 ➔ S_0 state transition. However, they might undergo non-radiative relaxation via internal conversion between S_3 ➔ S_2 and S_2 ➔ S_1 states and further gives emission due to a direct transition from S_2 ➔ S_0 and S_1 ➔ S_0 state. **Figure 6.2(a)** shows the photoluminescence emission spectrum exhibiting two major broad emission bands in visible

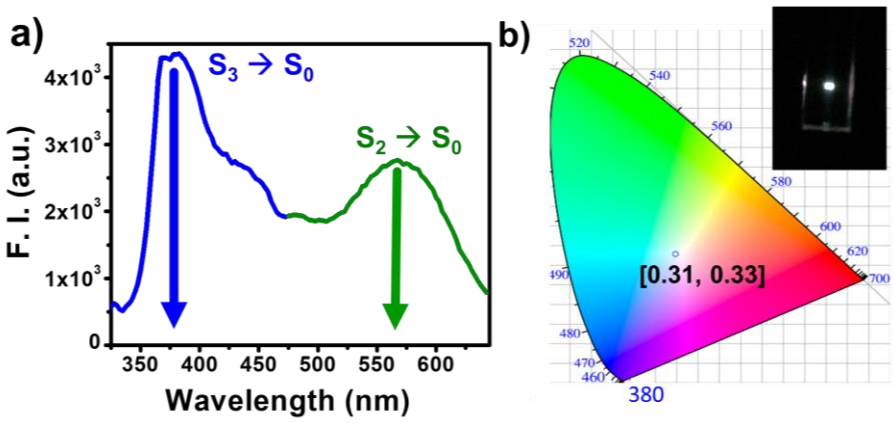

Figure 6.2 WL emission from the aqueous solution of ICG (a) PL spectra collected from 330 nm to 650 nm after excitation by 325 nm with He-Cd laser, the inset shows the mechanism via Jablonski diagram. (b) chromaticity plot coordinates of ICG in aqueous solution (inset: digital image of ICG in cuvette when excited by 325 nm laser).

wavelength range with peaks at ~380 and ~575 nm, respectively, which results in the production of WL. The commission international del' Elcairage (CIE) chromaticity coordinates of ICG were found to be (0.31, 0.33), which are very close to the perfect WL emission coordinates, i.e., (0.33, 0.33) as shown in **Figure 6.2(b)**. The inset of **Figure 6.2(b)** shows the colored digital image of the bright WL emission from the aqueous solution of the ICG upon excitation at 325 nm. This result suggests that the ICG could also be used as a biocompatible WL emitting molecule in the WL emitting devices such as light-emitting electrochemical cells.[1, 2]

6.3 References

1. Jenatsch S, Wang L, Bulloni M, *et al.* (2016) Doping Evolution and Junction Formation in Stacked Cyanine Dye Light-Emitting Electrochemical Cells. ACS Appl Mater Interfaces 8:6554–6562. https://doi.org/10.1021/acsami.5b12055

2. Pertegás A, Tordera D, Serrano-Pérez JJ, *et al.* (2013) Light-emitting electrochemical cells using cyanine dyes as the active components. J Am Chem Soc 135:18008–18011. https://doi.org/10.1021/ja407515w